ACCURATE SIMULATIONS OF CONVECTION IN STELLAR ATMOSPHERES

By

Regner Trampedach

A DISSERTATION

To be submitted to
Michigan State University
in partial fulfillment of the requirements
for the degree of

DOCTOR OF PHILOSOPHY

Department of Physics and Astronomy

2003

ABSTRACT

ACCURATE SIMULATIONS OF
CONVECTION IN STELLAR ATMOSPHERES

By

Regner Trampedach

I present the ingredients for high precision, 3D hydrodynamical simulations of convection in stellar atmospheres, as well as a number of applications. I have developed a new scheme for evaluating radiative transfer, an improved equation of state and I have investigated a number of directions for improving the numerical stability of the convection simulations.

The equation of state (EOS) used for the simulations, is updated by including post-Holtzmark micro-field distributions and relativistic electron-degeneracy as previously published. I have further included quantum effects, higher-order Coulomb interactions and improved treatment of extended particles. These processes (except relativistic degeneracy) have a significant effect in the solar convection zone, and most of them peak at a depth of only 10 Mm. I also include a range of astrophysically significant molecules, besides H_2 and the H_2^+-ion. This EOS will be used directly in the convection simulations, providing the thermodynamic state of the plasma, and as a foundation for a new calculation of opacities for stellar atmospheres and interiors.

A new scheme for evaluating radiative transfer in dynamic and multi-dimensional stellar atmosphere calculations is developed. The idea being, that if carefully chosen, very few wavelengths can reproduce the full radiative transfer solution. This method is based on a calibration against a full solution to a 1D reference atmosphere, and is therefore not useful for 1D stellar atmosphere modeling. The first tests of the method are very promising, and reveals that the new method is an improvement over the former opacity binning technique. The range of convective fluctuations is spanned more accurately and not only the radiative heating, but also the first three angular moments of the specific intensity, can be evaluated reliably. Work on implementing the method in the convection-code, is in progress.

These developments will be employed in the future for a number of detailed simulations of primary targets for the upcoming, space-based, astero-seismology missions, and will include α Cen A and B, η Boo, Procyon and β Hyi. Work on a 10 Mm deep solar simulation was severely hampered by numerical instabilities, but investigating the issue has revealed a number of potential solutions, that will be tested in the near future. The work on individual stars will soon be super-seeded by an effort to compute a grid of convection simulations in $T_{\rm eff}, \log g$ and metallicity, [Fe/H], in the spirit of present-day, grids of conventional atmosphere models.

Regner Trampedach, November 27, 2003.

ACKNOWLEDGMENTS

This dissertation would not have been possible without the help of a great number of great people.

I would in particular like to thank my advisor, Dr. Robert F. Stein, for generous hospitality during my visits to MSU before I started in the graduate program, for inviting me to pursue a Ph.D. with him at MSU, and for a great number of helpful insights during all these years.

I would like to thank Dr. Werner Däppen, at University of Southern California (USC) for generous hospitality during my numerous visits to Los Angeles, and for guiding me through the intricacies of the equation of state, as well as China Town and Old Town, L.A.

I would also like to thank Martin Asplund for hospitality during my visits in Upssala, Sweden, and, lately, Canberra, Australia

Doing research entails a lot of reading-up on what other people have been doing on the subject you are working on; To learn about the subject—learn how to do, and how not to do it, find a new angle to a problem, etc. As you can see from a quick glance at the bibliography, quite a lot of reading has gone in to this research, and if I had, had to visit the library and make a photocopy of each of those papers, I would barely have made it through the second page of references. This dissertation and

the included papers, have benefitted tremendously from NASA's Astrophysics Data System (ADS) and I send the people who power the abstract server, my deep-felt gratitude.

It has been delightful to share office with friend and long-time convection-colleguae Dali Georgobiani—and very convinient, both in terms of coffee-breaks and discussions about work.

I would also like to thank Dr. Horace Smith for initiating the excellent institution of "bad, fifties sci-fi nights", during which I got acquainted with blissfully obscure productions from an emerging danish film industry. The mere mentioning of titles such as, "Reptilicus" and "Journey to the 7^{th} Planet" now evokes a strange mix of patriotism and, well—embarresment.

Last, but by no means least; This dissertation has been powered by oatmeal-raisin cookies, lovingly provided by my wife, Charlotte Mudar. Her patience, support and love has enabled me to keep my sanity through this endeavour.

TABLE OF CONTENTS

LIST OF TABLES

LIST OF FIGURES

Chapter 1

Introduction

Understanding stars is a very multi-faceted endeavor Stars are basically self-gravitating "Great Balls of Fire" (Lewis 1957) with their cores having temperatures and densities high enough for nuclear fusion to take place, and supply the star with energy. The stability of the star is provided by the pressure of the gas counter-acting the inward force of gravity, establishing a hydro-static equilibrium.

This reveals that the equation of state (EOS), supplying the thermodynamical relations between temperature, density and pressure, must be a key ingredient in or model of a star. The energy travels out through the star, in one of three ways; either by conduction, radiation or convection. Simple conduction is only important for very dense objects, where the gas begins to act as a metal. This happens for, *e.g.*, neutron stars and white dwarfs, but also in the centers gaseous planets. Radiative transfer of energy, takes place in all stars and is also a key ingredient for any stellar model. The opaqueness, or opacity, of the gas determines the ease with which light can travel through the star. With a higher opacity, the energy cannot escape as freely and the

interior will heat up, til the energy that escapes matches the energy that is produced inside, setting up a radiative equilibrium. The opacity is composed of a number of processes between light and matter. Cross-sections for the various processes are evaluated from detailed knowledge of the quantum-mechanical wave-functions of all possible states of the implicated particles. Calculation of these cross-sections is a field of research in itself, and the vast calculations involved, have only been possible within the last two decades with the progress of computing-power.

To calculate the opacity, relevant for a stellar model, from the cross-sections of individual processes, we need to multiply by the number-densities of the involved particles, and add-up all the processes. The number-densities of the various particles, and the population of the energy-levels of each kind of particle, is also a result of the equation of state, which therefore has a dual rôle.

The equation of state is likewise a major atomic physics project, as the interactions between the particles constituting the gas, has to be accounted for. Although the gas is electrically neutral on a whole, most of the particles will be charged, being ionized due to the temperatures. The particles therefore feel each others presence by their charges, especially at higher densities where close encounters will be more frequent. In really close encounters quantum effects will have an effect; The particles will no longer be point-like, but "smeared out" according to the Heisenberg uncertainty principle, and encounters between identical particles will be governed by Pauli's exclusion principle. All of these effect (and many more) has an effect both on the thermodynamics of the gas, as well as on the ionization-balances and the population of energy-levels, important for opacity calculations.

The last mode of energy-transport is convection, which consists of macroscopic bubbles or flows of warmer than average gas, moving out towards lower temperatures, shedding its excess heat and sink down to higher temperatures and be recycled. If the opacity is very high and the energy has a hard time escaping via radiation, the gas will become instable towards convection and this will take over the transport of energy.

Convection is inherently a dynamic process, involving a lot of non-linear phenomena. As such, it is not amenable to simplified theories, and a good and relatively simple description of convection suitable for stellar modeling has eluded us. The so-called mixing-length-formulation of convection is simple and very suitable for use in stellar structure codes. It is, however, fraught by it's assumptions breaking down where a theory of convection is most needed, and by free parameters that have to be calibrated from outside the theory.

For envelope convection, *i.e.*, where the convection zone reaches all the way out the the surface, but not necessarily all the way in to the center, further complications arise at the surface. Here radiative transport begins to become important again, as the distance to the surface (where light can escape) becomes comparable with the mean-free-path of photons. This region is called the stellar atmosphere, the modeling of which, forms its own field of research. As the gas becomes optically thin, and photons can begin to escape freely, evaluation of radiative transfer becomes much more complicated. The radiative transport of energy can no longer be described by a single opacity, but have to be evaluated at upwards of 10^4 wavelengths. Combine this transition between optically thick and optically thin, with the transition between

convective and radiative transport of energy, and you have a very intractable problem.

The best way of studying this region, is through three-dimensional (3d) hydrodynamical simulations, for which a very small number of approximations has to be introduced. They are based on the same equation of state and opacities also used in conventional (*e.g.*, 1D) stellar models, but the hydrodynamics of the problem is solved explicitly, based on the fundamental laws of conservation of mass, momentum and energy.

Such simulations can be used for the same purposes as conventional stellar atmosphere model, *e.g.*, interpretation of observations including abundance analysis, and as upper boundary conditions for stellar structure and evolution models.

The above sketch of stellar structure, hopefully gives an impression of the interrelatedness of all the phenomena participating in making a star, a star, and serves as the motivation behind the present dissertation.

In chapter 2 the hydrodynamical convection simulations are introduced, and a stability problem is discussed. In chapter 3 I discuss the atomic physics entering both the convection simulations and the stellar structure models, presenting the current state of astrophysical equations of state in Sect. 3.1.1 and 3.1.1, and proposing some improvements to one particular EOS-project, in Sect. 3.2.5. In Sect. ?? I give a short overview of recent developments in opacity calculations, and expectations for the near future.

Chapter 4 deals with the evaluation of radiative transfer in the convection simulations, and how to bring the problem down to tractable dimensions, and yet only loose a little in accuracy compared to solutions including $\gtrsim 10^5$ wavelenght-points.

Chapter 5 presents a few applications of convection simulations in conjunction with stellar structure calculations. In Sect. 5 the convection simulations are used as boundary conditions for stellar structure models, which is used in Sect. 5.1.10 for a calibration of the main parameter, α, of the mixing-length formulation.

A summary and an outlook on the future, is offered in chapter 6, which ends this dissertation.

Chapter 2

Hydrodynamics

The code for the convection simulations used in this work, was written by Nordlund & Stein (1990) and is further described in (Nordlund 1982; Stein 1989).

The simulations are of compressible convection, subjected to realistic radiative transfer including the effect of line-blanketing. The boundaries are transmitting, with the entropy of the in-flow being adjusted (a constant in time), so as to result in the desired flux for the given simulation.

A state of the art equation of state, presented in Sect. 3.1.1, is used, together with equally high quality opacities.

The properties and morphology of the convection in the simulations, is described by, *e.g.*, (Nordlund & Stein 1991) and Stein & Nordlund (1989).

2.1 The Navier-Stokes Equations

The *conservative* or *divergence* form of the Navier-Stokes equations is

$$\frac{\partial \varrho}{\partial t} + \nabla \cdot (\varrho \boldsymbol{u}) = 0 \tag{1}$$

$$\frac{\partial \varrho \boldsymbol{u}}{\partial t} + \nabla \cdot (\varrho \boldsymbol{u}\boldsymbol{u} - \boldsymbol{\sigma}) = \boldsymbol{f}_{\mathrm{e}} \tag{2}$$

$$\frac{\partial \varrho \varepsilon_{\mathrm{tot}}}{\partial t} + \nabla \cdot (\varrho \varepsilon_{\mathrm{tot}} \boldsymbol{u} - \boldsymbol{\sigma}\boldsymbol{u} + \boldsymbol{q}) = \boldsymbol{f}_{\mathrm{e}} \cdot \boldsymbol{u} \ , \tag{3}$$

where ϱ is the density, $\varepsilon_{\mathrm{tot}} = \varepsilon + \frac{1}{2}\boldsymbol{u}^2$ is the total specific internal energy, $\boldsymbol{u}$ is the velocity field, $\boldsymbol{q}$ is the heat-flux vector and $\boldsymbol{f}_{\mathrm{e}}$ is the external force per unit volume.

The stress-tensor, $\boldsymbol{\sigma}$, can be written

$$\boldsymbol{\sigma} = -P_{\mathrm{g}}\boldsymbol{I} + \boldsymbol{T} , \tag{4}$$

where P_{g} is the gas pressure, $\boldsymbol{I}$ is the unity tensor with components $I_{ij} = \delta_{ij}$ and $\boldsymbol{T}$ is the viscous stress tensor with components T_{ij}.

Expanding Eqs. (1)–(3), eliminating occurrences of Eq. (1) and substituting Eq. (4), we arrive at the following three equations: the equation of mass conservation, often referred to as the continuity equation,

$$\frac{\partial \varrho}{\partial t} = -\boldsymbol{u} \cdot \nabla \varrho - \varrho \nabla \cdot \boldsymbol{u}, \tag{5}$$

the equation of momentum conservation, also called the equation of motion,

$$\varrho\frac{\partial \boldsymbol{u}}{\partial t} = -\varrho\boldsymbol{u}\cdot\nabla\boldsymbol{u} + \boldsymbol{f}_{\rm e} - \nabla P_{\rm g} + \nabla\boldsymbol{T}\,, \tag{6}$$

and the equation of energy conservation (with $E = \varrho\varepsilon$),

$$\frac{\partial E}{\partial t} = -\nabla\cdot(\boldsymbol{u}E) + (\boldsymbol{T} - P)\nabla\cdot\boldsymbol{u} + \nabla\cdot\boldsymbol{q}\,. \tag{7}$$

Because the densities and pressures change by 4-5 orders of magnitude from the top to the bottom of the simulations, it is advantageous to precondition the equations for use in the highly stratified case of stellar atmospheres. This is done by rewriting (5) - (7) in terms of logarithmic density, $\ln\varrho$, velocity, $\boldsymbol{u}$, and internal energy per unit mass, ε:

$$\frac{\partial \ln\varrho}{\partial t} = -\boldsymbol{u}\cdot\nabla\ln\varrho - \nabla\cdot\boldsymbol{u}, \tag{8}$$

$$\frac{\partial \boldsymbol{u}}{\partial t} = -\boldsymbol{u}\cdot\nabla\boldsymbol{u} + \boldsymbol{g} - \frac{P_{\rm g}}{\varrho}\nabla\ln P + \frac{1}{\varrho}\nabla\boldsymbol{T} \tag{9}$$

and

$$\frac{\partial \varepsilon}{\partial t} = -\boldsymbol{u}\cdot\nabla\varepsilon + \frac{\boldsymbol{T} - P}{\varrho}\nabla\cdot\boldsymbol{u} + \frac{1}{\varrho}\nabla\cdot\boldsymbol{q}\,, \tag{10}$$

where, for the external force, we use $\boldsymbol{f}_{\rm e}/\varrho = \boldsymbol{g}$, the gravitational acceleration, which is assumed to be constant with depth. These equations are much more well behaved than Eqs. (5) - (7) and the various derivatives are also smoother.

As the gradient of a flux is the time-derivative of the quantity transported by the flux, we define $Q_{\rm rad} \equiv \varrho^{-1}\nabla\cdot\boldsymbol{q}$, where $Q_{\rm rad}$ is the specific (radiative) heating.

2.2 Diffusion

In the energy equation the term in the viscous stress-tensor, $\boldsymbol{T}$, is the dissipation term, which we will re-write in a manner similar to $Q_{\rm rad}$: $Q_{\rm visc} \equiv \varrho^{-1}\boldsymbol{T}\nabla\cdot\boldsymbol{u}$.

The $\boldsymbol{T}$-term in the momentum equation, is the (velocity-) diffusion. We will re-write this in component form, to

$$\left(\frac{\partial u_i}{\partial t}\right)_{\rm diff} = \frac{1}{\varrho}\sum_j \frac{\partial}{\partial x_j}\left[\nu_j \varrho \frac{\partial u_i}{\partial x_j}\right] = \frac{1}{\varrho}\sum_j \frac{\partial T_{ij}}{\partial x_j} \quad \Leftrightarrow \tag{11}$$

$$T_{ij} = \nu_j \varrho \frac{\partial u_i}{\partial x_j} \,. \tag{12}$$

Comparing Eq. (9) and (12) we see that the diffusion coefficients, ν_j, have dimensions [L^2/T].

With the dissipation tensor, $\boldsymbol{T}$, so defined, the dissipation is

$$Q_{\rm visc} = \frac{\boldsymbol{T}}{\varrho}\nabla\cdot\boldsymbol{u} = \frac{1}{\varrho}\sum_{i,j} T_{ij}\frac{\partial u_i}{\partial x_j} = \sum_{i,j}\nu_j \frac{\partial u_i}{\partial x_j}\frac{\partial u_i}{\partial x_j} = \sum_{i,j}\nu_j\left(\frac{\partial u_i}{\partial x_j}\right)^2 \,. \tag{13}$$

2.2.1 Second Order Diffusion

Similar to Eq. 11, the second-order diffusion for a per-unit-mass quantity f, adds a contribution of the form

$$\frac{\partial f}{\partial t} = \cdots + \frac{1}{\varrho}\sum_j \frac{\partial}{\partial x_j}\left[\nu_{2j}\varrho\frac{\partial f}{\partial x_j}\right]. \tag{14}$$

The summation is over directions, $j = x$, y and z.

If the order of the numerical differencing is higher than 1, the derivatives will be oblivious to a two-zone oscillations, as depicted in Fig. 1. It can easily be shown that the derivative of a smooth interpolating function will be zero at the peaks of a two-zone oscillation.

For higher than first-order differencing schemes, it is therefore necessary to expand Eq. (14) into

$$\frac{\partial f}{\partial t} = \cdots + \sum_j \left[\nu_{2j} \frac{\partial^2 f}{\partial x_j^2} + \left(\frac{\partial \nu_{2j}}{\partial x_j} + \nu_{2j} \frac{\partial \ln \varrho}{\partial x_j} \right) \frac{\partial f}{\partial x_j} \right] . \tag{15}$$

We are using a first-order differencing scheme, but the expansion will nonetheless prove useful in the subsequent discussion.

The linear finite difference version of the second derivative is

$$(\Delta x_j)^2 \left[\frac{\Delta^2 f}{\Delta x^2} \right] (i) = \Delta^2 f_i = \Delta f(i+\tfrac{1}{2}) - \Delta f(1-\tfrac{1}{2}) = f(i-1) - 2f(i) + f(i+1) \; . \tag{16}$$

If the quantity is a pure oscillatory signal with amplitude, δ, and a wavelength of two grid-points (a so-called *two-zone oscillation*), as shown in Fig. 1, then we have $f_{i-1} = f_{i+1} = -f_i = \pm\delta$ and consequently

$$\frac{\Delta^2 f_i}{\Delta x_j} = -\frac{4 f_i}{\Delta x_j} \; , \tag{17}$$

for a uniform grid. Adding to f, a term proportional to $\Delta^2 f_i / \Delta x_j$, will therefore dampen a two-zone oscillation.

In the horizontal directions (x and y) the grid is uniform and therefore the

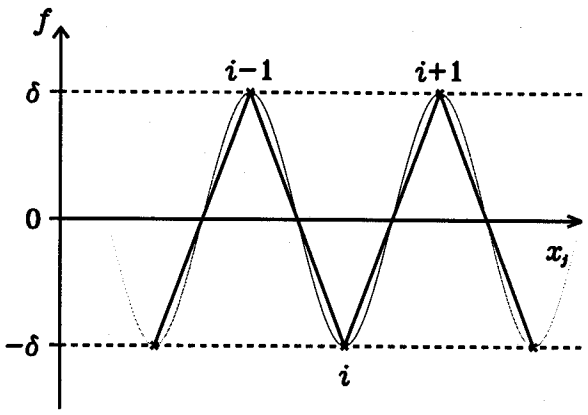

Fig. 1. Schematic of a pure two-zone oscillation. The thin curve is an example of a smooth interpolating function, illustrating the zero derivatives.

first term in the parenthesis multiplying the first derivative in Eq. (15) is zero. The horizontal density derivatives are also rather small, leaving the second derivative term the dominant one.

Similar to the derivation of Eq. (17), we find that the first-order first-derivative is twice the function, phase-shifted by half a grid-point. The first-derivative contribution to the second-order diffusion is therefore assured to be smaller than the second-derivative contribution by at least a factor of two.

2.2.2 Fourth Order Diffusion

In order to minimize unduly damping of physical features, we can go to higher order schemes, which will have a higher ratio of two-zone-oscillations to smoother features.

Fourth-order diffusion adds a contribution of the form

$$\frac{\partial f}{\partial t} = \cdots - \frac{1}{\varrho} \sum_j \frac{\partial^2}{\partial x_j^2} \left[\nu_{4j} \varrho \frac{\partial^2 f}{\partial x_j^2} \right] , \tag{18}$$

the sign of which will be justified below.

The corresponding dissipation is

$$Q_{\mathrm{visc},4} = \sum_{i,j} \nu_{4j} \left(\frac{\partial^2 u_i}{\partial x_j^2} \right)^2 . \tag{19}$$

The linear, finite differences version of the third- and fourth-derivatives on a uniform grid, are

$$(\Delta x)^3 \left[\frac{\Delta^3 f}{\Delta x^3} \right] (i - \tfrac{1}{2}) = \Delta^3 f(i - \tfrac{1}{2}) = \Delta^2 f(i) - \Delta^2 f(i-1) \tag{20}$$

$$= -f(i-2) + 3f(i-1) - 3f(i) + f(i+1) \tag{21}$$

and

$$(\Delta x)^4 \left[\frac{\Delta^4 f}{\Delta x^4} \right] (i) = \Delta^4 f(i) = \Delta^3 f(i + \tfrac{1}{2}) - \Delta^3 f(i - \tfrac{1}{2}) \tag{22}$$

$$= f(i-2) - 4f(i-1) + 6f(i) - 4f(i+1) + f(i+2) . \tag{23}$$

In the case of a pure two-zone oscillation, we therefore have that $\Delta^3 f_i = 8 f_i$ and $\Delta^4 f_i = 16 f_i$, or in general $\Delta^N f_i = 2^N f_i$. This is true for the linear difference scheme, and for third-order differences, it can be shown that the constant is $12^{N/2}$.

To destroy a two-zone oscillation with the pure fourth-order term, we therefore need to subtract a term proportional to $\Delta^4 f_i$. Using a linear difference scheme, two-zone oscillation will therefore be four times more prominent in forth-order derivatives than in second order derivatives. But what about physical features like sharp gradients?

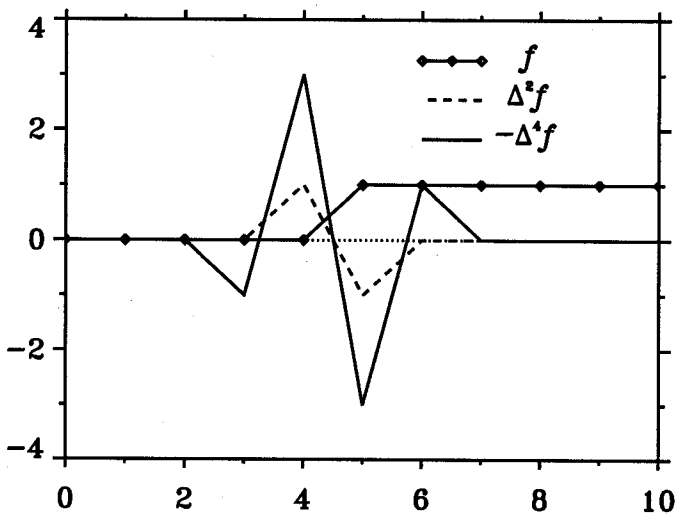

Fig. 2. Schematic of the response to a step function (solid line with diamonds). The dashed lined shows the corresponding linear second order difference, and the solid line is the linear fourth order difference.

Fig. 2 shows the response of second- and fourth-order derivatives to a step function — the ultimate in large gradients. From the figure, we see how second-order diffusion simply smooth out the large gradient, spreading it over more zones. Fourth-order diffusion does the same, and more efficiently, but it also introduces some extra peaks on either side of the gradient. These extra peaks, coupled with the (global) cubic-spline interpolations and differentiations used elsewhere in the simulations, quickly and efficiently excite two-zone oscillations. This phenomenon is called ringing, and it is excited by sharp edges, as well as localized peaks.

We want to keep the gradients as large as possible, and capture as much detail as possible, with a finite resolution of the simulations. We therefore want a large two-zone-oscillation to step-function response ratio. For linear second-order derivatives, this ratio is 4/1, and for fourth-order derivatives it is $16/3=5.\bar{3}$. So we do gain a little going from second- to fourth-order, but at the expense of extra excitation of two-zone oscillations.

2.2.3 Quenched Diffusion

One way around this problem is the so-called quenched diffusion, introduced by Robert F. Stein and Åke Nordlund in the early '90s (private communications). The quenching consists of using an expression for ν_{4j} that involves a (signed) first-order difference, scaled with the ratio of (unsigned) third-order differences to (unsigned) first-order differences,

$$\frac{\Delta_3 f}{\Delta x_j} = \frac{\Delta f}{\Delta x_j} \frac{\max_3 |\Delta^3 f|}{\max_3 |\Delta f|}, \tag{24}$$

centered on $i - \frac{1}{2}$. The $\max_3$-operator takes the maximum value in a three-point neighborhood of i, *i.e.* $i-1, i, i+1$. The third-order difference is defined by Eq. (20). By scaling the first-order difference in this way one obtains a diffusive flux that has the sign of the first-order difference, but the order of magnitude of the third-order difference. In smooth parts of the solution the diffusive flux will thus be quenched (hence the denomination), and the effect of the diffusion operator will be of similar magnitude as that of a fourth-order diffusion operator. In steep parts of the solution, on the other hand, the ratio of the third- to first-order difference will be of the order unity or larger, and the diffusion will be similar to normal second-order diffusion.

The diffusion contributions are combined into

$$\frac{\partial f}{\partial t} = \cdots + \frac{1}{\varrho} \sum_j \frac{\partial}{\partial x_j} \left[\varrho \left(\nu_{2j} \frac{\partial f}{\partial x_j} + \nu_{4j} \frac{\Delta_3 f}{\Delta x_j} \right) \right], \tag{25}$$

where the first part is a second-order diffusion that is active mainly in shocks. The second part is qualitatively similar to a fourth-order diffusion, but has the advantage

that sharp edges and localized peaks do not give rise to the ringing that tends to develop with a normal fourth-order operator. In the combined second- and fourth-order diffusion, enough second-order diffusion must be present to counteract the tendency for ringing from the fourth-order operator. Since this tendency is not present when (25) is used, one can remove the second-order diffusion altogether, except in shocks, where significant local diffusion is always needed.

With the quenched diffusion, only the shock capturing a_2 term is kept in the pure second-order part of the diffusion, and all three terms: advection-, shock- and sound-wave-terms, are included in the quenched part (See Sect. 2.2.4).

The dissipation that corresponds to (25) is

$$Q_{\text{visc}} = \sum_{i,j} \left[\frac{\partial u_i}{\partial x_j} \left(\nu_{2j} \frac{\partial u_i}{\partial x_j} + \nu_{4j} \Delta_3 u_i \right) \right]. \tag{26}$$

The diffusion at the top and the bottom are set to zero in both diffusion schemes to avoid boundary effects. All of the non-local operators take advantage of the periodic properties in the horizontal directions and are skewed at the top and bottom boundary.

The quenched diffusion works very well, as long as the two-zone oscillations in the first derivative is larger than the broader features in the first derivative — that is, when the two-zone oscillations are centered around zero. Otherwise it fails to pick-up the two-zone oscillations. The latter is often the case deeper in the simulations, and was of less concern for the shallow simulations pursued so far. During work on a 10 Mm deep solar simulation, this proved detrimental. The symptoms had also been

noticed higher in the atmosphere of a number of different simulations, introducing noise in the radiative transfer calculations and two-zone oscillations in temperature.

2.2.4 A Gallery of Diffusion Coefficients

The various forms of the diffusion coefficients all contain combinations of three terms with the following motivation: The

a_1 -term is proportional to the fluid velocity to prevent ringing at sharp changes in advected quantities.

a_2 -term is is proportional to a finite difference velocity convergence (when positive), and is necessary to prevent excessive steepening of shocks.

a_3 -term is proportional to the sound speed, and is necessary to stabilize sound waves and weak shocks. Also needed to stabilize 2-zone oscillations.

The Original Mixed 2+4-Order Version

$$\nu_{2j} = (a_1|u_j| + a_2\Delta_4^+ u_j)\frac{\Delta x_j}{12} \ , \tag{27}$$

where the velocity convergence is defined as

$$\Delta_k^+(u_j) = \sum_{i=1-k/2}^{k/2} [u_{j,i-1} - u_{j,i}] > 0 \ . \tag{28}$$

If the fluid in two adjacent volume-elements are approaching, $\Delta_k^+(u_j)$ is equal to their relative velocity, in k volume-elements around the two.

The fourth-order diffusion coefficient is

$$\nu_{4j} = (4a_1|u_j| + a_3 c_s)\frac{\Delta x_j}{12^2} , \tag{29}$$

where c_s is the adiabatic sound-speed.

The Original Form used with Quenched Diffusion

We use a diffusion suppression factor

$$f_\varrho = [1 + (\varrho/\varrho_0)]^{-1} . \tag{30}$$

The second-order diffusion coefficient is

$$\nu_{2j} = \frac{\Delta x_j}{12} a_2 f_\varrho \, \Delta_4^+(u_j) , \tag{31}$$

and the fourth-order diffusion coefficient is

$$\nu_{4j} = \frac{\Delta x_j}{12} \left[a_1|u_j| + a_2 f_\varrho \, \Delta_4^+(u_j) + a_3 c_s\right] . \tag{32}$$

2.3 Alternative solutions

Neither of the two diffusion-schemes outlined above, the second plus fourth order diffusion, or the quenched diffusion, are optimal for the convection simulations. Two-zone oscillations are excited by the cubic-spline interpolation employed, and these two

diffusion schemes do not dampen them efficiently without also smoothing physical features. We need another scheme for either dampening or avoiding these two-zone oscillations all together.

2.3.1 Subtracting a Smooth Average

One straight forward solution to the problem, is simply to subtract out the physical variation, to leave the undesired two-zone oscillations exposed:

$$f_i' = f_i - \sum_{j=i-N}^{i+N} w_j f_j \ , \tag{33}$$

where the weights w_j define the functional form of the averaging procedure and $2N+1$ is the number of points involved in the averaging. We have chosen a Gaussian averaging kernel

$$w_j = \frac{\exp(-(j/\sigma)^2)}{\sum_{j=i-N}^{i+N} \exp(-(j/\sigma)^2)} \ , \tag{34}$$

where σ is the width of the Gaussian and the denominator takes care of the normalization. Using a full-width-half-maximum of $W = 3\sigma\sqrt{\ln 2}$ of three points, has proven optimal for getting a large signal from the two-zone oscillations. The factor of three in the expression for W stems from the counting of grid points. Normally there would be factor of two to result in the width and not just the position, $\pm x$, of half-maximum. In the discrete case, however, we also have to count the point in the middle.

In choosing N there is obviously a trade-off between the computational expense

and the "smoothness" of the average. Rather surprisingly a three point average is very close to a five point average, and a seven point average is indistinguishable from the five point average. These are the results for real case scenarios, simply going through a snapshot of a simulation in both horizontal and vertical directions, and compare f' for $2N+1$ =3, 5 and 7.

Using $W = 3$ and $N = 1$ therefore results in the weights $w = [\frac{1}{4}, \frac{1}{2}, \frac{1}{4}]$, and

$$f_i = -\tfrac{1}{4} f_{i-1} + \tfrac{1}{2} f_i - \tfrac{1}{4} f_{i+1} \ , \tag{35}$$

which has first order differences

$$\begin{aligned} \Delta f'(i-\tfrac{1}{2}) &= f'(i) - f'(i-1) \\ &= \tfrac{1}{4} f(i-2) - \tfrac{3}{4} f(i-1) + \tfrac{3}{4} f(i) - \tfrac{1}{4} f(i+1) \ . \end{aligned} \tag{36}$$

From Eq. 20, we recognize this as the third order difference of f. The procedure is commutative, so whether subtracting the Gaussian average before or after the differencing, gives the same result. By subtracting out a Gaussian average, we merely change the first order differences into third order differences, immediately bringing us back to the problems of Sect. 18. The extra peaks introduced around steep gradients (See Fig. 2), do not depend on the choice of N. This idea has therefore been abandoned.

2.3.2 Monotonic interpolation schemes

In Fig. 3 we show how a cubic-spline interpolation across a step-function, generates oscillations in the derivatives on either sides of the step. A cubic spline, is a series of piece-wise cubic polynomia, connected by the requirement that the second derivatives be continous (de Boor 1978). We see from Fig. 3 that the interpolating function is not monotonic between grid-points, and that this is the reason for the excitation of two-zone oscillations around sharp edges.

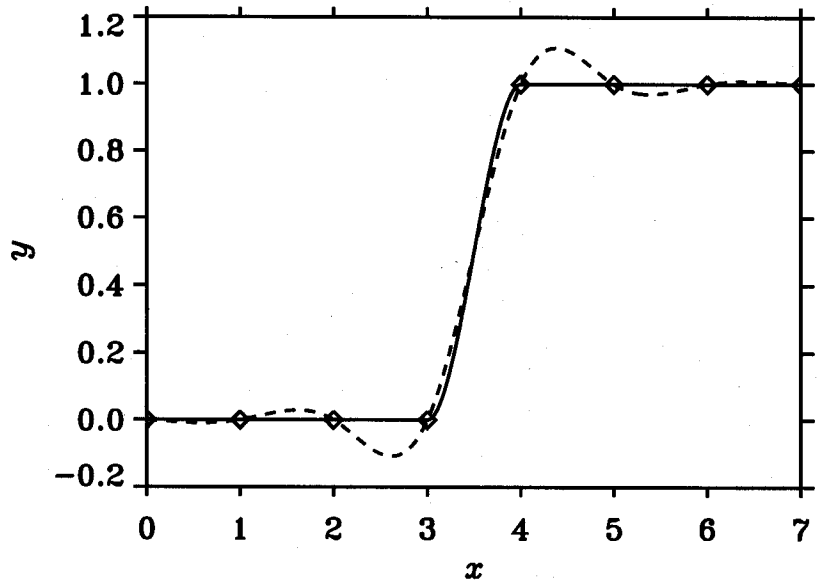

Fig. 3. Cubic-spline interpolation (dashed line) across a step-function (diamonds). The solid line shows a cubic interpolation where the derivatives have been forced to be zero (not a spline).

There a number of schemes for calculating monotonic interpolating functions, of which some are local and compact and others are global in nature. The principle of the requirement of monotonicity, is illustrated by the solid curve in Fig. 3. This is a piece-wise cubic interpolation where the derivatives on either side of the step,

has been set to zero. This results in a visually much more pleasing behaviour. This is admittedly a rather subjective criterium for the quality of an interpolant, but a valuable first test. The deciding test is how the scheme fares when applied to advection-, shock-tube- and wave-tests with analytical solutions.

There are a great number of monotonic scheme interpolation schemes on the market (*e.g.*, Fritsch & Butland 1984, and references therein). All of these schemes would qualitatively result in the same interpolating function in the case shown in Fig. 3, but behave differently when presented with, *e.g.*, triangular functions, Gaussians, parabolas, multiple step functions and similarely challenging tests.

One monotonic scheme, which is rather pleasing for its simplicity, uses piece-wise cubic-splines, disconnecting two parts of the spline where the solution is not monotonic between grid-points. This obviously raises the question about the boundary conditions on the two parts of the spline. The solid curve in Fig. 3 is an example of this scheme.

The total variation diminishing (TVD) schemes, as introduced by Harten (1983), use a measure of the overall amount of oscillation of a quantity u

$$TV[u(t)] = \sum_{i=1}^{N} |u_{i+1}(t) - u_i(t)| \ , \tag{37}$$

and require this quantity not to increase with time, t. A good presentation of TVD was recently written by Trac & Pen (2003).

In general, the order of the interpolation goes down across a discontinuity, but this is a small price to pay for increased stability and a more physical solution in the

smoother parts of the simulation.

There are several promising ways of solving the problems of instabilities in the convection simulations, and future investigations of these will reveal which is the best solution to the problem at hand.

In parallel with this work, a new version of the code, specifically optimized for massive parallelization, is being written by Nordlund, Stein, Carlsson & Hansted (private communications). This new version employs a staggered grid, with energy and density defined at cell-centers and velocities on cell-boundaries, which will most likely be stable against two-zone oscillations. Other problems are introduced with this formulation, though, in particular regarding the stabillity of the upper and lower boundaries of the simulation domain.

Chapter 3

Input Physics

The atomic physics underlying a model of an astrophysical phenomena is decisive for the quality of that model.

In Sect. 3.1.1 I present an analysis and comparison between two of the leading equation of state projects; the so-called Mihalas-Hummer-Däppen (MHD) equation of state (Hummer & Mihalas 1988; Mihalas et al. 1988; Däppen et al. 1988) and the OPAL equation of state pursued at Lawrence Livermore National Laboratory (Rogers 1986; Iglesias & Rogers 1995; Rogers et al. 1996, and references therein).

An artificial term, Ψ, in the MHD EOS that ensures pressure ionization in cold and dense plasmas, has been suspected of contaminating this EOS under solar conditions, and maybe even be needed for pressure ionization in the Sun. In Sect. 3.1.1 this term is examined an found "not guilty" of the above charges. It is, however, still suspicious and indicates a more fundamental flaw in the employed picture of interactions between neutral particles.

The close scrutiny of the MHD EOS in Sects. 3.1.1 and 3.1.1 has paved the

way for the improvements presented in Sect. 3.2.5 aimed at broadening the range of applicability and increasing the accuracy of the MHD EOS. This work is equally aimed at the convection simulations and the general stellar structure and evolution problem. All of the improvements are important for the latter, but for the convection simulations the addition of many more molecules will have the largest effect.

The improved MHD EOS, presented in Sect. 3.2.5 will be used as basis for a new opacity calculation, and in Sect. 3.4 I give a short review of recent progress in the calculation of absorption coefficients.

3.1 Equation of State

The equation of state is essential in most astrophysical context, both for the thermodynamic relations provided by it, and as the foundation for opacity calculations.

Exploring the differences the main EOS projects, I found that the most contested part of the solar EOS, the most uncertain and the most extreme plasma conditions, occur very close to the surface—less than 10 Mm below the photosphere. The deep 10 Mm solar convection simulation will get the whole impact of the improvements presented in this chapter, but even the shallow, 3 Mm simulations will be affected to an extend that can be measured by helioseismology (Christensen-Dalsgaard et al. 1988; Basu & Christensen-Dalsgaard 1997; Di Mauro et al. 2002).

3.1.1 "A Synoptic Comparison of the MHD and the OPAL Equations of State"

by

Trampedach, R., Däppen, W. & Baturin, V. A., 2003, ApJ, (submitted)

The two favorite equations of state of the astrophysical community, are the OPAL equation of state, pursued at Lawrence Livermore National Laboratory (Rogers 1986; Rogers et al. 1996), and the MHD equation of state (Hummer & Mihalas 1988; Mihalas et al. 1988; Däppen et al. 1988), which is part of the international Opacity Project (OP), described in the two volumes (Seaton 1995) and (Berrington 1997).

The present paper, (Trampedach et al. 2004c), compares these two equations of state to set the stage for further developing the MHD EOS in Sect. 3.2.5 (Trampedach & Däppen 2004a).

A synoptic comparison of the MHD and the OPAL equations of state

R. Trampedach[1]
Department of Physics and Astronomy. Michigan State University, East Lansing, MI 48824, USA
trampedach@pa.msu.edu

W. Däppen[1]
Department of Physics and Astronomy, USC, Los Angeles, CA 90089-1342, USA
dappen@usc.edu
and

V. A. Baturin
Sternberg Astronomical Institute, Universitetsky Prospect 13, Moscow 119899, Russia
vab@sai.msu.su

ABSTRACT

A detailed comparison is carried out between two popular equations of state (EOS), the Mihalas-Hummer-Däppen (MHD) and the OPAL equations of state, which have found widespread use in solar and stellar modeling during the past two decades. They are parts of two independent efforts to recalculate stellar opacities; the international Opacity Project (OP) and the Livermore-basd OPAL project. We examine the difference between the two equations of state in a broad sense, over the whole applicable $\varrho - T$ range, and for three different chemical mixtures. Such a global comparison highlights both their differences and their similarities.

We find that omitting a questionable hard-sphere correction, τ, to the Coulomb interaction, greatly improves the agreement between the MHD and OPAL EOS. We also find signs of differences that could stem from quantum effects not yet included in the MHD EOS, and differences in the ionization zones that are probably caused by differences in the micro-field distributions employed. Our analysis do not only give a clearer perception of the limitations of each equation of state for astrophysical applications, but also serve as guidance for future work on the physical issues behind the differences. The outcome should be an improvement of both equations of state.

Subject headings: Atomic processes—Equation of state—Plasmas—Sun: interior

1. Introduction

Stellar modeling, and in particular helio- and asteroseismology, require an equation of state and corresponding thermodynamic quantities that are smooth, consistent, valid over a large range of temperatures and densities, and that incorporate the most important chemical elements of astrophysical relevance Christensen-Dalsgaard & Däppen (for a review see 1992).

In astrophysics, the equation of state plays two basic roles. On the one hand, it supplies the thermodynamics neccessary for describing gaseous objects such as stars and gas-planets. On the other hand it also provides the foundation for opac-

[1]Teoretisk Astrofysik Center, Danmarks Grundforskningsfond, Institut for Fysik og Astronomi, Aarhus Universitet, DK-8000 Aarhus C, Denmark

ity calculations, in the form of ionization equilibria and level populations. Thanks to helioseismology, the Sun has broadened this perspective. The remarkable precision by which we have now peered into the Sun, puts strong demands on any physics going into a solar model. This, to such a degree, that we can turn around the argument and use the Sun as an astrophysical laboratory to study Coulomb systems under conditions not yet achieved on Earth.

Although the solar plasma is only slightly non-ideal, the tight observational constraints prompts the use of methods normally reserved for studies of more strongly-coupled plasmas. In this way the solar experiment addresses a much broader range of plasmas, *e.g.*, Jovian planets, brown dwarfs and low-mass stars, as well as white dwarfs (Cauble et al. 1998).

The two equation-of-state efforts we compare in this paper are associated with the two leading opacity calculations of the eighties and nineties. The MHD EOS (Hummer & Mihalas 1988; Mihalas et al. 1988; Däppen et al. 1988) was developed for the international *Opacity Project* (OP) described and summarized in the two volumes by Seaton (1995) and Berrington (1997), and the OPAL EOS is the equation of state underlying the OPAL opacity project at Livermore (Rogers 1986; Rogers et al. 1996, and references therein).

Another highly successful EOS address the extreme conditions in low-mass stars and giant planets and include the transition to the fluid phase (Saumon & Chabrier 1989; Saumon et al. 1995). In a trade-off between accuracy and range of validity, this EOS has so far only been computed for H/He-mixtures, rendering it less suitable for helioseismic investigations. Comparisons with this EOS should, however, be an essential part of efforts to further develop precise stellar EOS.

The OP and OPAL projects are based on two rather different philosophies; the *chemical picture* and the *physical picture*, respectively, as detailed in Sect. 2.1.1 and 2.1.2. The effect of Coulomb interactions is reviewed in Sect. 2.2, and a correction, τ, to these, that seems to account for a substantial part of the differences between the two formalisms, is explored in Sect. 2.2.2.

Detailed comparisons between the MHD and OPAL EOS have proved very useful for discovering the importance and consequences of several physical effects (Däppen et al. 1990; Däppen 1992, 1996). In Sect. 3, we extend these comparisons to a systematic search in the entire T–ρ plane, and in Sect. 4 we take a closer look at the EOS under solar circumstances.

The consensus of the last few years has been that in helioseismic comparisons the OPAL EOS is closer to the Sun than the MHD EOS (Christensen-Dalsgaard et al. 1996) although both are remarkably better than earlier theories. However, recent helioseismic inversions for the adiabatic exponent $\gamma_1 = (\partial \ln p/\partial \ln \varrho)_{ad}$ (Basu et al. 1999; Di Mauro et al. 2002) shows that the MHD EOS fares better than OPAL in the upper 7% of the sun including the ionization zones of hydrogen and helium. These new developments again highlights the importance of competing equation-of-state efforts and systematic comparisons such as the present.

2. Beyond Ideal Plasmas

The simplest model of a plasma is a non-ionizing mixture of nuclei and electrons, obeying the classical *perfect gas* law. However, an *ideal gas* can be more general than a perfect gas. Ideal only refers to the interactions between particles in the gas. The interactions in any gas redistribute energy and momentum between the particles, giving rise to statistical equilibrium. In an ideal gas these interactions do not contribute to the energy of the gas, implying that they are point interactions. Since the Coulomb potential is not a δ-function, real plasmas cannot be ideal.

Deviations from the perfect gas law, such as ionization, internal degrees of freedom (excited states, spin), radiation and Fermi-Dirac statistics of electrons are all in the ideal regime. And the particles forming the gas can be classical or quantum, material or photonic; as long as their interactions have no range, the gas is still ideal. All such ideal effects can be calculated as exactly as desired.

The ideal picture, is however, not adequate even for the solar case. At the solar center, an ideal-gas calculation leaves about 20% of the gas unionized. On the other hand, the mere size of the neutral (unperturbed) atoms, do not permit more than 7% of the hydrogen to be unionized at these densities, provided the atoms stay in the ground state and are closely packed. At the temperature

at the center of the Sun neither of these assumptions can possibly hold and the mere introduction of *size* and *packed* immediately imply interactions between the constituents of the plasma and it is therefore no longer ideal.

In a plasma of charges, Z, with average interparticle distance $\langle r \rangle$, we define the coupling parameter, Γ, as the ratio of average potential binding energy over mean kinetic energy $k_{\rm B}T$

$$\Gamma = \frac{Z^2 e^2}{k_{\rm B} T \langle r \rangle} \ . \qquad (1)$$

Plasmas with $\Gamma \gg 1$ are *strongly* coupled, *e.g.* the interior of white dwarfs, where coupling can become so strong as to force crystallization. Those with $\Gamma \ll 1$ are *weakly* coupled, as in stars more massive than slightly sub-solar.

As one can suspect, Γ is the dimensionless coupling parameter according to which one can classify theories. Weakly-coupled plasmas lend to systematic perturbative ideas (*e.g.* in powers of Γ), strongly coupled plasma need more creative treatments. Improvements in the equation of state beyond the model of a mixture of ideal gases are difficult, both for conceptual and technical reasons.

2.1. Chemical and Physical Picture

The present comparison is not merely between two EOS-projects, but also between two fundamentally different approaches to the problem. The *chemical picture* is named for its foundation in the notion of a chemical equilibrium between a set of pre-defined molecules, atoms and ions.

In the *physical picture* only the "elementary" particles of the problem are assumed from the outset — that is, nuclei and electrons. Composite particles appear from the formulation.

2.1.1. Chemical Picture: MHD EOS

Most realistic equations of state that have appeared in the last 30 years belong to the chemical picture and are based on the free-energy minimization method. This method uses approximate statistical mechanical models (for example the non-relativistic electron gas, Debye-Hückel theory for ionic species, hard-core atoms to simulate pressure ionization via configurational terms, quantum mechanical models of atoms in perturbed fields, *etc.*). From these models a macroscopic free energy is constructed as a function of temperature T, volume V, and the particle numbers $N_1, \ldots, N_m$ of the m components of the plasma. At given T and V, this free energy is minimized subject to the stoichiometric constraints. The solution of this minimum problem then gives both the equilibrium concentrations and, if inserted in the free energy and its derivatives, the equation of state and the thermodynamic quantities.

Obviously, this procedure automatically guarantees thermodynamic consistency. As an example, when the Coulomb pressure correction (see Sect. 2.2) to the ideal-gas contribution originates from the free energy (and not merely as a correction to the pressure), there will be corresponding terms in all the other thermodynamic variables, as well as changes to the equilibrium concentrations. One major advantage of using the chemical picture lies in the possibility to model complicated plasmas, and to obtain numerically smooth and consistent thermodynamical quantities.

In the chemical picture, perturbed atoms must be introduced on a more-or-less *ad-hoc* basis to avoid the familiar divergence of internal partition functions (see *e.g.* Ebeling et al. 1976). In other words, the approximation of unperturbed atoms precludes the application of standard statistical mechanics, *i.e.* the attribution of a Boltzmann-factor to each atomic state. The conventional remedy is to modify the atomic states, *e.g.* by cutting off the highly excited states in function of density and temperature.

The MHD equation-of-state is based on an occupation probability formalism (Hummer & Mihalas 1988), where the internal partition functions $Z_s^{\rm int}$ of species s are weighted sums

$$Z_s^{\rm int} = \sum_i w_{is} g_{is} \exp\left(-\frac{E_{is}}{k_{\rm B}T}\right) \ . \qquad (2)$$

Here, is label state i of species s, and E_{is} is the energy and g_{is} the statistical weight of that state. The coefficients w_{is} are the occupation probabilities that take into account charged and neutral surrounding particles. In physical terms, w_{is} gives the fraction of all particles of species s that can exist in state i with an electron bound to the atom or ion, and $1 - w_{is}$ gives the fraction of those that are so heavily perturbed by nearby neighbors that their states are effectively destroyed. Perturbations by neutral particles are based on an

excluded-volume treatment and perturbations by charges are calculated from a fit to a quantum-mechanical Stark-ionization theory (for details see Hummer & Mihalas 1988).

The Opacity Project and, with it, the MHD equation-of-state restricts itself to the case of stellar envelopes, where density is sufficiently low that the concept of atoms makes sense. This was the main justification for realizing the Opacity-Project in the chemical picture and base it on the Mihalas, Hummer, Däppen equation of state (Hummer & Mihalas 1988; Mihalas et al. 1988; Däppen et al. 1988, hereinafter MHD). The Opacity Project is mainly an effort to compute accurate atomic data, and to use these in opacity calculations. Plasma effects on occupation numbers are of secondary interest.

2.1.2. Physical Picture: OPAL EOS

The chemical pictures heuristic separation of the atomic-physics from the statistical mechanics is avoided in the physical picture. It starts out from the grand canonical ensemble of a system of electrons and nuclei interacting through the Coulomb potential (Rogers 1981b, 1986, 1994). Bound clusters of nuclei and electrons, corresponding to ions, atoms and molecules are sampled in this ensemble. Any effects of the plasma environment on the internal states are obtained directly from the statistical mechanical analysis, rather than by assertion as in the chemical picture.

There is an impressive body of literature on the physical picture. Important sources of information with many references are the books by Ebeling et al. (1976), Kraeft et al. (1986), and Ebeling et al. (1991). However, the majority of work on the physical picture was not dedicated to the problem of obtaining a high-precision equation of state for stellar interiors. Such an attempt was made for the first time by the OPAL-team at Lawrence Livermore National Laboratory (Rogers 1986; Iglesias & Rogers 1995; Rogers et al. 1996, and references therein), and used as a foundation for the OPAL opacities (Iglesias et al. 1987, 1992; Iglesias & Rogers 1991; Iglesias & Rogers 1996; Rogers & Iglesias 1992).

The OPAL approach avoids the *ad-hoc* cutoff procedures necessary in free energy minimization schemes. The method also provides a systematic procedure for including plasma effects in the photon absorption coefficients. An effective potential method is used to generate atomic data which have an accuracy similar to single configuration Hartree-Fock calculations (Rogers 1981a).

In contrast to the chemical picture, plagued by divergent partition functions, the physical picture has the power to avoid them altogether. Partition functions of bound clusters of particles (*e.g.* atoms and ions) are divergent in the Saha approach, but has a compensating divergent scattering state part in the physical picture (Ebeling et al. 1976; Rogers 1977). A major advantage of the physical picture is that it incorporates this compensation at the outset. A further advantage is that no assumptions about energy-level shifts have to be made; it follows from the formalism that there are none.

As a result, the Boltzmann sum appearing in the atomic (ionic) free energy is replaced by the so-called Planck-Larkin partition function (PLPF), given by (Ebeling et al. 1976; Kraeft et al. 1986; Rogers 1986)

$$\mathrm{PLPF} = \sum_{is} g_{is} \left[\exp\left(-\frac{E_{is}}{k_{\mathrm{B}}T} \right) - 1 + \frac{E_{is}}{k_{\mathrm{B}}T} \right] .$$

The PLPF is convergent without additional cut-off criteria as are required in the chemical picture. We stress, however, that despite its name the PLPF is not a partition function, but merely an auxiliary term in a virial coefficient (see, *e.g.*, Däppen et al. 1987).

The major disadvantage of the physical picture, is its formulation in density expansions. Expansions that first of all are very cumbersome to carry out, which means that only terms up till $\frac{5}{2}$ in density have been evaluated (Alastuey & Perez 1992; Alastuey et al. 1994, 1995). Second, the slow convergence of the problem, means that even this extraordinary accomplishment has a rather limited range of validity. The chemical picture, on the other hand, do not need to rely on expansions, and complicated expressions, possibly with the correct asymptotic behavior, can be used freely.

2.2. The Coulomb correction

The Coulomb correction, that is, the consequence of an overall attractive binding force of a neutral plasma deserves close attention, because it describes the main truly non-ideal effect un-

der conditions as found in the interior of normal stars. Already in a number of early papers (*e.g.* Berthomieu et al. 1980; Ulrich 1982; Ulrich & Rhodes 1983; Shibahashi et al. 1983, 1984) it was suggested that improvements in the equation of state, especially the inclusion of a Coulomb correction, could reduce discrepancies between computed and observed p-modes in the Sun. Responding to this, Christensen-Dalsgaard et al. (1988), showed that the MHD equation of state indeed improved the agreement with helioseismology. That the largest change was caused by the Coulomb correction was not immediately clear, since the MHD equation of state also incorporates other improvements over previous work.

From early comparisons between the MHD and OPAL equations of state (Däppen et al. 1990), it turned out, rather surprisingly, that the net effect of the other major improvement, the influence of hydrogen and helium bound states on thermodynamic quantities, became to a large degree eclipsed beneath the influence of the Coulomb-term. In the solar hydrogen and helium ionization zones the Coulomb-term is the dominant correction to the ionizing perfect gas. This discovery led to an upgrade of the simple, but astrophysically useful Eggleton et al. (1973) (EFF) equation of state through the inclusion of the Coulomb interaction term (CEFF) (see Christensen-Dalsgaard 1991; Christensen-Dalsgaard & Däppen 1992).

The leading-order Coulomb correction is given by the Debye-Hückel (DH) theory, which replaces the long-range Coulomb potential with a screened potential, as outlined below.

2.2.1. The Debye-Hückel approximation

The Debye & Hückel (1923) theory of electrolytes, describes polarization in liquid solutions of electrons and positive ions. This description also applies to ionizing gases. Assuming the particles can move freely, the electrons will congregate around the ions, and the ions will repel each other due to their charges. With their smaller mass and higher speeds, the paths of electrons are deflected by the ions increasing the chance of finding an electron closer to an ion. This screening by the electrons decreases the repulsion between the ions, acting as an overall attractive force in the plasma.

The fundamental assumption of Debye and Hückel is that of statistical equilibrium, according to which the local density of particles of type j (including electrons) immersed in a potential ψ around an ion, i, can be expressed as

$$n_j(\boldsymbol{r}_i) = \langle n_j \rangle \exp(-Z_j e\psi(\boldsymbol{r}_i)/k_{\rm B}T) \ , \quad (3)$$

where $Z_j e$ and $\langle n_j \rangle$ are the charge and mean density of the particles and $n_j(\boldsymbol{r})$ are the perturbed densities. $\psi(\boldsymbol{r})$ is the plasma-potential or the effective (screened) inter-particle potential. Over-all charge neutrality dictates that

$$\sum_j \langle n_j \rangle Z_j = 0 \quad \Leftrightarrow \quad \langle n_{\rm e} \rangle = \sum_{j \neq {\rm e}} \langle n_j \rangle Z_j \ . \quad (4)$$

With these perturbed densities, the corresponding charge density is

$$\begin{aligned} \rho(\boldsymbol{r}_i) &= \sum_j Z_j e \langle n_j \rangle e^{-Z_j e\psi(\boldsymbol{r}_i)/k_{\rm B}T} + Z_i e\delta(\boldsymbol{r}_i) \\ &= \sum_{j \neq {\rm e}} Z_j e \langle n_j \rangle \left[e^{-Z_j e\psi(\boldsymbol{r}_i)/k_{\rm B}T} - e^{e\psi(\boldsymbol{r}_i)/k_{\rm B}T} \right] + Z_i e\delta(\boldsymbol{r}_i) \end{aligned}$$

resulting in the Poisson equation

$$\nabla^2 \psi(\boldsymbol{r}_i) = -4\pi e \left[\sum_j Z_j \langle n_j \rangle e^{-Z_j e\psi(\boldsymbol{r}_i)/k_{\rm B}T} + Z_i \delta(\boldsymbol{r}_i) \right] \ . \quad (6)$$

And now comes the most critical of Debye's approximations: To make Eq. (6) more tractable, the exponential is expanded in a power series, and only terms up to first order are retained. The zero-order term is the net-charge, Eq. (4). Solving Eq. (6) with the remaining first-order terms results in a screened Coulomb potential—the *Debye-Hückel potential*

$$\psi(r) = \frac{Ze}{r} e^{-r/\lambda_{\rm DH}} \ , \quad (7)$$

where $\lambda_{\rm DH}$ is the Debye-length

$$\lambda_{\rm DH}^{-2} = \frac{4\pi e^2}{k_{\rm B}T} \sum_i Z_i^2 n_i \ . \quad (8)$$

The approximation of disregarding higher order terms affects the low temperature and high density region where the inter-particle interactions becomes too large to be described by just the first order term. This is a manifestation of the problems with the classical, long-range part of the Coulomb field in a plasma.

Investigations taking the physical picture point of view indicate that the original potential defined in (6), is a good choice for a plasma potential (Rogers 1981b), and only the truncation of the exponential resulting in the Debye-Hückel potential is of limited validity (Rogers 1994)

At high densities the effect is in fact over-estimated by using the Debye-Hückel potential (7). The relative Coulomb pressure in the Debye-Hückel theory, expressed in terms of the coupling parameter, $p_{\rm DH}/k_{\rm B}T = -\Gamma^{3/2}/\sqrt{12}$, is a negative contribution to the pressure. At very high densities, the over-estimation of the Coulomb pressure can be so severe as to result in a negative total pressure. The negative pressure differences seen in the comparison plots in Sects. 3 and 4, suggests that the amplitude of the Coulomb pressure is larger in OPAL than in MHD. This statement is true when the τ-correction, mentioned below, is applied to the MHD EOS.

To get a feeling for the behavior of the Coulomb pressure, we use the perfect gas law to obtain the approximate expression

$$\Gamma \propto R^{1/3}\mu^{-1/3}\langle Z^2\rangle^{1/3} , \qquad (9)$$

where μ is the mean-molecular weight. This leads us to anticipate differences between OPAL and MHD, stemming from different treatments of the plasma interactions, to increase with R, and that such differences will be somewhat reduced when we mix in helium and metals.

2.2.2. *The τ correction in DH theory*

As they were investigating electrolytic solutions of molecules under terrestrial conditions, it was natural for Debye and Hückel to consider electrolytes made up of hard spheres. Assuming there is a *distance of closest approach*, $r_{\rm min}$ to the ion, Eq. (7) is modified to

$$\psi(r) = \frac{Ze}{1 + r_{\rm min}/\lambda_{\rm DH}} \frac{e^{-(r-r_{\rm min})/\lambda_{\rm DH}}}{r} , \qquad (10)$$

for $r \geq r_{\rm min}$ and constant, $\psi(r_{\rm min})$, inside, removing the short range divergence. To obtain the free energy, we apply the so-called *recharging* procedure detailed in Fowler & Guggenheim (1956) to Eq. (10), and get the result without $r_{\rm min}$, multiplied by the factor

$$\tau(x) = 3[\ln(1+x) - x + \frac{1}{2}x^2]x^{-3} , \qquad (11)$$

where $x = r_{\rm min}/\lambda_{\rm DH}$. In short, the recharging procedure consists of varying all charges in the potential and integrating from zero to full charge. Equation (11) is the analytical result of this integration and is based on the assumption that $r_{\rm min}$ is independent of the charge of any particles. The τ-factor goes from one to zero as x increase, reducing the Coulomb pressure which was overestimated before. With the τ correction we can avoid the negative pressures mentioned above.

Graboske et al. (1969) proposed to use

$$r_{\rm min} = \langle Z\rangle e^2 \left[k_{\rm B}T\frac{F_{3/2}(\eta_{\rm e})}{F_{1/2}(\eta_{\rm e})}\right]^{-1} , \qquad (12)$$

for stellar plasmas, and it was later used in the MHD EOS but not in OPAL. This choise of $r_{\rm min}$ is merely the distance of equipartition between thermal and potential energy of electrons approaching ions. Since the charges are opposite there are, however, no classical limits to their approach. Also notice that since this choice of $r_{\rm min}$ depends explicitly on charge, the recharging procedure will result in a different form of τ.

A thorough and critical review of the Debye-Hückel theory can be found in Fowler & Guggenheim (1956), Chp. IX, and a very clear presentation is found in Kippenhahn & Weigert (1992), though the latter does not mention τ.

2.2.3. *Other higher-order Coulomb corrections*

Obviously, the τ correction is just one particular higher-order Coulomb correction. We can use it as a model for developing more general expressions, by allowing some liberty in the choice of $r_{\rm min}$. Let us begin by asking about the distance of closest approach for quantum-mechanical electrons. Heisenberg's uncertainty relation puts firm limits on how localized particle can be — it is smeared out over a volume the size of a de Broglie wavelength $\lambda = \hbar/p$. This de-localization eliminates the infinite charge densities associated with classical point-particles, and hence the short-range divergence of the Coulomb potential.

Based on that, we can tentatively suggest a distance of closest approach which is the combined radii of the electron and ion: $\frac{1}{2}\lambda_{\rm e} + \frac{1}{2}\langle\lambda_{\rm ion}\rangle$. The diffraction parameter, γ_{ij}, between two particles i and j, emerging from a more careful quantum-mechanical analysis implies the use of the De-

Broglie wavelength in relative coordinates

$$r_{\rm min} = \lambda_{\rm ij} = (\hbar^2/2\mu_{\rm ij}k_{\rm B}T)^{1/2} \propto T^{-1/2} \ , \quad (13)$$

where μ_{ij} is the reduced mass. Comparing the τ-function with the quantum diffraction modification in Fig. 5 of (Rogers 1994), we see a similarity in the functional form. The asymptotic behavior differs though: $\tau(x) \rightarrow x^{-1}$ for $x \rightarrow \infty$ in the hard-sphere model, whereas quantum diffraction goes as $x^{-1/2}$. The two functions are very close up to $x \simeq 1$, though, suggesting that preliminary investigations of quantum diffraction effects in the MHD EOS could be carried out by means of the τ-function and a new $r_{\rm min}$ as given by Eq. (13).

Dividing Eq. (13) by $\lambda_{\rm DH}$, we find that the correction is now a function of ϱ only. That is, going from a hard-sphere model of interactions, to including quantum diffraction, the factor alleviating the short-range divergence of the Coulomb potential becomes a function of ϱ instead of R.

Abandoning the hard-sphere ion correction for the benefit of quantum diffraction, still leaves us with only the first term of the Coulomb interactions. Could the higher order terms be represented by τ in some form? It turns out that τ would only fit in a very limited range, and it would be more fruitful to use proper expressions. The present analysis however, shows that the effect of including higher-order Coulomb terms, is much smaller than has previously been estimated by the MHD EOS. It therefore might be a fair approximation to leave them out for at least the solar case.

3. The EOS landscape in ϱ and T

For this comparison, we have computed MHD EOS tables with exactly the same ϱ/T-grid points as the OPAL-tables (Rogers et al. 1996), to ensure that the equation-of-state comparison is not influenced by interpolation errors. We do actually use the respective interpolation routines to access the table-values, but by interpolating on the exact gridpoints for identical mixtures, we should not lose precision in the process.

We compare tables with three different chemical mixtures, successively adding more elements to the plasma: Mix 1 is pure hydrogen, mix 2 a hydrogen-helium mixture and mix 3 is a 6-element mixture that, besides hydrogen and helium, also includes C, N, O and Ne. In Table 1 we list the exact mixtures, both by mass abundance, X_i, of chemical element, i, and as logarithmic number fractions relative to hydrogen $[N_i/N_H]$. The choice of mixtures is that of the currently available OPAL-tables, to avoid interpolations in X and Z. In the comparisons of this section, we have omitted the radiative contributions.

The MHD equation of state now includes relativistically degenerate electrons, (Gong et al. 2001b) as do the new version of OPAL (Rogers & Nayfonov 2002). This, of course, is significant for stellar modeling and important for helioseismic investigations of the Solar radiative zone (Elliot & Kosovichev 1998). For the present paper, however, it is irrelevant due to the lack of controversy on the subject, and we will therefore limit ourselves to dealing with non-relativistic electrons.

All plots of differences in this paper present absolute differences. Since the absolute quantities span less than an order of magnitude and as they have quite complicated behaviors, we found that normalizing the differences would confuse more than illuminate. The solar track (also presented in Sect. 4) overlaid on the surface plots is not hidden behind the surface, so as to give an idea of the behavior in otherwise obscured regions.

While the MHD tables and the pure-hydrogen OPAL table have the same resolution, Mix-2 and Mix-3 OPAL tables have three times higher resolution both in T and ϱ. This can only affect the comparisons of the solar Mix 2 and 3 cases, Sect. 4, where it might introduce some extra interpolation-wiggles in the OPAL-MHD differences. The table comparisons are all done on the low resolution grid.

For the case of pure hydrogen (Mix 1) we plot the logarithmic absolute pressure, but for the other mixtures we plot the logarithm of a reduced pressure, $P/(\varrho T)$, to make it easier to identify non-ideal effects and the location of ionization zones. This choice will of course not affect the differences of the logarithms.

Apart from the actual pressure we also investigate the three derivatives

$$\chi_\varrho = \left(\frac{\partial \ln P}{\partial \ln \varrho}\right)_T \ , \quad \chi_T = \left(\frac{\partial \ln P}{\partial \ln T}\right)_\varrho \ , \text{and} \quad \gamma_1 = \left(\frac{\partial \ln P}{\partial \ln T}\right)_S \ , \quad (14)$$

where γ_1 is the adiabatic derivative often called Γ_1. These three derivatives form a complete set

TABLE 1
CHEMICAL MIXTURES 2 AND 3 (SEE TEXT)

element	$X_i(\%)$	$[N_i/N_{\rm H}]$	$X_i(\%)$	$[N_i/N_{\rm H}]$
H	80.00	0.00000	80.00	0.00000
He	20.00	-1.20098	16.00	-1.29789
C	0.00	—	0.762643	-3.09693
N	0.00	—	0.223398	-3.69693
O	0.00	—	2.171950	-2.76693
Ne	0.00	—	0.842053	-3.27923

and fully describe the equation of state.

3.1. Pure hydrogen

We start with the simplest mixture, that is, pure hydrogen (Mix 1). The case of hydrogen is, however, far from simple, not the least because of its negative ion and molecular species. All in all five species of hydrogen: H, H^+, H^-, H_2 and H_2^+ are included in both EOS.

The number of negative hydrogen ions does never exceed a few parts in a thousand compared to the other hydrogen species. Already at moderate temperature, they dissociate into hydrogen atoms. Despite its low abundance, H^- does have an impact on the electron balance since it is the only (significant) electron sink. The heavy elements with their low abundances are most affected by this. Apart from this indirect effect on the heavy elements, the most important feature of the H^--ion is of course its bound-free and free-free opacity, which is the primary source of opacity in atmospheres of G, K and M stars.

The positive and neutral hydrogen molecules can be seen in the low-temperature-high-density corner of the tables, where their abundance reaches up to 28% of hydrogen, by mass. At slightly lower densities, which is of greater astrophysical interest, these molecules only become important at temperatures below those considered here.

The most important feature in the hydrogen-EOS landscapes of Figs. 1–4 is, by far, the ionization (from atom to positive ion), seen as a curved rift in all the derivatives. It is hardly visible in the surface-plot of the full pressure (Fig. 1), but becomes obvious in those of the reduced pressure (Figs. 5 and 9).

The OPAL-team introduced the quantity

$$R = T_6^3 \varrho^{-1} \,, \tag{15}$$

where $T_6 = T/10^6$, as a convenient quantity to describe the approximate $\varrho - T$-stratification of many stars. This is clearly seen in Fig. 1 where we also plotted three iso-R tracks, bracketing the solar track. In the lower panel of Fig. 1 these iso-R tracks also highlight the main feature in the differences: A sharply rising ridge, bell-shaped in $\log T$ and centered around $\log T = 5.5$, lying along $\log R \simeq 0$. This ridge is a signature of differences in the pressure ionization. The sign of ΔP in Fig. 1 tells us that MHD has a more abrupt pressure ionization than the softer OPAL. The reason for this difference is still not completely clear. It might be related to differences in the treatment of the short-range suppression of the Coulomb forces, as mentioned in Sect. 2.2.2 and 2.2.3, or it could be a result of differences in the mechanism of pressure ionization (Iglesias & Rogers 1995; Basu et al. 1999; Gong et al. 2001a).

We now turn to the logarithmic pressure derivatives, χ_ϱ and χ_T, displayed in Fig. 2 and 3, respectively. In both figures, the ionization zone is easily recognized as the canyon or ridge starting in the low-temperature-low-density corner, slowly bending over to follow the solar track and disappear at about $\log T = 6$.

In quite a large region of the $\varrho - T$ plane both derivatives are equal to one reflecting that the gas is a perfect gas. In this region the differences are very small (*i.e.* less than 0.03%), confirming that

both the chemical and the physical picture converges appropriately to the perfect gas case.

At low temperatures χ_ϱ and χ_T are dominated by temperature ionization, which is about an order of magnitude more prominent in χ_T than in χ_ϱ. This region is a fairly well known regime and here we can directly compare the two pictures. The differences are indeed small in this region, less than 1% and less than a tenth of the differences in the high-R ridge.

The rise of χ_T in the low-T-high-ϱ corner is due to H_2-molecules. About 28% by mass, of the hydrogen atoms are bound in molecules in this region, but at higher densities they quickly pressure dissociate. The fact that the differences increase while the absolute value decreases indicates that MHD is pressure dissociating faster than OPAL.

The differences are again dominated by the sharp ridge at high R, but in contrast to pressure (Fig. 1), the differences in χ_ϱ and χ_T return to zero for high temperatures and densities. As for pressure, the solar track falls over or climbs the R-edge in the middle of the ionization zone, as it is traversing the iso-R at $\log R \simeq 0$.

These high-R differences occur in a region where there is competition between the Coulomb terms and electron degeneracy. This makes the interpretation much more difficult. Two possible reasons are the previously mentioned short-range

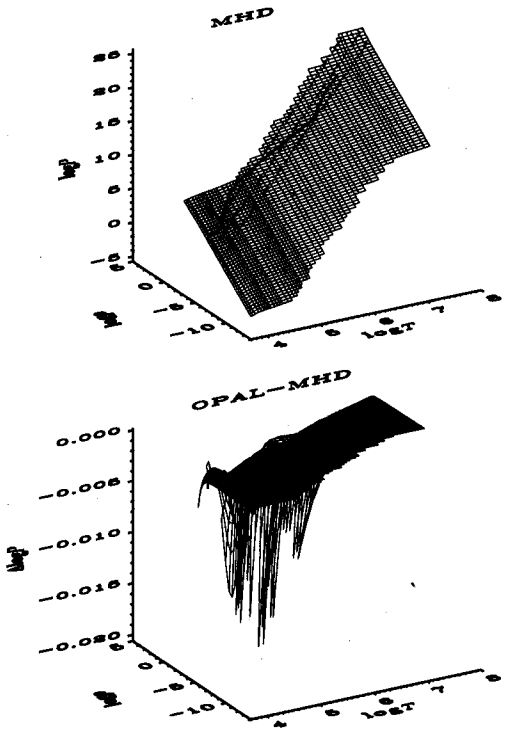

Fig. 1.— Comparison of $\log_{10}P$ in the two pure hydrogen tables. The upper panel shows the absolute value from the MHD EOS and the lower panel shows the difference; OPAL minus MHD. The strange boundaries of the surface simply reflects the shape of the tables. We also overlay the solar track from Sect. 4 for comparison. On this plot alone we also show iso-R tracks (dotted lines) for $\log_{10}R = -2, -1, 0$, going from low to high densities.

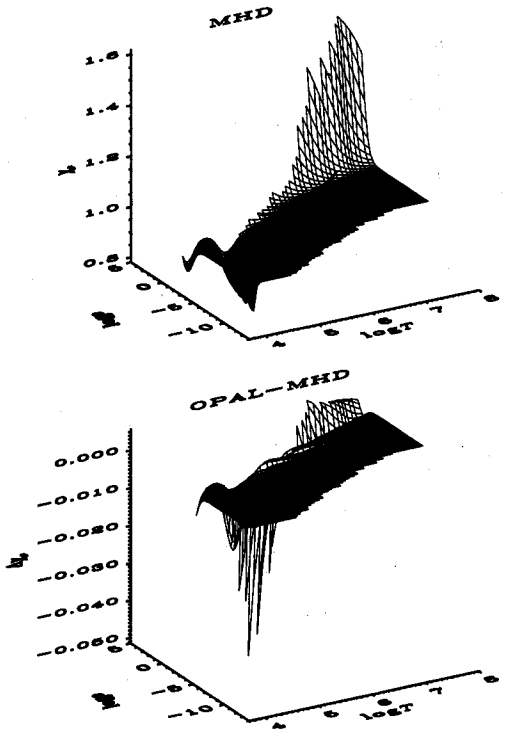

Fig. 2.— The logarithmic pressure derivative with respect to density $\chi_\varrho = (\partial \ln P/\partial \ln \varrho)_T$ for pure hydrogen in the upper panel, and its differences (OPAL minus MHD) in the lower panel.

part of the Coulomb interactions and the changes induced in the internal atomic states by the dense, perturbing surroundings.

In the MHD EOS, all energy levels of internal states are assumed to be unaltered by the plasma environment. That is, the effect of the perturbation by surrounding neutral and charged particles on the internal state is restricted to a lowering of the occupation probability of the given state only. In the OPAL EOS, the net result looks similar, but there the relative stability of energy levels to perturbations is not merely postulated but the result of in-situ calculations of the Schrödinger or Dirac equation for each configuration of nuclei and electrons, based on parameterized Yukawa potentials (Rogers 1981a), as mentioned in Sect. 2.1.2.

Looking at γ_1 in Fig. 4 we immediately notice how well this quantity displays the ionization zones while leaving out everything else. This property is also reflected in the differences, which here are of about the same magnitude in the ionization zone as in the high-R ridge. The high-R differences have also changed characteristics, changing sign periodically, while retaining the overall bell-shape in log$T$ of the amplitude. We mention, however, that at least some of this behavior might be due to the numerical differentiation scheme used in the OPAL EOS (see Sect. 5 and Fig. 25).

3.2. Hydrogen and helium mixture

The effect of helium in the thermodynamical quantities is revealed by the addition of 20% helium and comparison with the pure-hydrogen case.

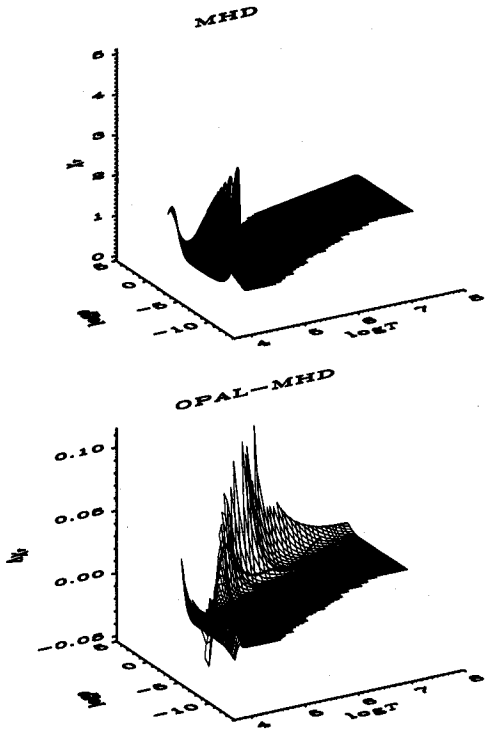

Fig. 3.— The logarithmic pressure derivative with respect to temperature $\chi_T = (\partial \ln P/\partial \ln T)_\varrho$ for pure hydrogen in the upper panel, and its differences (OPAL minus MHD) in the lower panel.

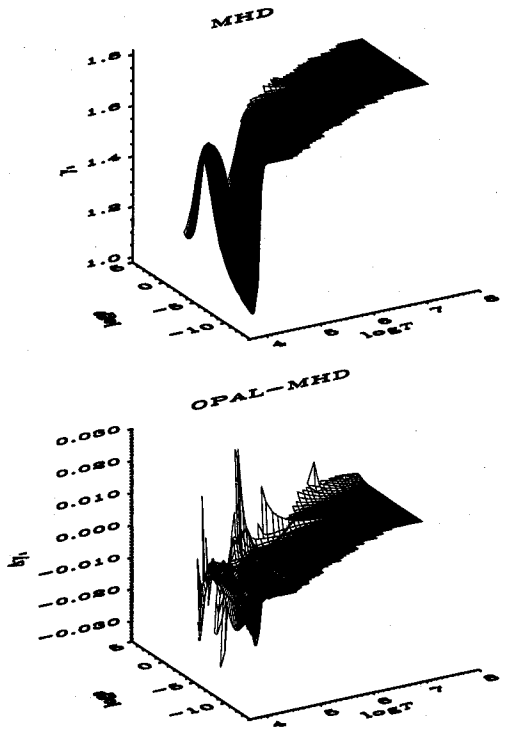

Fig. 4.— The adiabatic logarithmic pressure derivative with respect to density $\gamma_1 = (\partial \ln P/\partial \ln \varrho)_S$ for pure hydrogen in the upper panel, and its differences (OPAL minus MHD) in the lower panel.

The first thing we notice from Fig. 5 is how well the reduced pressure $P/(\varrho T)$ reveals all the dissociation and ionization zones (except H^-); The H_2-formation in the low-T-high-ϱ corner and the prominent ionization of hydrogen together with the two He ionization zones, the first eventually merging with the H ionization. The effect of degenerate electrons is evident in the high-T-high-ϱ corner.

We also notice another thing: while the pure hydrogen OPAL-table was cutting the high-ϱ, low-T corner, leaving a little less for the comparison, the mixture OPAL-tables allow a full comparison since they have the same boundaries as the MHD tables. The slightly larger table reveals a new feature in the differences. For pure hydrogen, the pressure difference drops suddenly in the high-ϱ, low-T corner, due to faster molecule formation in OPAL as compared to MHD. But in the slightly larger tables used for the remainder of this section, this difference suddenly goes to zero before it falls down the high-R edge.

In the pressure differences, one can just barely identify the first helium ionization zone, whereas the second is too faint to be seen here. The high-R differences are a little smaller than for pure hydrogen, as anticipated from Eq. (9) and the discussion following it. This can be most clearly seen by comparing the dip in the hydrogen ionization zone.

The addition of helium is also evident in the logarithmic pressure derivatives in Fig. 6 and 7. First we see the deep rift (ridges in Fig. 7) of the hydrogen ionization zone. Then comes a small groove from the first helium ionization zone, a groove which, when it widens and gets shallower at higher densities, eventually merges with the hydrogen ionization zone, as is the case for the solar track. Widely separated from the hydrogen and first helium ionization zones, we find the second helium ionization zone. It seems to disappear at the low density edge of the table, but that is only so because the ridge gets very sharp and is unresolved in temperature, at low densities. Hotter stars, that is, stars shifted towards lower R, will clearly exhibit three, more distinct ionization zones when compared with the Sun.

Apart from the two helium ionization zones, the differences in the pressure derivatives are very similar to the pure hydrogen case. The high-R differences are somewhat smaller though, as are the differences in the hydrogen ionization zone. The differences in χ_ϱ also displays a very small ripple along $\log R \simeq -4$, which might be due to differences in the differentiation technique (see Sect. 5).

From the differences in χ_T (Fig. 7), we see that the absolute differences in the three ionization zones are just about the same. If we instead compare the differences relative to the size of the respective ionization ridges, we get 0.16% and 3% relative differences for the hydrogen and helium ionization zones respectively. That is, MHD and OPAL have about 20 times better agreement on hydrogen than on helium.

In Fig. 8, γ_1 appears like what we would anticipate from the pure hydrogen case in Fig. 4. The first helium ionization zone is only visible at low densities, as it merges with the hydrogen ioniza-

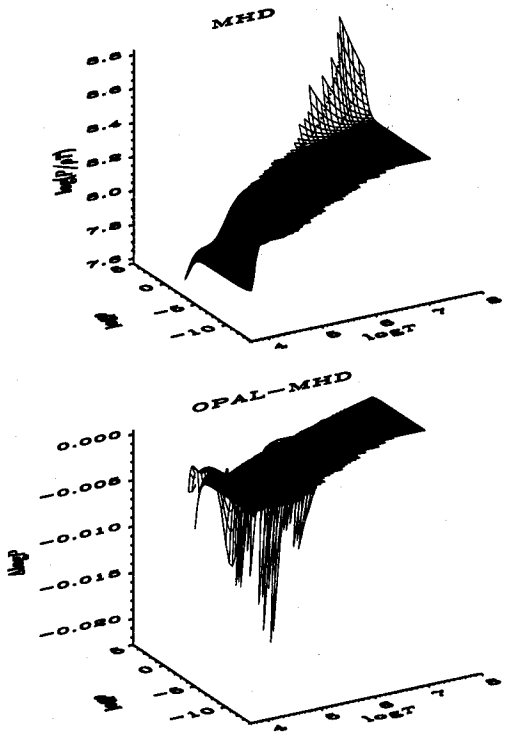

Fig. 5.— The reduced pressure, $P/(\varrho T)$, for the H-He mixture in the upper panel, and its differences (OPAL minus MHD) in the lower panel.

tion zone shortly before the solar track is reached.

The differences, however, exhibit a much more complicated structure. Along each of the ionization zones, there is a deep valley in the differences, and along the bottom of these valleys runs a very sharp ridge, bringing the differences up to positive values. This is a clear sign of a broad negative peak minus a sharp negative peak, meaning that MHD temperature ionize faster than does OPAL. In the beginning of this section, we found that MHD was also pressure ionizing faster than OPAL, so all in all OPAL is the softer EOS of the two. The ridge-in-the-middle-of-the-valley picture is also found in the pure hydrogen case (Fig. 4), but as the hydrogen ionization zone is not fully covered at low densities, the low-T side of the valley is missing.

3.3. H,He,C,N,O and Ne mixture

In this section we add the last four elements considered, namely carbon, nitrogen, oxygen and neon. Comparing Figs. 9-11 of this section with the corresponding Figs. 5-7 of the previous section, hardly any differences appear, neither in the absolute values nor in the differences between the two EOS.

For a few points on the high-R boundary of the tables, differences in χ_ϱ and γ_1 have increased dramatically. At least some of these odd points are the same for χ_ϱ and γ_1. This might indicate that these points are spurious, possibly associated with convergence problems in either EOS in this difficult region.

The heavy elements are just barely discernible in the differences of χ_ϱ (Fig. 11). However, for γ_1,

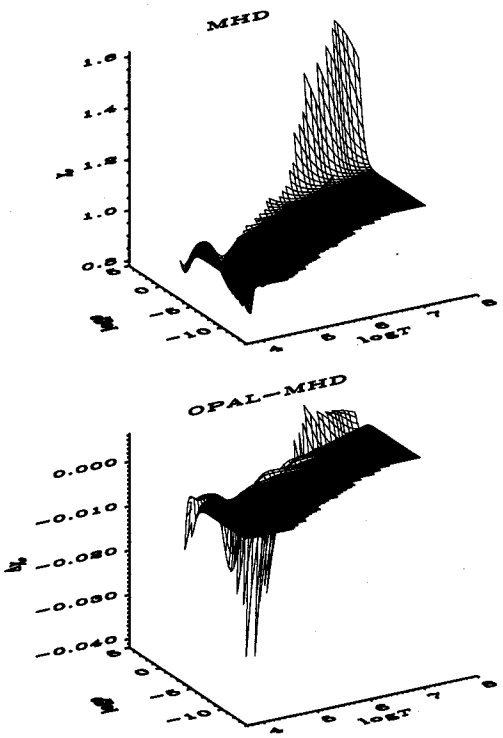

Fig. 6.— χ_ϱ, the logarithmic pressure derivative at constant temperature, for the H-He mixture in the upper panel, and its differences (OPAL minus MHD) in the lower panel.

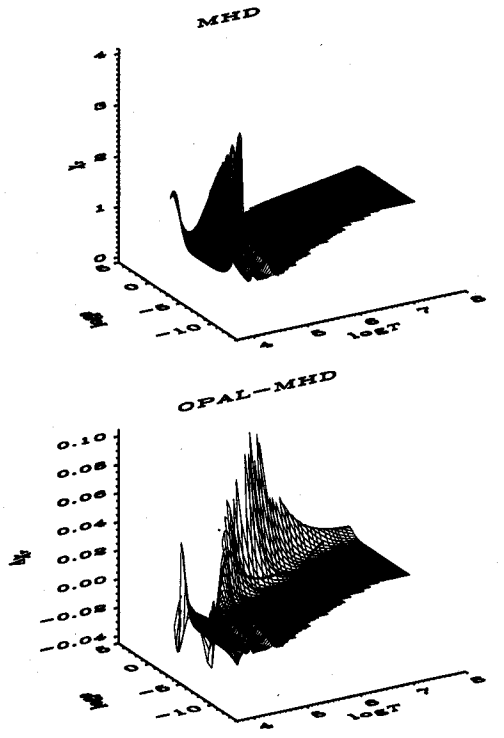

Fig. 7.— χ_T, the logarithmic pressure derivative at constant density, for the H-He mixture in the upper panel, and its differences (OPAL minus MHD) in the lower panel.

in Fig. 12, the heavy elements appear clearly both in the absolute γ_1 and in the γ_1 differences, especially along the low-ϱ edge of the table. Between the first and second ionization zones of helium (*cf.* Fig. 8), we notice some wiggles, which are likely resulting from the third ionization zones of carbon and nitrogen, and the second ionization zones of oxygen and neon. Above the second ionization zone of helium, we can see all the ionization zones from the fourth ionization zone of carbon right up to the tenth ionization of neon, although they are not all resolved in this ϱ-T-grid. A rough estimate reveals that the relative difference between MHD and OPAL for the heavy elements is of about the same magnitude as the one for the helium ionization zones, *i.e.* 3%, or about 20 times worse than the 0.16% agreement for hydrogen.

This unexpectedly large discrepancy for the heavy elements might be a hint that these differences are primarily caused by differences in the lower excited states. For hydrogenic ions, there are analytical solutions for all states. This might explain the small discrepancy for hydrogen. For ions with more than one electron there are no analytical treatments, except for their higher states, which become nearly hydrogenic. So it might well be that the lower lying states of the non-hydrogenic ions are responsible for the differences noticed here. The Yukawa potentials (Rogers 1981a), which are used to describe bound electron states in OPAL, are fitted to give the correct (experimental) ionization energies. MHD uses experimental results for the energy levels. It is no surprise therefore to get quasi-perfect agreement on the location of the ionization zones (confirmed by the ridge-in-the-middle-of-the-valley picture in the γ_1 differences), whereas the energies of lower lying excitation levels might differ These differences

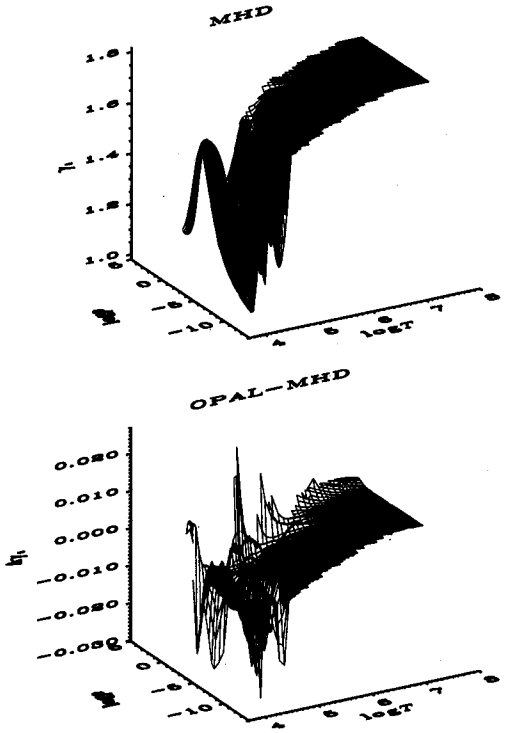

Fig. 8.— γ_1 for the H-He mixture in the upper panel, and its differences (OPAL minus MHD) in the lower panel.

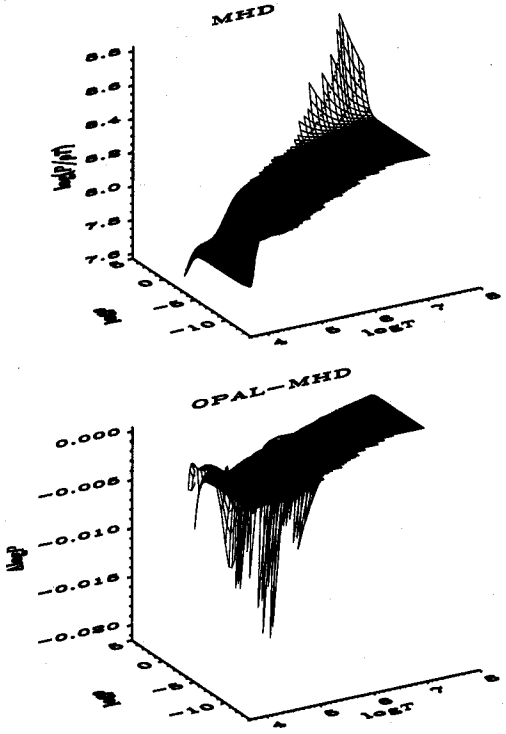

Fig. 9.— Reduced pressure for mixture 3 (*cf.* Tab. 1) in the upper panel, and its differences (OPAL minus MHD) in the lower panel.

propagate into the partition functions and affect the course of ionization. In addition, the differences in the adopted micro-field distribution, and the mechanism by which they ionize highly excited states, might play a rôle in this region (Nayfonov & Däppen 1998; Nayfonov et al. 1999). Since the differences occur at the low-ϱ edge of the table, we expect however, that they mainly reveal differences in the thermal ionization, not in pressure ionization.

Let us return to pressure and have a closer look at the non-ideal effects in the high-T-high-ϱ corner. From the dotted iso-R lines in Fig. 9, it is clear that the non-ideal effects are not functions of R alone. Instead it turns out that they are largely functions of ϱ^2/T^3. Comparing the perfect gas pressure and the fully degenerate, non-relativistic electron pressure

$$P_{\rm perf} = \frac{\varrho k_{\rm B} T}{\mu m_{\rm u}} \quad \text{and} \quad P_{\rm e}^{\rm deg} = \frac{1}{5}\left(\frac{3}{8\pi}\right)^{2/3} \frac{h^2}{m_{\rm e}} \left(\frac{\varrho}{\mu_{\rm e} m_{\rm u}}\right)^{5/3},$$

we see that the two pressures compete along $\varrho^2 \propto T^3$-lines. This means that relative to high-R (Coulomb) effects, there are more degeneracy effects in the high-T-ϱ corner of the table, which reveals the nature of the sharp rise of both P and χ_ϱ in this region. The correlation with larger OPAL−MHD differences (See lower panel of Fig. 9) prompted us to perform a direct comparison between the Fermi-Dirac integrals from the two codes. We found non-systematic differences a reassuring eight orders of magnitude smaller than the EOS differences we observe in this region.

An alternative explanation could be the lack of electron exchange effects in the MHD EOS. This is a combined effect of Heisenberg's uncertainty

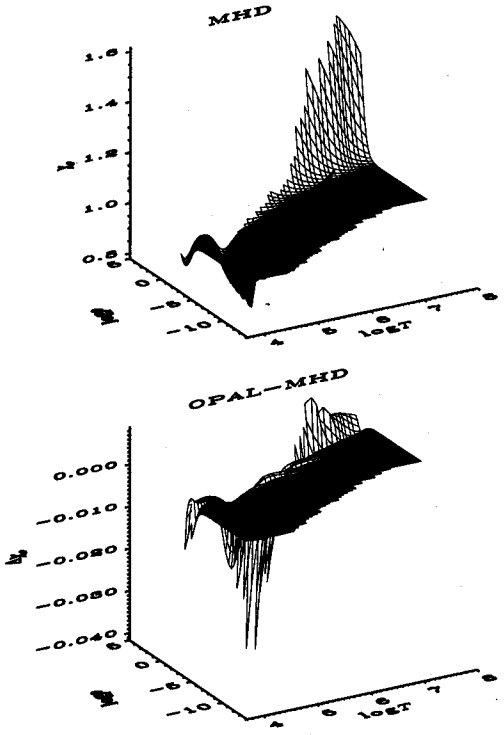

Fig. 10.— χ_ϱ, the logarithmic pressure derivative at constant temperature, for the full mixture in the upper panel, and its differences (OPAL minus MHD) in the lower panel.

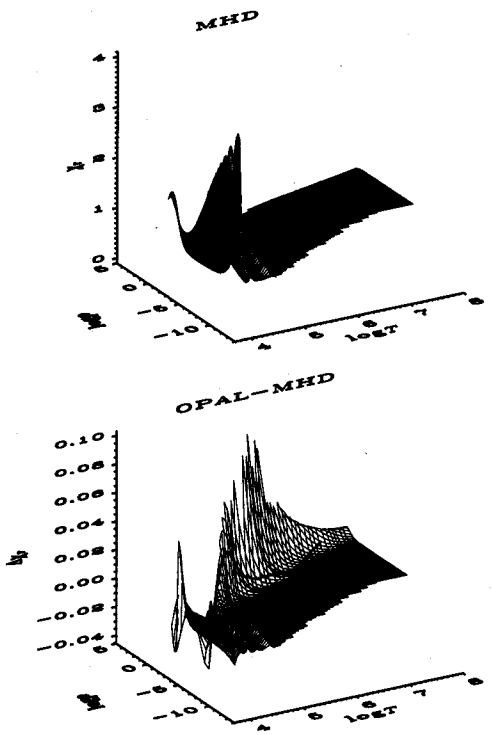

Fig. 11.— χ_T, the logarithmic pressure derivative with respect to temperature, for the full mixture in the upper panel, and its differences (OPAL minus MHD) in the lower panel.

relation (Heisenberg 1927) and Pauli's exclusion principle (Pauli 1925): Due to the former, electron wavefunctions are extended, but due to the latter, the wavefunctions of two close electrons with same spin cannot overlap. This results in the combined wavefunction either having a bulge or a node at the mid-point between the two electrons, giving rise to two different kinds of contributions to the Coulomb interactions. In the fully ionized, weak degeneracy limit, the first-order e-e exchange pressure (DeWitt 1961, 1969) is negative and proportional to ϱ^2/T. Analyzing the differences in solar solar case, we actually find in Sect. 4, that those powers of ϱ and T are the ones best describing the differences above $T \simeq 2 \times 10^6$ K

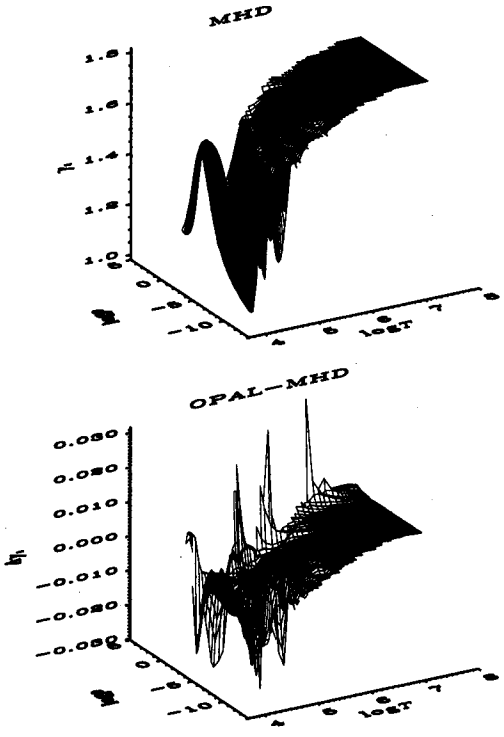

Fig. 12.— The adiabatic logarithmic pressure derivative, γ_1, for the six element mixture in the upper panel, and its differences (OPAL minus MHD) in the lower panel.

4. Comparisons in the Sun

To study the EOS under solar conditions, we have evaluated the MHD and OPAL EOS on a $\varrho - T$ track that corresponds to the Sun using the respective interpolation routines. Obviously, this is a simplified comparison, not of evolutionary models of the Sun, but merely of the equations of state for fixed solar-like circumstances. As demonstrated elsewhere, such a simplified procedure is well justified (See *e.g.* Christensen-Dalsgaard et al. 1988).

We use the three chemical mixtures from Table 1, bearing in mind that Mix 3 has about twice solar metallicity. In contrast to the comparisons of the previous section, we now include radiative contributions. This will of course not change the differences of thermodynamic quantities, since both formalism use the well-known additive radiative contributions (Cox & Guili 1968).

In all the figures of this section, we notice that the MHD and the OPAL EOS differs very little at temperatures below 20 000 K and above 10^6 K, but they differ significantly in between. And though the differences are small, above 20 000 K they look intriguingly systematic.

The wiggles in the differences, most noticeable in the region between log$T$=4-4.5, are almost certainly due to the interpolation schemes. They become quite dominant in the γ_1 difference. As mentioned in Sect. 3, the tabular resolution of the OPAL tables for Mix 2 and 3 is about three times better than that of the corresponding MHD tables. This means that most of the interpolation wiggles comes from MHD. The exception is the pure hydrogen case (Mix 1), where the tables have the same (low) resolution and the respective interpolation errors are of the same order.

4.1. Pure hydrogen

If we take a look at the absolute pressure in Fig. 13 a), we notice a bend at log$T = 6.4$. This marks the bottom of the convection zone. Inside the convection zone, that is below log$T = 6.4$, there is adiabatic stratification of pressure and temperature, *i.e.*

$$\nabla_{\rm ad} = \left(\frac{\partial \log T}{\partial \log P}\right)_{\rm ad} = \frac{\gamma_1 - \chi_\varrho}{\gamma_1 \chi_T}. \qquad (16)$$

When the gas is nearly fully ionized, essentially $\nabla_{\rm ad} = 2/5$, evidenced as the straight-line part of

the curve in Fig. 13 a). In the ionization zones (the outer $0.02R_\odot$), ∇_{ad} is lowered to about 0.11 at $\log T \simeq 4.1$, again clearly evidenced as a depression in the pressure curve. ∇_{ad} comes back to 2/5 at $\log T \simeq 3.76$, but this happens at the top of the convection zone where there is a downward bend to a radiative stratification. The *depth* of the convection zone is about $0.285R_\odot$, and just slightly higher, at a depth of $0.25R_\odot$, hydrogen finally gets fully ionized (fewer than 1 in 10^5 are still neutral), at a temperature of $\log T = 6.3$. For comparison, hydrogen is 99.88% ionized in the middle of the convection zone at $\log T = 6$. So, although it is reasonable to say that the hydrogen ionization zone is confined to the outermost 2% of the Sun, one should also bear in mind the long tail of unionized hydrogen that is extending almost to the bottom of the convection zone. This tail has an especially large effect on the opacity, since in the visual and UV only bound states can add opacity to the constant "background opacity" from electron scattering.

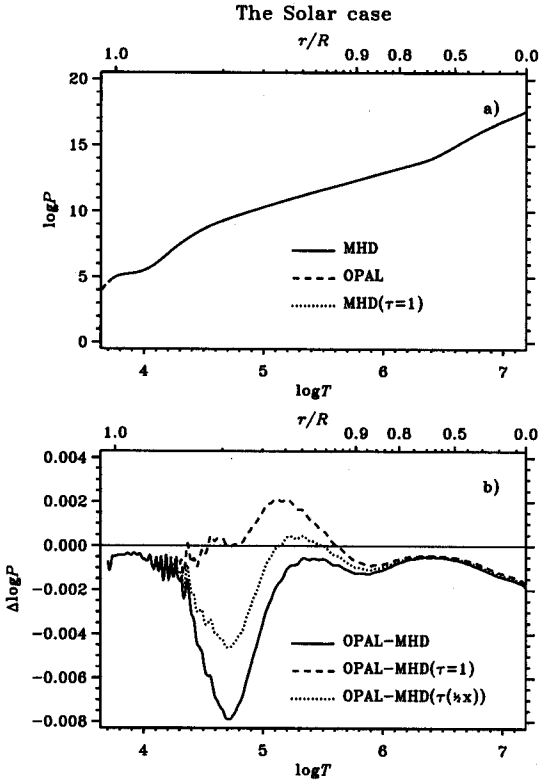

Fig. 13.— The logarithmic pressure along a solar ϱ, T-track for pure hydrogen. The upper panel shows the absolute values of the MHD (solid line) and the OPAL (dashed line) pressure. We also plot the MHD pressure, using $\tau = 1$ to show the effect of omitting this correction (*cf.* Sect. 2.2.2). These three pressures are indistinguishable unless we look at the lower plot, showing the difference OPAL minus MHD. Here we show, apart from the normal MHD, also the version with $\tau = 1$, which seems closer to OPAL, and a version where we have halved the argument of τ.

In the upper plot of Fig. 14 we can actually see the differences between the absolute values of χ_ϱ. It is evident that OPAL has a much smoother and broader ionization zone than the somewhat bumpy MHD. Turning off the τ-correction (dashed lines), almost centers MHD on OPAL, but the bumps re-

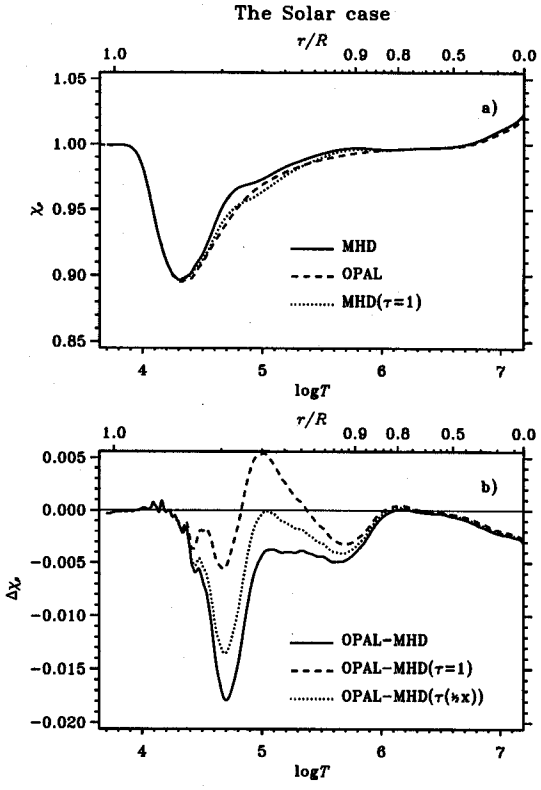

Fig. 14.— The logarithmic pressure derivative with respect to density, χ_ϱ, along the solar track for pure hydrogen. **a)** the absolute value, **b)** the difference (OPAL minus MHD).

main the same. These bumps were also noticed by Nayfonov & Däppen (1998) and their analysis showed that in the region where $\log T = 4.2$–5.2 the bumps are caused by excited states in hydrogen. In this part of the Sun, hydrogen is 30% increasing to 97.8% ionized, so even a small amount of neutral hydrogen can have a significant effect on the EOS.

At $\log T \gtrsim 6.5$ we see how degeneracy sets in, increasing χ_ϱ towards it's fully degenerate value of 5/3. In the lower plot, we notice that degeneracy is accompanied by an increase in the differences. This could be attributed to the MHD EOS not including electron-electron exchange effects, as pointed out in Sect. 3.3.

The behavior of χ_T (Fig. 15) confirms the picture obtained from Fig. 14, that is, MHD ionizing faster and being more bumpy than OPAL. However, since the dynamic range of χ_T is much larger than that of χ_ϱ, the bumps, which have still about the same size as those of χ_ϱ, are now being dwarfed by the much larger ionization peak in χ_T. Comparing the differences shown in the lower plots, we notice that the overall differences are about twice as large as for χ_ϱ, but the ionization peak in the respective upper plots is about 10 times larger for χ_T than for χ_ϱ. We also notice that in χ_T, as a likely result of the higher dynamic range, the interpolation-wiggles at $\log T \lesssim 4.6$, are much more prominent than in χ_ϱ.

We can also distinguish MHD from OPAL in the absolute values of γ_1 (Fig. 16 a)), although they are much closer than in the χ's of Fig. 14 and 15. This is confirmed in the differences shown

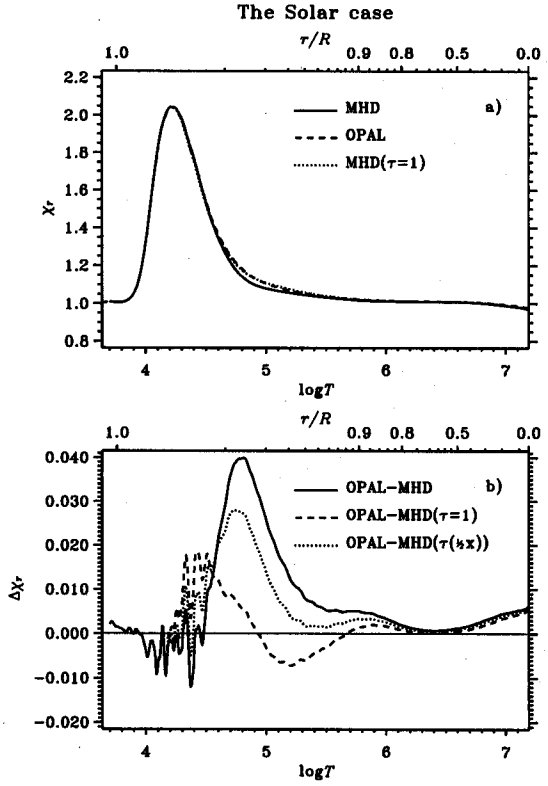

Fig. 15.— The logarithmic pressure derivative with respect to temperature, χ_T, along the solar track for pure hydrogen. **a)** the absolute value, **b)** the difference (OPAL minus MHD).

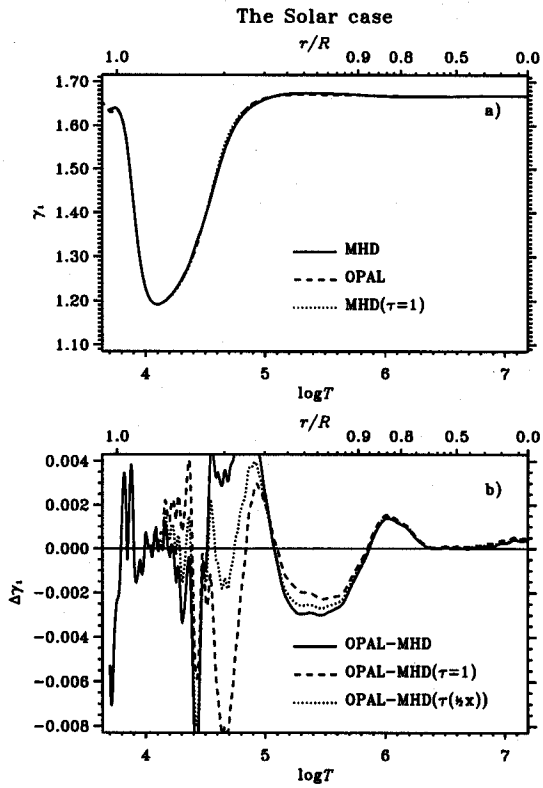

Fig. 16.— The adiabatic logarithmic pressure derivative, γ_1, along the solar track for pure hydrogen. **a)** the absolute value, **b)** the difference (OPAL minus MHD).

in panel b), which are overall smaller by an order of magnitude compared to the P-, χ_ϱ- and χ_T-differences. In contrast to our experience with P, χ_ϱ and χ_T, here diminishing the τ-correction in MHD (dashed and dotted lines) does not lead to any better agreement with OPAL. This is again convincing evidence that γ_1 is a very efficient filter for high-R effects. The differences that we see are therefore due to the physics of ionization, except at low temperatures, where interpolation errors seem to dominate.

4.2. Hydrogen and helium mixture

The effect of helium is very hard to see in the reduced pressure shown in Fig. 17 a), and in the shape of the differences in Fig. 17 b). However, a comparison with the pure hydrogen case (Fig. 13), allows us none the less to see a few changes to the differences in the lower panels; The peak around $\log T = 4.7$ gets considerable smaller by adding helium, except for the $\tau = 1$ case, where the difference actually increases in this region. Also, the differences outside the high-R region decrease by adding helium, independently of the choice of τ.

In general, adding helium does not alter the shape of the differences in P, χ_ϱ or χ_T, and the changes due to composition are only manifest by a change of the amplitude of the peak around $\log T = 4.7$. This is surely due to the fact that most of the ionization in the Sun takes place in the high-R region, so that the first-order high-R differences due to the ionizations themselves simply dwarf the second-order effects due to detailed partition functions, among other. The solar track does follow the ionization zones to some de-

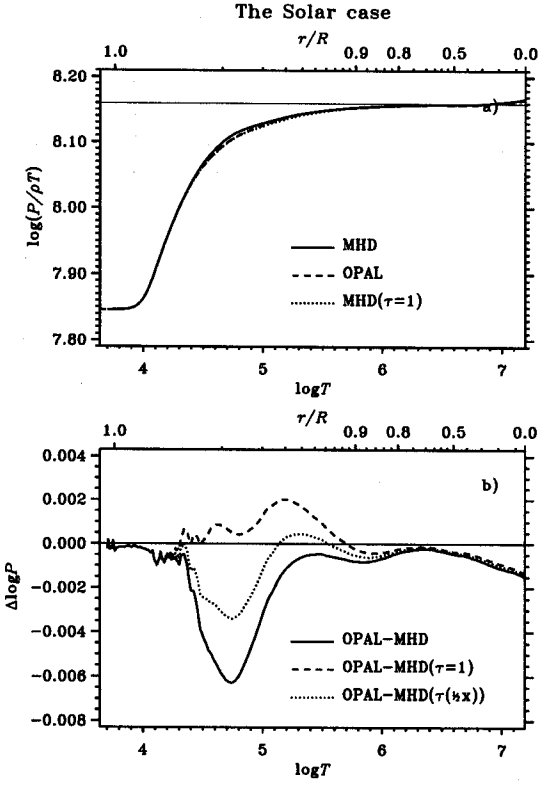

Fig. 17.— The reduced pressure in the H-He-mixture along the solar track. **a)** the absolute value, **b)** the difference (OPAL minus MHD). The thin horizontal line in panel a), indicates the fully ionized, perfect gas pressure.

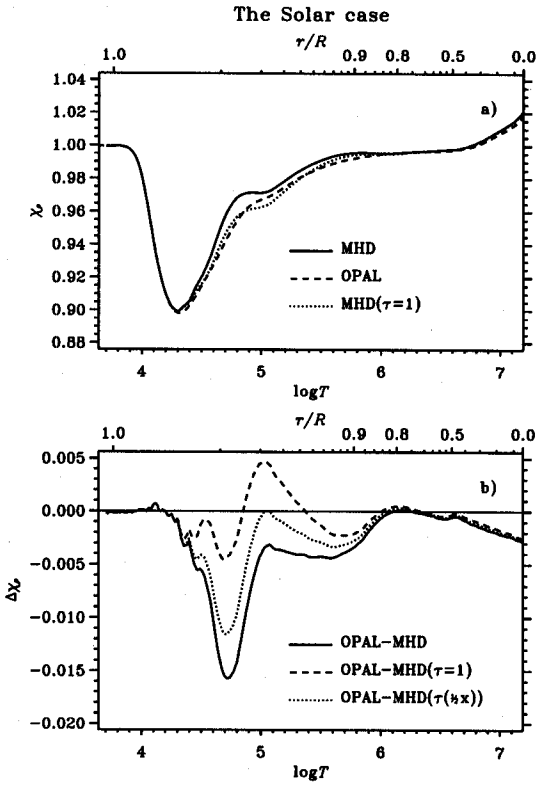

Fig. 18.— χ_ϱ for the H-He-mixture along the solar track. **a)** the absolute value, **b)** the difference (OPAL minus MHD).

gree, and only enters the hydrogen ionization zone "head on". With the solar track curving along the hydrogen ionization zone in this way the ionization features will be smoothed out over a much larger temperature interval than if we had examined an iso-chore. This smoothing leads to more blending of ionization zones from various elements, hampering analysis. The shape, merging and smoothing of the ionization features is best seen in Figs. 9–11.

This behavior is clearly illustrated in, *e.g.*, χ_ϱ (Fig. 18 a), where we observe a rather sharp onset of ionization followed by a much slower transition to full ionization. The second ionization of helium appears as part of the bump around $\log T = 5$. The bump is somewhat more pronounced than in the pure hydrogen case. A more careful comparison with the pure hydrogen case (Fig. 14) reveals the first ionization zone of helium as a slight extension of the hydrogen peak, on the side towards higher temperatures. Helium gets almost fully ionized at $\log T = 6.0$, where 1.77% is singly ionized and 98.23% doubly ionized. It only ionizes slowly further at higher temperature, until at $\log T = 6.75$ it suddenly becomes fully ionized. This happens at a depth of $0.63 R_\odot$, at the edge of the hydrogen burning core. At $\log T = 6.5$, just slightly above the temperature where hydrogen gets fully ionized, there is finally no more neutral helium left.

For χ_T (Fig. 19 panel a), the bump at $\log T \simeq 5$ is a clear sign of the helium added, as opposed to the similar but more entangled bump in χ_ϱ (*cf.* Fig. 14 and 18). The second He ionization zone is very distinct in γ_1 (Fig. 20 a), and the first ionization zone is manifested by a widening of the hydrogen ionization zone towards the high-T side. The differences (panel b) are just as entangled as for pure hydrogen (Fig. 16) but with lower amplitude. On the descending part, just above $\log T = 5$, there

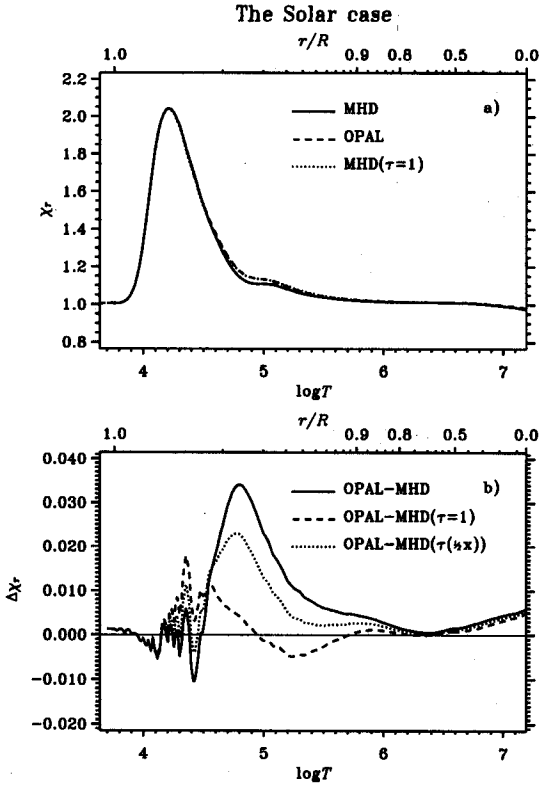

Fig. 19.— χ_T for the solar track and the H-He-mixture. **a)** the absolute value, **b)** the difference (OPAL minus MHD).

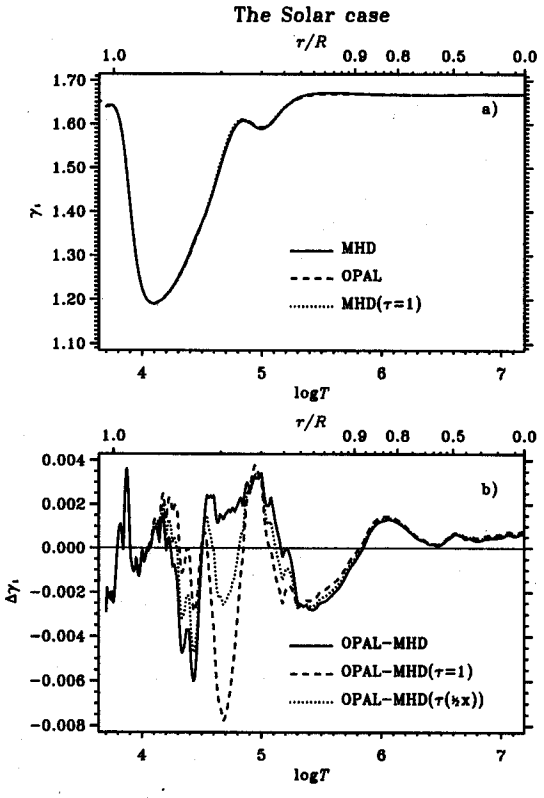

Fig. 20.— γ_1 for the solar track and the H-He-mixture. **a)** the absolute value, **b)** the difference (OPAL minus MHD).

are some large interpolation errors, caused by the change to the coarser grid. We also notice a peculiar bump at $\log T = 6.6$

Looking at the various difference plots in this section, we see a correlation between a high amplitude in the differences and a high R-value, a property we already inferred from the solar track (Fig. 1). The minimum in R is found at the base of the convection zone, where we also find a local minimum in the magnitude of the differences between the EOS. The location of this local minimum coincide for all four thermodynamic quantities. This confirms our suspicion that at least some of the discrepancy stems from τ. The reason for this conjecture is that the differences between MHD EOS with different τ almost vanishes in this region, whereas they increase in the same way as the MHD-OPAL differences grow for intermediate temperatures.

At high temperatures, above a minimum occurring at $\log T \simeq 6.4$, the MHD-OPAL differences grow, but the differences between the three τ versions themselves remain small. On the solar track, $\log R = -1.8$ at the minimum of the MHD-OPAL difference, and it only rises slightly to -1.4 at $\log T = 6.8$ where the solar track bends to follow more or less an iso-R line. The constant R value is attained around $\log T = 6.15$. The differences between the τ-versions are indeed the same in both of these regions (this is best seen in the pressure differences *e.g.* Fig. 17), which explains why the three curves with different τ follow each other so closely at high temperatures. The MHD-OPAL difference in this region can therefore not be explained by the τ-correction. It also turns out that

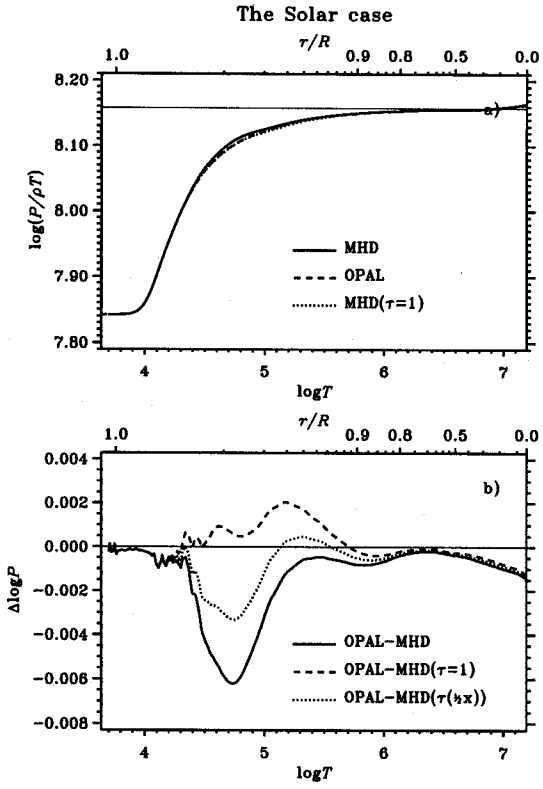

Fig. 21.— Reduced pressure for the solar track and the 6-element mixture. **a)** the absolute value, **b)** the difference (OPAL minus MHD). The thin horizontal line in panel a), indicates the fully ionized, perfect gas pressure.

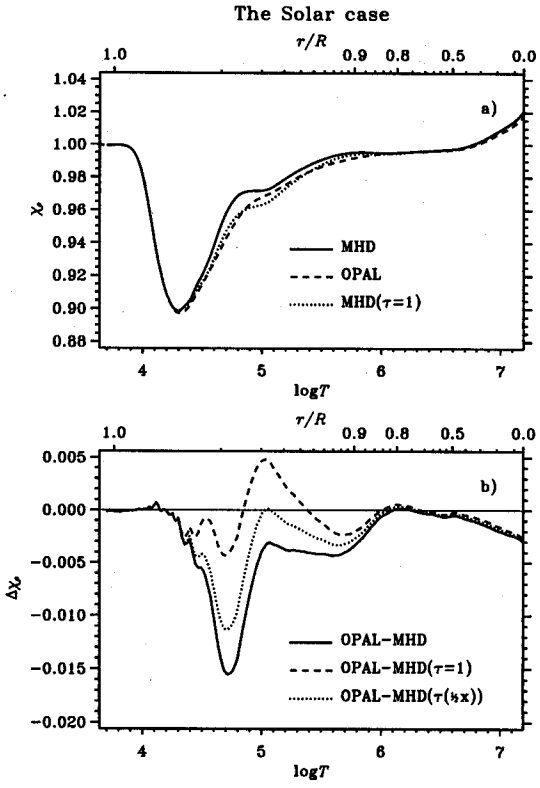

Fig. 22.— The logarithmic pressure derivative with respect to density χ_ϱ for the 6-element mixture along the solar track. **a)** the absolute value, **b)** the difference (OPAL minus MHD).

in this region, the differences of the ϱ-T plane are mainly functions of ϱ^2/T^3 instead of R. In Sect. 3.3 we suggested that this dependence might arise from electron exchange effects or maybe from possibly different evaluations of the Fermi-Dirac integrals. However, a third explanation might be based on the quantum diffraction mentioned in Sect. 2.2.3.

4.3. H,He,C,N,O and Ne mixture

Adding C, N, O and Ne to the H-Ne mixture has two main effects: first, it displaces 4% He (*cf.* Tab. 1), thereby diminishing the helium features, and second it leads to a slight decrease in the high-R OPAL-MHD differences due to the increased mean charge [see Eq. (9)]. Only in γ_1 (Fig. 24), can the heavy elements be observed directly. Comparing with the H-He case (Fig. 20), and going from low to high temperatures, we first notice a slight diminishment of the feature associated with the first ionization zone of helium due to the 4% decrease of the helium content. This weakening of the He^+ feature is counteracted by the second ionization zone of carbon (24.38 eV), as well as that of the less abundant Ne (21.56 eV) and N^+ (29.60 eV). The feature of the second ionization zone of helium is also diminished, but counteracted by the third ionization zone of oxygen O^{++} (54.93 eV), the most abundant heavy element. C^{++}, C^{3+}, N^{++} and Ne^{++} adds further ionization in this temperature region. Continuing towards higher temperatures we notice a slight straightening of the "knee" around $\log T \simeq 5.3$, due to the intermediate ionization stages of C, N and Ne with ionization potentials between 47 eV and 240 eV. Finally,

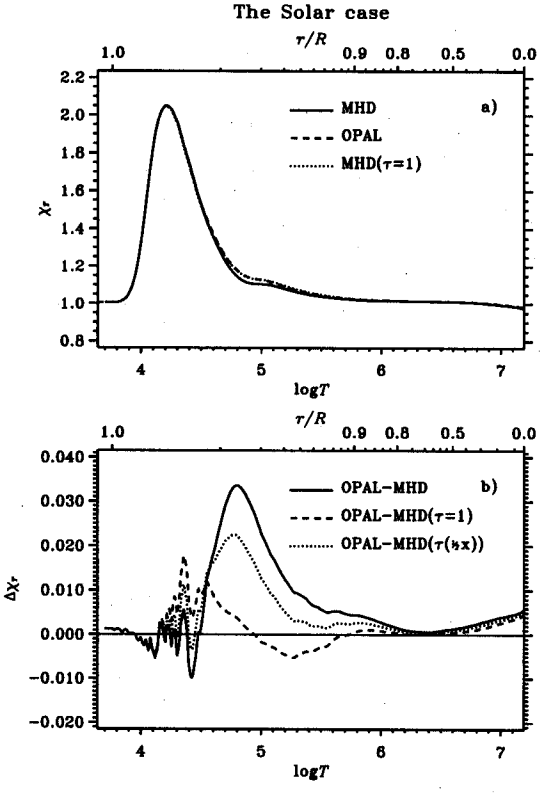

Fig. 23.— The logarithmic pressure derivative with respect to temperature χ_T for the 6-element mixture along the solar track. **a)** the absolute value, **b)** the difference (OPAL minus MHD).

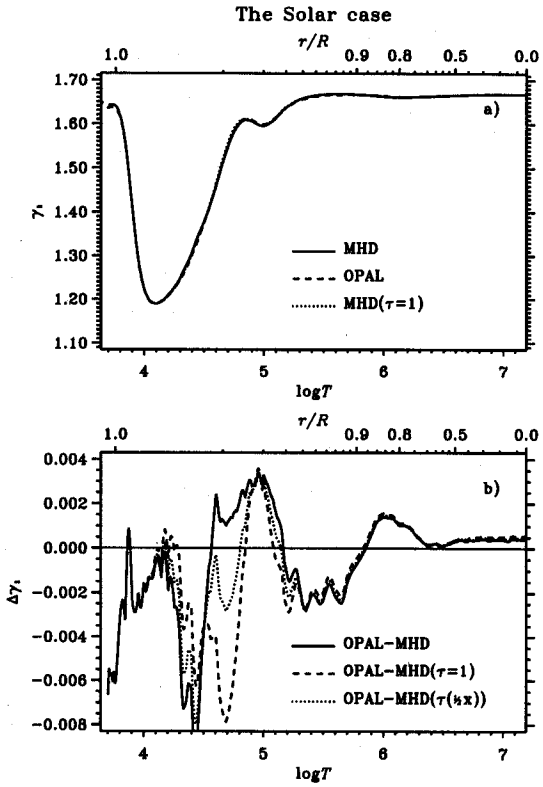

Fig. 24.— The adiabatic logarithmic pressure derivative, γ_1, for the six-element mixture along the solar track. **a)** the absolute value, **b)** the difference (OPAL minus MHD).

at $\log T \simeq 6.2$, we find a broad dip supplied by the two uppermost ionization stages of C,N,O and Ne, having ionization energies in the range between 400 eV and 1 360 eV.

The only quantity in which the introduction of heavy elements is manifested directly is γ_1, which is an important key variable in helioseismology (since it is closely related to adiabatic sound speed $c^2 = \gamma_1 p/\varrho$). The promise of these features is that the presence of heavy elements is well marked in γ_1. Actually, this marking is so distinct (Gong et al. 2001a), that in future solar and stellar applications of the MHD and OPAL equations of state it might be worth to include more heavy elements The influence due to our small quantity of heavy elements is about three times larger than the difference between OPAL and MHD, though we hasten to add that our heavy element abundance of $Z = 4\%$ is chosen too high in order to exhibit the effects more clearly; they would of course decrease with a more solar metallicity around $Z = 2\%$.

We have not discussed radiation pressure yet, merely because of the lack of controversy about it. However, it is worth a few notes. The ratio between radiation pressure and gas pressure is constant along iso-R lines the two being equal around $\log R \simeq -4.5$. The largest radiation effects therefore occur at $\log T = 6.4$ where there is also the smallest discrepancy between OPAL and MHD. The relative size of the effect of radiation is: $0.0007, -0.001, 0.003, -0.002$ for $\log P$, χ_ϱ, χ_T and γ_1, respectively.

5. Discrepancies due to differentiation

A closer inspection of the derivatives in the perfect gas region reveals some discrepancies which are likely due to the numerical differentiation performed in the OPAL EOS. This is most noticeable in γ_1, where the OPAL-MHD differences in the perfect gas region are as large as 0.03%, which admittedly is small indeed. Helioseismology will, however, soon be dealing with such precision. This difference most probably comes from problems in the numerical calculation of an adiabatic change as performed in OPAL (note that MHD uses essentially analytical expressions for γ_1, χ_ϱ and χ_T Since an adiabatic change is not rectangular in the $T - \varrho$ plane, such an interpretation is consistent with the fact that the differences in the derivatives with respect to ϱ and T (χ_ϱ and χ_T, respectively) are about one order of magnitude smaller. This also means, that in the ionization zones where pressure and entropy are non-linear functions of ϱ and T, this differentiation noise must be much larger. On the other hand, the differences between OPAL and MHD are still at least an order of magnitude larger than this differentiation noise. We hope, however, that future improvements will make OPAL and MHD converge to within that level of the actual EOS, requiring higher numerical standards.

The differences in χ_ϱ and χ_T have a tendency to follow iso-R tracks, while the differences in γ_1 follow isotherms. These two behaviors are still unexplained. In Fig. 25, the differences following isotherms are pretty clear, but the iso-R differences are also visible, well below the rising mountain at high R-values.

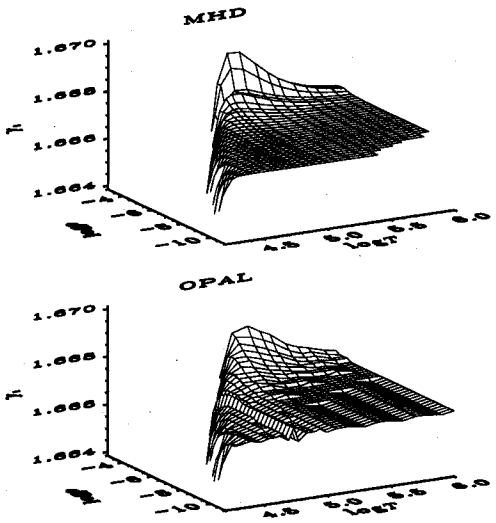

Fig. 25.— This is a zoom-in on the fully ionized, perfect gas region of a pure hydrogen plasma (*cf.* Fig. 4), where $\gamma_1 = 5/3$. The upper panel shows the results for the MHD EOS which uses analytical expressions for all first- and second-order derivatives. The lower panel shows the same for the OPAL EOS, where derivatives are calculated numerically on a grid that are much denser in ϱ and T though, than in the tables published.

6. Conclusion

The present comparison of the two MHD and OPAL EOS has revealed the reasons of several differences between these equations of state. They can be summarized as follows (in order of importance):

a) We find the largest differences at high densities and low temperatures, or more precisely, at high R-values. From Sect. 2.2.1 and Eq. (9) we know that this property is indicative of differences in the treatment of plasma interactions. Comparing the peaks of the differences in *e.g.* pressure (See Figs. 13, 17 and 21), we obtain Mix-1-to-Mix-2 ratios of 0.797, and Mix-1-to-Mix-3 ratios of 0.788, which agrees very well with Eq. (9), and thus further substantiates our interpretation. These differences are lowered dramatically when we put $\tau = 1$ in MHD, indicating that it is worthwhile to abolish τ and reconsider how to get rid of the short-range divergence in the plasma-potential (See Sect. 2.2.3).

b) In the high-temperature-high-density corner of the tables we observe how degeneracy sets in. Along with degeneracy, we also notice how some specific differences are growing. This effect could be due to quantum diffraction or exchange effects, both included in OPAL but not in MHD. Quantum diffraction is the effect of the quantum mechanical smearing out of, primarily, the electron due to it's wave nature. The exchange effect is a modification of the quantum diffraction arising from the anti-symmetric nature of two-particle wavefunctions of fermions.

c) Differences also appear in the ionization zones, and a great deal of them can be attributed to the τ correction, but not all of it. The causes for the rest of these differences are not easily identified. They might be due to the basic differences between the physical- and the chemical approach to the plasma. The treatment of bound state energies and wave functions might have an effect in this region. These are highly accurate in MHD but calculated in the isolated particle approximation, whereas they are approximate (fitted to ground-state energies), but varying with the plasma environment in OPAL. We have also tried experimenting with the assumed critical field strength used in MHD for the disruption of a bound state [Eq. (4.24) of Hummer & Mihalas (1988)]. However, this intervention had only a very small effect. Earlier investigations by Iglesias & Rogers (1995) indicated that a change in the micro-field distribution might have a greater effect, and that highly excited states are more populated in the OPAL EOS, although the OPAL EOS ionizes the plasma more readily than MHD (Nayfonov & Däppen 1998).

d) The evaluation of thermodynamic differentials is done numerically in OPAL but analytically in MHD. For the quantities we have examined here, the difference becomes most apparent in γ_1. In the trivial perfect gas region of the $\varrho - T$ plane, OPAL is rugged on a 0.03% scale (see Sect. 5), as opposed to the smooth MHD. These 0.03% may sound negligible, but helioseismology is approaching that level. In ionization zones, the discrepancies due to differentiation are most likely larger. On the other hand, physical differences between the two EOS are still at least an order of magnitude larger.

For helioseismic studies of the equation of state it is a very nice property of the Sun that high-R conditions are found exclusively in the convection zone, where the stratification is essentially adiabatic, and therefore virtually decoupled from radiation and the uncertainty in the opacity (Christensen-Dalsgaard & Däppen 1992). As opacity calculations are still subject to errors of 5-10%, we stress the importance of the fact that opacity effects do not contaminate the structure of the convection zone. This means that the solar convection zone is a perfect laboratory for investigations of the most controversial parts of the EOS.

The difference between γ_1 from and EOS and that of the Sun can be inferred from helioseismology, and that with an accuracy that by far exceeds the discrepancy between the two of the best present EOS for stellar structure calculations (Christensen-Dalsgaard et al. 1988). The pursuit for a better EOS is therefore not at all

academic, and we can improve both solar models and atomic physics in the process (Basu & Christensen-Dalsgaard 1997).

We thank Jørgen Christensen–Dalsgaard for supplying us with a copy of his solar model S Christensen-Dalsgaard et al. (1996). R. T. acknowledges support from NASA grants NAG 5 9563 and 5-12450, and NSF grant 0205500. W. D. acknowledges support from the grants AST-9618549 and AST-9987391 of the National Science Foundation. In addition, W.D. and R.T were supported in part by the Danish National Research Foundation through its establishment of the Theoretical Astrophysics Center.

REFERENCES

Alastuey, A., Cornu, F., Perez, A. 1994, Phys. Rev. E 49, 1077

Alastuey, A., Cornu, F., Perez, A. 1995, Phys. Rev. E 51, 1725

Alastuey, A., Perez, A. 1992, Europhys. Lett. 20, 19

Basu, S., Christensen-Dalsgaard, J. 1997, A&A 322, L5

Basu, S., Däppen, W., Nayfonov, A. 1999, ApJ 518, 985

Berrington, K. A. (ed.) 1997, "The opacity project", Vol. 2. Institute of Physics Publishing

Berthomieu, G., Cooper, A., Gough, D., Osaki, Y., Provost, J., Rocca, A. 1980. In: H. A. Hill, H. A. and W. Dziembowski, W. (eds.), "Nonradial and nonlinear stellar pulsation", Vol. 125 of Lecture Notes in Physics, IAU Coll. 38, Springer Verlag, Berlin, 307

Cauble, R., Perry, T. S., Bach, D. R., Budil, K. S., Hammel, B. A., Collins, G. W., Gold, D. M., Dunn, J., Celliers, P., Silva, L. B. D., Foord, M. E., Wallace, R. J., Stewart, R. E., , Woolsey, N. C. 1998, Phys. Rev. Letters 80, 1248

Christensen-Dalsgaard, J. 1991. In: D. O. Gough, D. O. and J. Toomre, J. (eds.), "Challenges to theories of the structure of moderate-mass stars", Vol. 388 of Lecture Notes in Physics, IAU Coll. 38, Springer Verlag, Berlin, 11

Christensen-Dalsgaard, J., Däppen, W. 1992, A&AR 4(3), 267

Christensen-Dalsgaard, J., Däppen, W., Ajukov, S. V., Anderson, E. R., Antia, H. M., Basu, S., Baturin, V. A., Berthomieu, G., Chaboyer, B., Chitre, S. M., Cox, A. N., Demarque, P., Donatowicz, J., Dziembowski, W. A., Gabriel, M., Gough, D. O., Guenther, D. B., Guzik, J. A., Harvey, J. W., Hill, F., Houdek, G., Iglesias, C. A., Kosovichev, A. G., Leibacher, J. W., Proffitt, P. M. C. R., Provost, J., Reiter, J., Rhodes Jr., E. J., Rogers, F. J., Roxburgh, I. W., Thompson, M. J., Ulrich, R. K. 1996, Science 272(5266), 1286

Christensen-Dalsgaard, J., Däppen, W., Lebreton, Y. 1988, Nature 336, 634

Cox, J. P., Guili, R. T. 1968, "Physical principles", Vol. 1 of Principles of Stellar Structure. Gordon and Breach, Science Publishers

Däppen, W. 1992, Rev. Mex. Astron. Astrofis. 23, 141

Däppen, W. 1996, Bull. Astr. Soc. India 24, 151

Däppen, W., Anderson, L., Mihalas, D. 1987, ApJ 319, 195

Däppen, W., Lebreton, Y., Rogers, F. 1990, Solar Physics 128, 35

Däppen, W., Mihalas, D., Hummer, D. G., Mihalas, B. W. 1988, ApJ 332, 261

Debye, P., Hückel, E. 1923, Physic. Zeit. 24(9), 185

DeWitt, H. E. 1961, J. Nucl. Energy, Part C: Plasma Phys. 2, 27

DeWitt, H. E. 1969. In: S. Kamar, S. (ed.), "Low luminosity stars", Gordon and Breach, New York, 211

Di Mauro, M. P., Christensen-Dalsgaard, J., Rabello-Soares, M. C., Basu, S. 2002, A&A 384, 666

Ebeling, W., Förster, A., Fortov, V. E., Gryaznov, V. K., Polishchuk, Y. A. 1991, "Thermodynamic properties of hot dense plasmas". Teubner, Stuttgart, Germany

Ebeling, W., Kraeft, W., Kremp, D. 1976, "Theory of bound states and ionization equilibrium in plasmas and solids". Akademie Verlag, Berlin, DDR

Eggleton, P. P., Faulkner, J., Flannery, B. P. 1973, A&A 23, 325

Elliot, J. R., Kosovichev, A. G. 1998. In: S. Korzennik, S. (ed.), "Structure and dynamics of the interior of the sun and sun-like stars", SOHO 6/GONG 98 Workshop, 453 (in press)

Fowler, R., Guggenheim, E. A. 1956, "Statistical thermodynamics". Cambridge University Press

Gong, Z., Däppen, W., Nayfonov, A. 2001a, ApJ 563, 419

Gong, Z., Däppen, W., Zejda, L. 2001b, ApJ 546, 1178

Graboske, H. C., Harwood, D. J., Rogers, F. J. 1969, Physical Review 186(1), 210

Heisenberg, W. 1927, Forsch. und Fortschr. 3(11), 83

Huebner, W. F. 1986, "Physics of the sun", Vol. 1, 33. D. Reidel Publishing Co., Dordrecht

Hummer, D. G., Mihalas, D. 1988, ApJ 331, 794

Iglesias, C. A., Rogers, F. J. 1991, ApJ 371, L73

Iglesias, C. A., Rogers, F. J. 1995, ApJ 443, 460

Iglesias, C. A., Rogers, F. J. 1995, ApJ 443, 460

Iglesias, C. A., Rogers, F. J. 1996, ApJ 464, 943

Iglesias, C. A., Rogers, F. J., Wilson, B. G. 1987, ApJL 322, L45

Iglesias, C. A., Rogers, F. J., Wilson, B. G. 1992, ApJ 397, 717

Kippenhahn, R., Weigert, A. 1992, "Stellar structure and evolution". Springer Verlag. Chp. 18.4

Kraeft, W., Kremp, D., Ebeling, W., Röpke, G. 1986, "Quantum statistics of charged particle systems". Plenum, New York

Mihalas, D., Däppen, W., Hummer, D. G. 1988, ApJ 331, 815

Nayfonov, A., Däppen, W. 1998, ApJ 499, 489

Nayfonov, A., Däppen, W., Hummer, D. G., Mihalas, D. 1999, ApJ 526, 451

Pauli, W. 1925, Zeits. f. Physik 31, 765

Rogers, F. 1981a, Phys. Rev. A 23(3), 1008

Rogers, F. 1994. In: G. Chabrier, G. and E. Schatzman, E. (eds.), "The equation of state in astrophysics", IAU Coll. 147, Cambridge University Press, 16

Rogers, F. J. 1977, Phys. Lett. 61A, 358

Rogers, F. J. 1981b, Phys. Rev. A 24, 1531

Rogers, F. J. 1986, ApJ 310, 723

Rogers, F. J., Iglesias, C. A. 1992, ApJS 79, 507

Rogers, F. J., Nayfonov, A. 2002, ApJ (submitted)

Rogers, F. J., Swenson, F. J., Iglesias, C. A. 1996, ApJ 456, 902

Saumon, D., Chabrier, G. 1989. In: G. Wegner, G. (ed.), "White dwarfs", IAU Coll. 114, Springer Verlag, Berlin, 300

Saumon, D., Chabrier, G., Horn, H. M. V. 1995, ApJS 99, 713

Seaton, M. 1987, J. Phys. B 20, 6363

Seaton, M. J. (ed.) 1995, "The opacity project", Vol. 1. Institute of Physics Publishing

Seaton, M. J., Zeippen, C. J., Tully, J. A., Pradhan, A. K., Mendoza, C., Hibbert, A., Berrington, K. A. 1992, Rev. Mex. Astron. Astrofis. 23, 19

Shibahashi, H., Noels, A., Gabriel, M. 1983, A&A 123, 283

Shibahashi, H., Noels, A., Gabriel, M. 1984, Mem. Soc. Astron. Ital. 55, 163

Ulrich, R. 1982, ApJ 258, 404

Ulrich, R., Rhodes, E. 1983, ApJ 265, 551

This 2-column preprint was prepared with the AAS LaTeX macros

3.2 Pressure Ionization in the MHD Equation of State

We, Trampedach & Däppen (2004b), elucidate the behavior and importance of an often quoted and questioned term in the Mihalas-Hummer-Däppen (MHD) equation of state (EOS), the so-called Ψ-term, which provides pressure ionization of neutral plasmas in the high density/low temperature region.

3.2.1 Introduction

In stellar evolution computations, and in particular in the case of stars more massive than the Sun, it is generally sufficient to use a simple equation of state. The plasma of the stellar interior is treated as a mixture of perfect gases of all species (atoms, ions, nuclei and electrons), and the Saha equation is solved to yield the degrees of ionization or molecular formation. In the case of low mass stars however, non ideal effects, such as Coulomb interactions become important.

For such stars, the most useful equations of state, as far as their smooth realization and versatility are concerned, are (i) the so-called Mihalas-Hummer-Däppen (MHD) equation of state (Hummer & Mihalas 1988; Mihalas et al. 1988; Däppen et al. 1988), and (ii) the OPAL equation of state, the major alternative approach developed at Livermore (Rogers 1986; Rogers et al. 1996, and references therein). A brief description of these two equations of state is given in Sect. 3.2.3.

Although the MHD equation of state was originally designed to provide the level populations for opacity calculations of stellar *envelopes*, the associated *ther-*

modynamic quantities of MHD can none the less be reliably used even for cores of low-mass stars (Chabrier & Baraffe 1997a). Low-mass stars harbor the most extreme plasma-conditions, the gas being far from ideal, due to the high densities and low temperatures. The Coulomb interaction between particles becomes more important, as does the destruction of the more fragile excited states. This latter phenomenon will eventually lead to pressure ionization, which in the MHD equation of state is achieved through an occupation probability formalism for bound species, as detailed in Sect. 3.2.2. The neutral-neutral interactions employed are, however, not strong enough to pressure-ionize a plasma consisting of mostly neutral particles (low temperature), and approximate higher-order terms are therefore included through the Ψ-term, addressed in the present paper.

Since the MHD equation of state otherwise includes processes important for low-mass stars and envelopes of white dwarfs (W. Stolzmann, *private communication*), *e.g.*, Coulomb pressure and electron degeneracy, the question of the impact and validity of the Ψ-term is more than academic.

3.2.2 Pressure ionization in MHD

In this paper we examine pressure ionization in the MHD equation of state. As described in Hummer & Mihalas (1988), the formalism incorporates perturbations from the fluctuating fields from the charged particles, and a first-order approximation to the hard-sphere interactions from neutral particles. It turned out that the approximative neutral-neutral interaction *alone* is too weak to overcome the steeply increasing

energy of the free, degenerate electrons, and thereby cause pressure ionization. This is hardly surprising.

If, however, there are just a few charged particles present, the fluctuating micro-fields takes over and pressure ionize without any problems.

The pressure dissociation of hydrogen molecules avoids this problem all together, as no electrons are released, and pressure dissociation does occur in the MHD equation of state without any extra help.

The hard-sphere model, or excluded volume model, has the free energy

$$F_5 = -k_{\rm B}T \sum_i N_i \ln \left[1 - \left(\frac{2\pi}{3V} \right) \sum_j N_j (R_i + R_j)^3 \right] , \tag{38}$$

where both sums are extended over all states of all species of particles. Expanding the logarithm in

$$\xi_i = \left(\frac{4\pi}{3V} \right) \sum_j N_j (R_i + R_j)^3 , \tag{39}$$

the free energy can be written

$$F_5 = k_{\rm B}T \sum_i N_i \left(\frac{1}{2}\xi + \frac{1}{8}\xi^2 + \frac{1}{24}\xi^3 + \ldots \right) \tag{40}$$

The first order term is already included in the expression for the occupation probabilities, w_{is}, apart from a factor of two.

As shown by Fermi (1924), occupation probabilities, w_i, as used in the MHD

formulation for partition functions, Z,

$$Z = \sum_i w_i e^{-E_i/k_B T} \ , \tag{41}$$

are accompanied by a term in the Helmholtz free energy

$$F_w = f - \sum_i n_i \left(\partial f/\partial n_i\right) \ , \tag{42}$$

where $\ln w_i \equiv -\left(\partial f/\partial n_i\right)/k_B T$. In the case that the non-ideal term, f, is linear in the occupation numbers $\{n_i\}$, the F_w-term vanish identically, making it independent of the state of excitation. By confining effects that depend on the population of excited levels, to such linear terms in the occupation probabilities, the equation of state is reduced to a $M \times M$- instead of a $N \times N$-matrix problem, where $M \simeq 170$ is the number of species (atoms, ions and molecules) and $N \simeq 16\,000$ is the total number of states considered.

The first term in the expansion, Eq. (40), of the hard-sphere free energy therefore result in no extra terms in the free energy.

Retaining the $N \times N$-order of the problem, the second order term can therefore only be included in an approximate way, *e.g.*, assuming that all particles of a given species are in the same state. Using the ground-state, we can therefore write

$$\xi_\nu = \left(\frac{4\pi}{3V}\right) \sum_\mu N_{1\mu} (R_{1\nu} + R_{1\mu})^3 \ , \tag{43}$$

where ν and μ label particle species. The second order term is then of the form

$$\begin{aligned} F' &= -k_{\rm B}T\sum_{\nu} N_\nu(-\alpha\xi_\nu^2) \\ &= -k_{\rm B}T\sum_{\nu} N_\nu \ln\Psi_\nu \ , \quad \ln\Psi_\nu = -\alpha\xi_\nu^2 \ . \end{aligned} \tag{44}$$

This artificial term was introduced to allow computation of numerically consistent results for very cold and dense plasmas, just to allow tabulation of thermodynamical quantities in rectangular temperature-density grids, with less regard to physical accuracy in this difficult region of limited astrophysical interest.

It is a legitimate concern that the presence of the artificial pressure ionization mechanism, the so-called Ψ-term might contaminate the results for less extreme conditions relevant for stellar interiors. We show with this paper that this is not the case, and that the pressure ionization in the MHD equation of state, for stellar conditions, is caused by the decreasing occupation probabilities with increasing density. The Ψ-term only affects the high density low temperature corner of the (ϱ, T)-plane, and was merely introduced to ensure numerical stability and convergence in this region.

Before presenting the results of our study, which is based on a systematic switching on and off of the Ψ term, for the convenience of the reader, we give the specifications of the MHD equation state and its relation to alternative formalisms.

3.2.3 A brief review of the MHD equation of state

Historically, the MHD equation of state was developed as part of the international "Opacity Project" (OP, see Seaton 1987; Seaton et al. 1992). It was realized in the so-

called *chemical picture*, where plasma interactions are treated through modifications of atomic states, *i.e.* the quantum mechanical problem is solved before statistical mechanics is applied. It is based on the so-called free-energy minimization method. This method uses approximate statistical mechanical models (for example the non-relativistic electron gas, Debye-Hückel theory for ionic species, hard-sphere atoms to simulate pressure ionization via configurational terms, quantum mechanical models of atoms in perturbed fields, etc). From these models a macroscopic free energy is constructed as a function of temperature T, volume V, and the concentrations $N_1, \ldots, N_M$ of the M components of the plasma. The free energy is minimized subject to the stoichiometric constraint. The solution of this minimum problem then gives both the equilibrium concentrations and, if inserted in the free energy and its derivatives, the equation of state and the thermodynamic quantities.

More specifically, in the chemical picture, perturbed atoms must be introduced on a more-or-less *ad-hoc* basis to avoid the familiar divergence of internal partition functions (see *e.g.*, Ebeling et al. 1976). In other words, the approximation of unperturbed atoms precludes the application of standard statistical mechanics, *i.e.* the attribution of a Boltzmann-factor to each atomic state. The conventional remedy of the chemical picture against this is a modification of the atomic states, *e.g.* by cutting off the highly excited states in function of density and temperature of the plasma. Such cut-offs, however, have in general dire consequences due to the discrete nature of the atomic spectrum, *i.e.* jumps in the number of excited states (and thus in the partition functions and in the free energy) despite smoothly varying external parameters (temperature and density). However, the occupation probability formal-

ism employed by the MHD equation of state avoids these jumps and delivers very smooth thermodynamic quantities. Specifically, the essence of the MHD equation of state is the Hummer & Mihalas (1988) occupation probability formalism, which describes the reduced availability of bound systems when immersed in a plasma. Perturbations by charged and neutral particles are taken into account. The neutral contribution is evaluated in a first-order approximation to hard-sphere interactions, which is good for stars in which most of the ionization in the interior is achieved by temperature. For colder objects (brown dwarfs, giant planets), higher-order excluded-volume effects become important (Saumon & Chabrier 1991; Saumon et al. 1995). In the common domain of application of the Saumon et al. (1995) and MHD equations of state, Chabrier & Baraffe (1997a) showed that the two developments yield very similar results.

Despite undeniable advantages of the physical picture, the chemical picture approach leads to smoother thermodynamic quantities, because they can be written as analytical (albeit complicated) expressions of temperature, density and particle abundances. In contrast, the physical picture is normally realized with the unwieldy chemical potential as independent variable, from which density and number abundance follow as dependent quantities. The physical-picture approach involves therefore a numerical inversion before the thermodynamic quantities can be expressed in their "natural" variables temperature, density and particle numbers. This increases computing time greatly, and that is the reason why so far only a limited number of OPAL tables have been produced, and then only suitable for stars more massive than $\sim 0.8\,M_{\odot}$.

3.2.4 Examination of the influence of the Ψ term

To quantify how much the Ψ-term affects the MHD EOS, we have calculated two tables, including and neglecting Ψ, respectively, and plotted the pressure difference between the two in Fig. 4.

The occupation probabilities in the MHD EOS are very dependent on the presence of charged particles in order to ionize. At sufficiently large densities and low

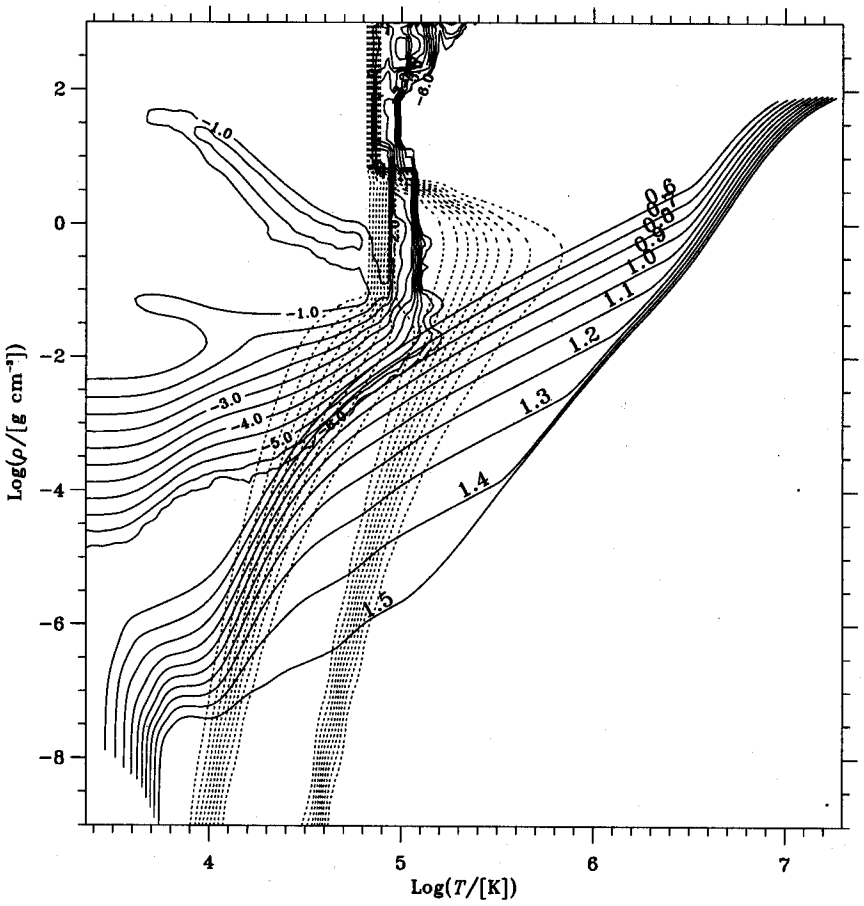

Fig. 4. This figure shows contours of the difference in pressure between including and ignoring the Ψ-term, in the sense $\log_{10}|\Delta \log_{10} P|$. We have also plotted tracks of stellar structure, for stars in the mass range 0.6-1.5$M_{\odot}$, as indicated above each track. The dotted contour lines mark the hydrogen and second helium ionization zones respectively, with contour lines in steps of 10%.

temperatures there are no such seed charges from the temperature ionization, and

the pressure ionization due to the occupation probabilities can not occur. Even the slightest amounts of metals, *i.e.* some elements with very low ionization potentials, will supply seed-charges in a larger region than a pure hydrogen plasma. Introducing helium will of course work in the opposite direction due to the high ionization potential. To investigate the most extreme case (fewest seed charges) of astrophysical relevance, we therefore performed the calculations for a hydrogen/helium mixture with $Y = 20\%$ (by mass), but no metals.

From Fig. 4 we see that the pressure in the $0.6\,M_\odot$ model is altered by less than 0.003% by introducing Ψ. It looks as if the stellar tracks follows the iso-difference curves for quite a stretch, but examining the stellar models more closely, we find that the large temperature and density gradients in the outer parts of the star, causes this region to be very thin. For the $0.6\,M_\odot$ model, it is centered around a relative radius of $r/R = 0.987$, and already at 0.975 and 0.995, this difference has fallen by an order of magnitude from its maximum.

The extent of the affected region is indeed thin, and the location is below the super-adiabatic uppermost part of the convection zone and far from the photospheric transition zone. These regions are even more shallow, but nevertheless very important for the stellar structure, as they act as upper boundary conditions for the whole star (Trampedach et al. 2004d). The thin region affected by Ψ does not have a corresponding importance and the implications for the star as a whole are insignificant.

The inner 94% of the star (by radius—99.8% by mass), on the other hand, pressure ionizes perfectly by means of the occupation probabilities without any intervention by the Ψ-term.

3.2.5 Conclusion

As can be seen from Fig. 4, the Ψ-term barely affects any stellar models. By extrapolating the stellar model-tracks in the figure a bit, we conclude that the pressure in a $0.5\,M_\odot$ star is at most changed by 0.01% and for a $0.4\,M_\odot$ star, about 0.03%. As explained in Sect. 3.2.4 the largest change even occurs in a very thin layer, in a region of the star which responds linearely to such changes, *i.e.*, hardly affects the remainder of the star.

We conclude that the Ψ-term is not a cause for serious concern regarding the validity of the MHD EOS for stars down to masses of $0.4\,M_\odot$.

3.3 MHD 2000

Prompted by helioseismic analysis and detailed comparisons with the principal competing equation of state (EOS) project, we, Trampedach & Däppen (2004a), here present an updated MHD (EOS) including a number of new phenomena, as well as the previously published updates of improved electric micro-field distributions and relativistically degenerate electrons. The main new features include higher order density terms in the Coulomb interactions, quantum effects including relativistic effects and a new formulation of interactions that involve particles with zero met-charge, abandoning the hard-sphere interactions. These changes expand the region of validity towards higher temperatures and densities, easily encompassing normal stellar cores. We also include di- and poly-atomic molecules (in addition to the already present H_2- and H_2^+-molecules), in order to include stellar atmosphere in the domain of the MHD EOS.

3.3.1 Introduction

The equation of state (EOS) is an integral part of most astrophysical analysis, having the two rôles of supplying the thermodynamic state of the plasma, and of serving as a foundation for opacity calculations by providing ionization- and dissociation-balances and detailed populations of all electronic states.

In the late 1980s two very successful EOS emerged, both being parts of efforts to improve on the opacities available to the astrophysical community: The Mihalas-Hummer-Däppen EOS (Hummer & Mihalas 1988; Mihalas et al. 1988; Däppen et al.

1988) as part of the international Opacity Project (OP) which is nicely summarized in the two volumes by Seaton (1995) and Berrington (1997), and the OPAL EOS (Rogers 1986; Rogers et al. 1996), pursued at the Lawrence Livermore National Laboratory, being the foundation for the OPAL opacities (Iglesias et al. 1987; Iglesias et al. 1992; Iglesias & Rogers 1991; Iglesias & Rogers 1996; Rogers & Iglesias 1992a).

From detailed comparisons between these two, fundamentally different, approaches to the EOS (Däppen et al. 1990; Trampedach et al. 2004c) and comparisons with helioseismic inversions (Basu et al. 1999), a number of problems with the MHD EOS have been identified. In particular, experiments with the partition functions (Gong et al. 2001a), suggested that the fluctuating micro-fields in the MHD EOS were too efficient at destroying highly excited states. This result was backed by direct comparison between a number of formulations for the micro-field distributions, including those used in the MHD and the OPAL EOS (Iglesias & Rogers 1995). Recent work by Badnell & Seaton (2003) indicate, however, that the equivalent level-populations in the OPAL EOS are improbably high at high densities and temperatures. Nayfonov et al. (1999) introduced an improved treatment of micro-field distributions, dubbed Q-MHD, which also includes the effects of electrons screening the charges of the ions (and *vice verca*). We have implemented our own version of Q-MHD, as detailed in Sect. 3.3.6.

Helioseismic investigations by Elliot & Kosovichev (1998) showed a clear sign of the Solar radiative interior not only being slightly degenerate, but also slightly relativistic. We therefore include the work by Gong et al. (2001b) on relativistically degenerate electrons, as well as a number of other relativistic effects in Sect. 3.3.3.

In the Sun, relativistic effects become significant in the radiative zone, increasing towards the center. Another effect of about the same magnitude at the solar center, is the exchange interaction between identical particles, which we include in Sect. 3.3.5.

Trampedach et al. (2004c) recommended to introduce quantum diffraction (see Sect. 3.3.5) and higher order terms in the Coulomb interactions (see Sect. 3.3.5), to improve the agreement between the MHD and the OPAL EOS. Both these effects were included in OPAL, but not in the MHD EOS.

In Sect. 9 we present the contributions from the exchange interactions between identical particles, and derive an expansion for the relativistic exchange integral in terms of the generalized Fermi-Dirac functions.

In the original MHD EOS, perturbations by neutral particles (atoms) was included by means of the hard-sphere model. In order for the problem to remain tractable this term was only treated up to first order in density, and second order terms were included in an approximate way, as discussed by Trampedach & Däppen (2004b). The hard-core interaction model is inherently flawed, as it introduces a divergence for high densities and is undefined for densities higher than the close-packing density of the spheres.

The interactions involved when neutral particles interact, are obviously still caused by the charges of the particles constituting the atoms; In close encounters between atoms, the electronic wave-functions will overlap and the nuclei will therefore no longer be completely screened from each other and net-forces arise. We describe this phenomena by introducing the concept of effective charge in Sect. 3.3.5.

In Sect. 3.3.7 we describe how we introduce molecules (other than H_2 and H_2^+) into the MHD EOS, through parameterized partition functions. Inspired by the original MHD EOS, we derive analytical approximations to the occupation probabilities of molecules, based on the two molecules, H_2 and H_2^+, that are treated in detail.

3.3.2 Chemical Compositions

In the following sections we will plot comparisons between the original and the present updates to the MHD EOS. These comparisons obviously depend on the chemical mixtures used in the calculations, and we therefore introduce the reader to our choices of chemical compositions, before we proceed to the equation of state issues.

To facilitate comparisons with earlier work (*e.g.*, Trampedach et al. 2004c) and with the OPAL EOS, we use a H/He-mixture and a 6-element mixture, as listed in Tab. 1. We list the abundances in logarithmic abundance relative to hydrogen, $[N_i/N_{\rm H}]$, which is normalized to 12. Mix 1 and 2 have helium mass-fractions of $Y = 20\%$ and 16%, respectively, and a hydrogen mass-fraction of $X = 80\%$. In Tab. 1 we also list the ionization potentials for the first ionization stage, χ_1, to indicate the temperatures for which they start to add electrons to the plasma.

The 6-element Mix 2 has a metallicity more than twice that of the Sun, $Z_\odot = 1.8\%$ and a distinctly sub-solar helium abundance, $Y_\odot = 0.245$ (Basu & Antia 1995), exaggerating metallicity effects with respect to most stellar applications. This is of course useful for analyzing the effects of metals on the EOS.

Next, we need to address the issue of the best solar composition, *i.e.*, metal-

Table 1. Chemical mixtures in $[N_i/N_H]$ (see text)

element	Mix 1	Mix 2	GN96	Optimized	χ_1/[eV]
H	12.00000	12.00000	—	—	13.59844
He	10.79902	10.70211	—	—	24.58741
C	—	8.90307	8.55000	8.55884	11.26030
N	—	8.30307	7.97000	7.97000	14.53410
O	—	9.23307	8.87000	8.87000	13.61806
Ne	—	8.72077	8.08000	8.11100	21.56454
Na	—	—	6.32000	6.32895	5.13908
Mg	—	—	7.58000	7.58000	7.64623
Si	—	—	7.56000	7.56000	8.15169
K	—	—	5.13000	5.13000	4.34066
Fe	—	—	7.50000	7.65924	7.87052

mixture, to use for the final table calculations. The computational cost increase drastically with the number of elements and the complexity (atomic number) of the elements considered, but we also want to preserve the characteristics of the full mixture. For the full mixture, we use the compilation by Grevesse et al. (1996) (GN96). As a measure of the characteristics of a particular composition, we use the average charge

$$\langle Z \rangle = \sum_\alpha N_\alpha Z_\alpha / \sum_\alpha N_\alpha \ . \tag{45}$$

where we sum over all ionization stages of all metals. We estimate the population of all ionization-stages of metals along a solar stratification, using simple Saha-equations (Saha 1921), with ground-level statistical-weights for the partition-functions. The approximations here should be immaterial, since we only want an estimate of the locations and the relative strength of ionization features.

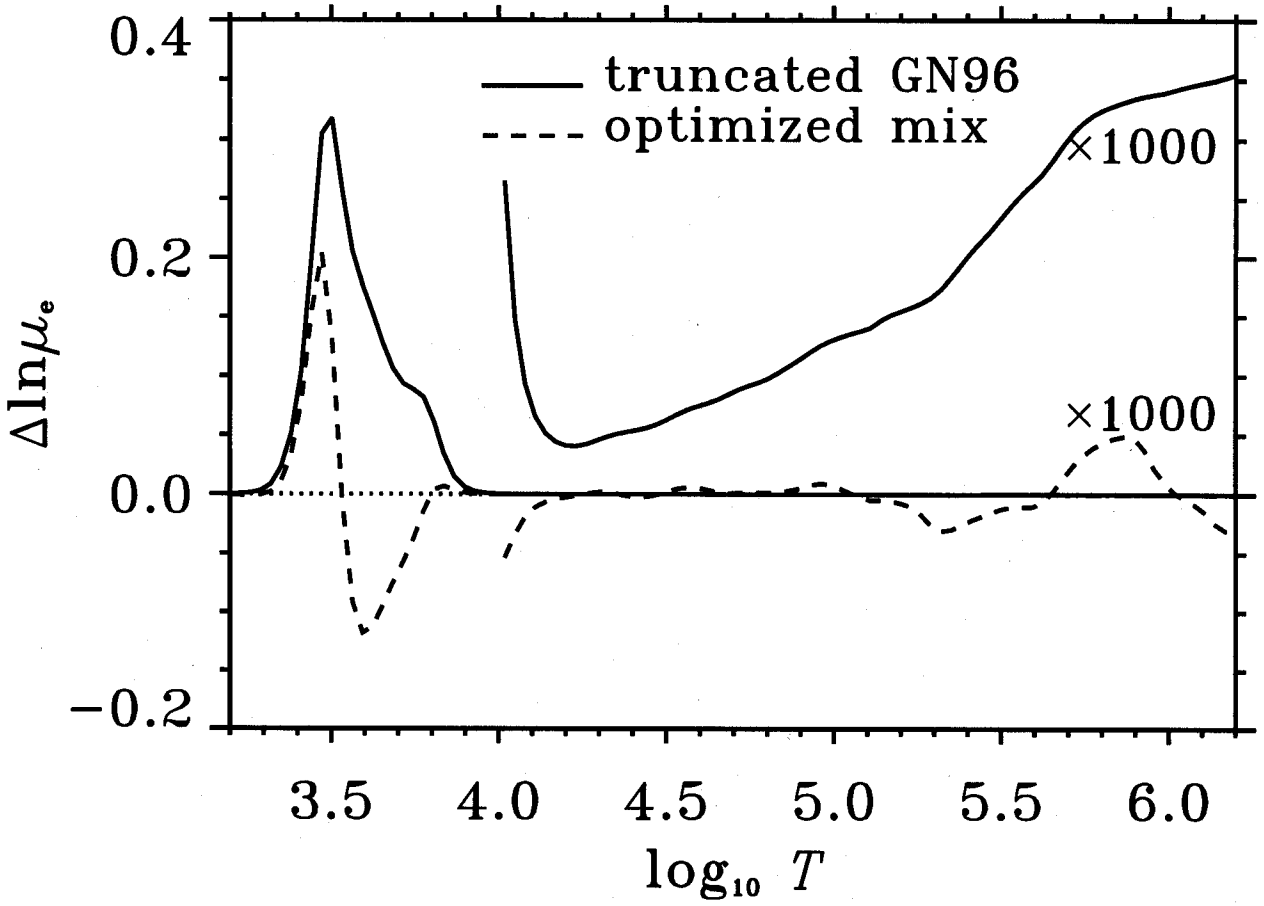

Fig. 5. The relative difference in mean-electron-mass, μ_e, as a function of temperature in a solar stratification. The solid line is for the GN96 mixture truncated from 30 to 11 elements, and the dashed line is the optimized 11 element composition, as listed in Tab. 1.

We truncate the GN96-mixture, and pad the remaining elements to best reproduce the $\langle Z \rangle$ of the full mixture, as well as the average mass of particles in the plasma. The optimization is performed on $\ln\langle Z \rangle$ in order to capture the details of ionization in the parts of stellar atmospheres where hydrogen is still only a minor electron donor.

We find that a good compromise between speed and precision can be struck with a 11-element mixture, comprised of the elements as listed in Tab. 1. The column labeled GN96 is the GN96-mixture truncated to 11 elements, and the last column

is the optimized version. The optimized mixture has a RMS-deviation from the full GN96-mixture of 3.8% We see that most of the padding has been added to iron, some is added to neon, and the rest is shared between carbon and sodium. Potassium, with its ionization potential of 4.341 eV, the lowest of all elements up to ^{37}Rb which is more than 300 times less abundant, is crucial for reproducing the details at low temperatures. Leaving it out, results in over-all discrepancies of 22% and approaching 100% at low temperatures.

Optimizing just the four metals of Mix 2, results in an over-all RMS-deviation of 45%. Below 6300 K the deviation increases rapidly to 100%, *i.e.*, this mixture supplies none of the electrons donated by the low-ionization-potential elements, like sodium and potassium of the 11 element mixture. As can be seen from Tab. 1, Mix 2 has no elements with ionization potential below 11.26 eV.

In the rest of this paper, we will refer to the optimized nine metal-mixture as the solar (metal) composition.

3.3.3 Relativistic electrons

This section is concerned with the consequences of an appreciable fraction of the electrons having relativistic speeds, *i.e.*, $p_e \gtrsim m_e c$, where the masses of particles are always understood to be rest-masses. We let the treatment of relativistic electrons be dealt with prior to the other EOS improvements of the present paper, as it influences most of these.

Due to their much larger masses, ions only become relativistic at temperatures

exceeding 10^{12} K. These temperatures are four magnitudes higher than considered in the MHD EOS at present, and we can therefore safely ignore them for now.

For an ensemble of particles of species α, we use

$$\beta_\alpha = \frac{k_B T}{m_\alpha c^2} \tag{46}$$

as a measure of the importance of relativistic effects — the ratio of kinetic- to rest-mass-energy. As mentioned above, we are only interested in relativistic electrons, and drop the sub-script to simplify notation; $\beta = \beta_e$. The present section is, however, kept general, and applies to all fermions. Note that there is a lack of concensus in the litterature on the definition of β; sometimes the inverse is used.

There are a number of effects arising from particles having relativistic speeds. First of all, special relativity complicates the relation between momentum, p, and kinetic energy, E, changing the general distribution function

$$f(p,E)\mathrm{d}p = \frac{8\pi}{\pi^3}\frac{p^2\mathrm{d}p}{1+e^{u-\eta}} \tag{47}$$

from $(p^2 = 2mE)$

$$f(p,E)\mathrm{d}u = n_*\frac{u^{1/2}\mathrm{d}u}{1+e^{u-\eta}} \tag{48}$$

to $(p^2 = m^2c^2[(\beta u+1)^2-1])$

$$f(p,E)\mathrm{d}u = n_*\frac{\sqrt{(\beta u+1)^2-1}}{1+e^{u-\eta}}(\beta u+1)\mathrm{d}u\ , \tag{49}$$

where $u = E/k_{\rm B}T$, and the normalization factor is

$$n_* = \frac{4\pi}{h^3}(2mk_{\rm B}T)^{3/2} = \frac{4}{\sqrt{\pi}}\lambda_0^{-3} \quad (50)$$

$$= \frac{8\pi\sqrt{2}}{h^3}m^3c^3\beta^{3/2} \ . \quad (51)$$

The thermal de Broigle wavelength for particles of mass, m, is

$$\lambda_0 = h/\sqrt{2\pi mk_{\rm B}T} \ , \quad (52)$$

and the subscript indicates that the thermal average is evaluated at $\eta = 0$, *i.e.*, using Boltzmann statistics.

The two distribution functions, Eqs. (48) and (49) have inspired the definition of the (non-relativistic) Fermi-Dirac functions

$$F_\nu(\eta) = \int_0^\infty \frac{u^\nu {\rm d}u}{1+e^{u-\eta}} \ , \quad (53)$$

and the generalized Fermi-Dirac functions

$$F_\nu(\eta,\beta) = \int_0^\infty \frac{u^\nu\sqrt{1+\frac{1}{2}\beta u}{\rm d}u}{1+e^{u-\eta}} \quad \text{for} \quad \nu > -1 \ , \quad (54)$$

neither of which have analytical integrals. We solve the generalized Fermi-Dirac functions numerically, as described by Gong et al. (2001), who also lists all derivatives up to order three. For convinience, we will list the two first-order derivatives, as we

will need them in Sect. 3.3.4. The differentiation is straight forward, and gives

$$\frac{\partial F_\nu(\eta,\beta)}{\partial \eta} = \int_0^\infty \frac{u^\nu \sqrt{1+\frac{1}{2}\beta u}}{1+e^{u-\eta}} \frac{\mathrm{d}u}{1+e^{\eta-u}} \tag{55}$$

and

$$\frac{\partial F_\nu(\eta,\beta)}{\partial \beta} = \frac{1}{4}\int_0^\infty \frac{u^\nu \sqrt{1+\frac{1}{2}\beta u}}{1+e^{u-\eta}} \frac{u\,\mathrm{d}u}{1+\frac{1}{2}\beta u} \,. \tag{56}$$

From Eqs. (49) and (54), we see that the number density of relativistically degenerate particles, is

$$n = \int_0^\infty f(p,E)dp \tag{57}$$

$$= n_* \left[F_{1/2}(\eta,\beta) + \beta F_{3/2}(\eta,\beta)\right] \,, \tag{58}$$

which is needed for normalization of ensemble averaged kinetic quantities, as *e.g.* the θ- and Θ-factors discussed below.

The largest effect of the change of distribution function, is a change of the translational free-energy of electrons, F_3. We follow the formulation of Gong et al. (2001b) for F_3 and its derivatives.

The change of distribution function, also means that ensemble averaged momenta and energies will change. This has an effect on *e.g.* the degeneracy factors, θ_e and Θ_e, modifying the electron screening contribution to the Debye-length, Eq. (61), and the ensemble averaged De Broigle wavelength, Eq. (68), respectively. These factors will be treated in detail below.

Yet another effect due to relativistic speeds, is that of *retarded potentials*, ac-

counting for the finite speed of propagation of electric fields. It can be shown (See, *e.g.*, Chapter 8 of Landau & Lifshitz 1989) that the potential produced by a moving charge, is

$$\phi = \frac{e}{R - \dfrac{\boldsymbol{v}\cdot\boldsymbol{R}}{c}} , \tag{59}$$

where $\boldsymbol{R}$ is the vector from the charge, to the point of observation.

3.3.4 The Free Energy of the Coulumb interactions

In the original version of the MHD EOS (Hummer & Mihalas 1988; Mihalas et al. 1988; Däppen et al. 1988), the Coulomb free energy, F_4, is approximated by the Debye-Hückel free energy

$$F_{\rm DH} = -\frac{k_{\rm B}TV}{12\pi}\lambda_{\rm D}^{-3} \tag{60}$$

where $\lambda_{\rm D}$ is the Debye length

$$\lambda_{\rm D}^{-2} = \frac{4\pi e^2}{k_{\rm B}TV}\left[N_{\rm e}\theta_{\rm e} + \sum_{\alpha\neq{\rm e}} N_\alpha \tilde{Z}_\alpha^2\right] . \tag{61}$$

Since most expressions involving $\lambda_{\rm D}$, does so in negative powers, we introduce the inverse screening length, $\kappa_{\rm D} = \lambda_{\rm D}^{-1}$. In the summation in Eq. (61), α runs over all particles with a net charge, except for the electrons, for which we also include effects of degeneracy through the $\theta_{\rm e}$-term.

The non-relativistic (NR) $\theta_{\rm e}$ used in the original version of the MHD-EOS,

$$\theta_{\rm e}^{\rm NR} = F_{-1/2}(\eta)/2F_{1/2}(\eta) , \tag{62}$$

is based on the interaction propagators, G_2, for the electrons (Cooper & DeWitt 1973)

$$\theta_e = \frac{G_2}{N_e} = \frac{8\pi}{h^3}\frac{V}{N_e}\int_0^\infty \frac{p^2 dp}{e^{u-\eta}+1}\frac{1}{1+e^{\eta-u}} , \tag{63}$$

which can be generalized to the relativistic case by using Eq. (49). From Eq. (55) we now recognize the integral as $\partial F_\nu(\eta,\beta)/\partial\eta$, so that

$$\theta_e = \frac{\partial F_{1/2}(\eta,\beta)/\partial\eta + \beta\partial F_{3/2}(\eta,\beta)/\partial\eta}{F_{1/2}(\eta,\beta)+\beta F_{3/2}(\eta,\beta)} , \tag{64}$$

which through the recursion relation, $(\nu+1)F_\nu(\eta) = \partial F_{\nu+1}/\partial\eta$, yields the previous result in the non-relativistic limit. This new expression for θ_e, however, does not account for other relativistic effects in the plasma interactions due to, *e.g.*, the retardation of the potential. For lack of a better theory, we choose to limit ourselves to the relativistic effect on θ_e.

In Fig. 6 we show the θ_e-factor in the non-relativistic limit (solid curve) and for β up to 1.0 in steps of 0.1 (dashed curves). Degeneracy of electrons strongly inhibits them from contributing to the screening of the ions, *i.e.*, since they can hardly change state, because none are available to them, the electrons will act more like a uniform, charged background. Relativistic effects only make the electrons slightly more effecient at screening.

In the following sections, we will present improvements to the Coulomb free energy, based on quantum mechanical effects, higher-order density effects, and *effective charges* to account for extended particles. The final expression for F_4 is summarized

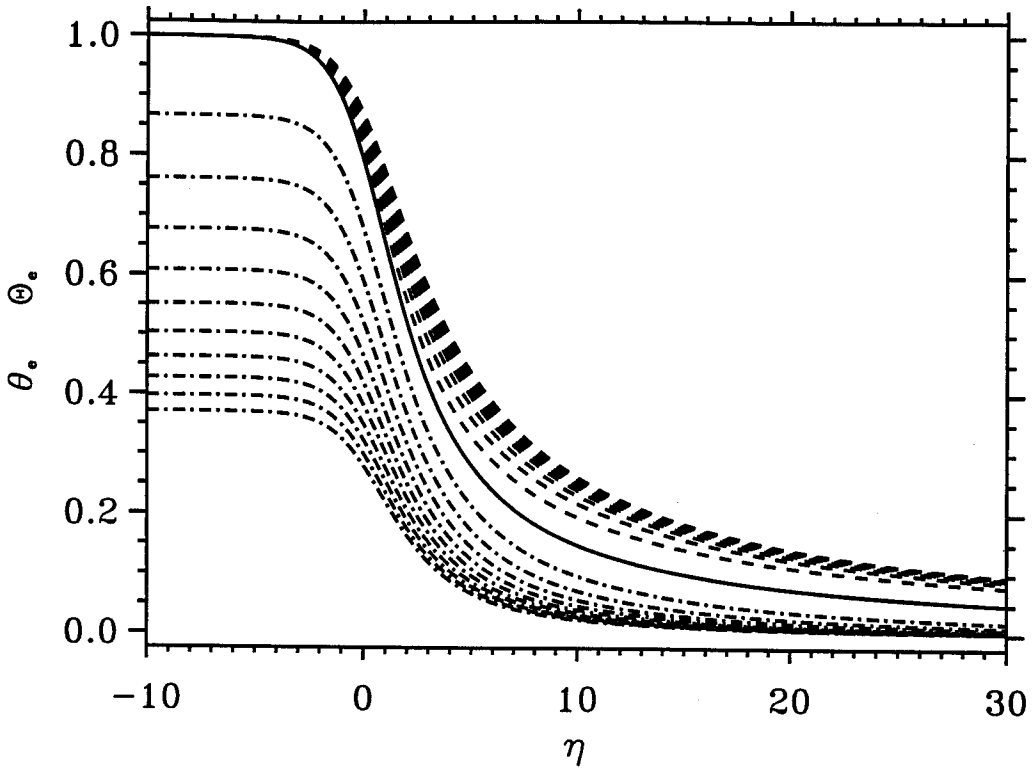

Fig. 6. The two degeneracy factors, θ_e Eq. (64), and Θ_e Eq. (78). The solid line shows the non-relativistic case, for which $\theta_e(\eta, 0) = \Theta_e(\eta, 0)$. The dashed lines displays the relativistic θ_e for β up to 1.0 in steps of 0.1, and the dash-dotted lines shows the same for Θ_e. The behaviour in β is monotonic in both cases.

in Sect. 3.3.5.

3.3.5 Quantum Diffraction

In the original MHD EOS, F_{DH} was multiplied by a correction-factor to account for limits on the distance of closest approach between two particles. This correction factor has since been disputed (Trampedach et al. 2004c), and it was suggested to abandon it for the more physical phenomenon of quantum diffraction.

Quantum diffraction removes the short range divergence of the Coulomb potential, by means of Heisenbergs uncertainty principle. The wave nature of the particles results in finite charge densities at the position of particles, thereby leading to zero

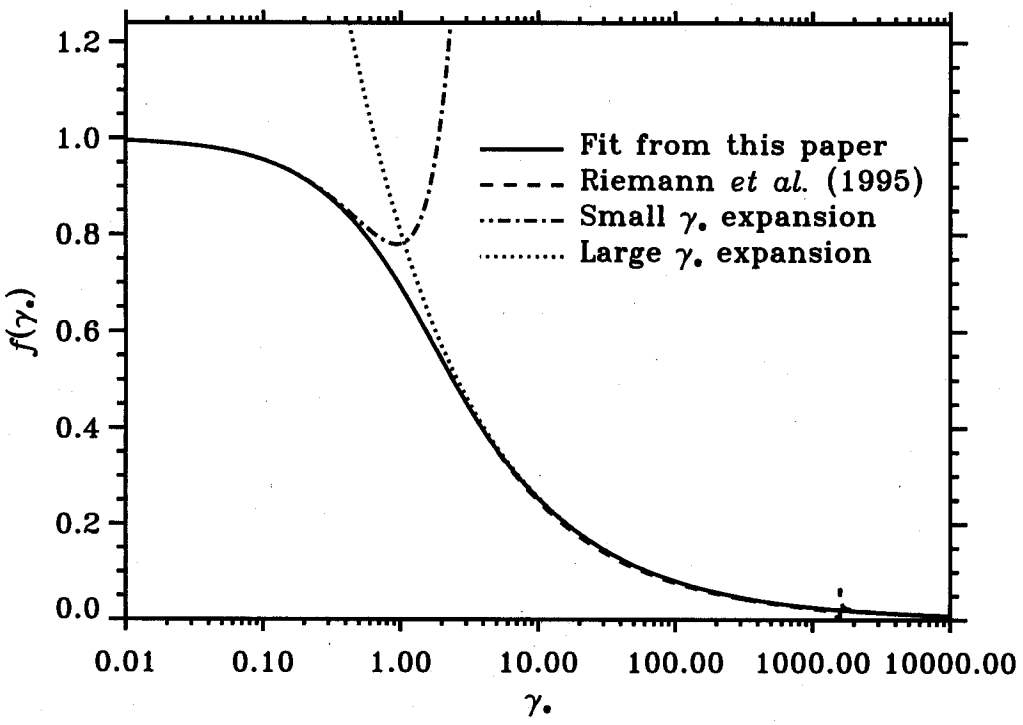

Fig. 7. The quantum diffraction term, as evaluted from Eq. (65) and (66). We compare with the Padé-formula given by Riemann et al. (1995) and with analytical expansions for small and large γ.

potential at $r = 0$. This effect results in a suppresion of the Coulomb interactions at distances comparable to a de Broigle wavelength, which we accomplish with

$$\tau(x) = \sqrt{\frac{1 - e^{-x}}{x}} \, . \tag{65}$$

where

$$x = a\gamma \left[1 + \frac{b}{1 + \frac{3}{5}(a\gamma)^{7/6}} \right] \tag{66}$$

with coeffecients

$$a = 1.5393236 \quad \text{and} \quad b = 0.22047583. \tag{67}$$

As is evident from Fig. 7, this form of τ and x, makes a very good fit to Eq. (10)

of Riemann et al. (1995), but without the singularity at $\gamma \simeq 1570$. From $\gamma \simeq 4$ and up to the singularity, the two fits differ by up till 0.6 %, but our fit is much closer to the large γ-expansion than to Riemann et al.'s fit in this region. We suspect that their fitting coeffecients are merely published with too little precision. The asymptotic behaviour of τ for large, as well as for small γ, is the same as given by Riemann et al. (1995).

The argument, γ, is the center of mass de Broigle wavelength in units of a Debye length. Defining the single particle de Broigle wavelength as $\lambda_\alpha = \hbar/p_\alpha$, we can define the thermally averaged, *relative* or *center-of-mass* de Broigle wavelength between two particles, as

$$\begin{aligned} \lambda_{\alpha\beta}^2 &= \lambda_\alpha^2 + \lambda_\beta^2 = \hbar^2 \left[\langle p_\alpha^{-2} \rangle + \langle p_\beta^{-2} \rangle \right] \\ &= \frac{\hbar^2}{2k_{\rm B}T} \left[\frac{\Theta_\alpha}{m_\alpha} + \frac{\Theta_\beta}{m_\beta} \right] , \end{aligned} \tag{68}$$

where we use

$$\begin{aligned} \Theta_\alpha &= 1 \qquad \text{for } \alpha \neq \mathrm{e} \\ \Theta_{\rm e} &= \langle p^{-2} \rangle / \langle p_{\rm cl}^{-2} \rangle \, . \end{aligned} \tag{69}$$

The general expression for $\langle p^{-2} \rangle$ is

$$\langle p^{-2} \rangle = \frac{\int_0^\infty p^{-2} f(p,E) {\rm d}p}{\int_0^\infty f(p,E) {\rm d}p} \, , \tag{70}$$

where E is the energy of the particle, p its momentum and $f(p, E)$ is its distribution function.

For the general case of relativistic Fermi-Dirac-statistics

$$f(p, E) = \frac{8\pi}{h^3} \frac{p^2}{1 + e^{E-\eta}} , \tag{71}$$

we introduce the dimension-less energy $u = E/kT$, resulting in the relativistic expression for the momentum

$$p = mc\sqrt{(\beta u + 1)^2 - 1} \tag{72}$$

$$\mathrm{d}p = mc \frac{(\beta u + 1)\beta \mathrm{d}u}{\sqrt{(\beta u + 1)^2 - 1}} . \tag{73}$$

Using $\sqrt{(\beta u + 1)^2 - 1} = \sqrt{2\beta u}\sqrt{1 + \beta u/2}$, we can rewrite $\mathrm{d}p$, which is also the main part of the integrand of the numerator of Eq. (70), as

$$\mathrm{d}p = mc\sqrt{\frac{\beta}{2}} \frac{1 + \beta u}{\sqrt{1 + \beta u/2}} \frac{\mathrm{d}u}{\sqrt{u}} . \tag{74}$$

Realizing that this is the β-derivative of the generalized Fermi-Dirac function, Eq. (56, we obtain

$$\frac{\mathrm{d}p}{1 + e^{u-\eta}} = 2mc\sqrt{2\beta} \left[\frac{\partial F_{-3/2}}{\partial \beta} + \beta \frac{\partial F_{-1/2}}{\partial \beta} \right] . \tag{75}$$

For the denominator of Eq. (70), $n(\eta, \beta)$, We similarely obtain

$$\frac{p^2 \mathrm{d}p}{1 + e^{u-\eta}} = \sqrt{2}(mc)^3 \beta^{3/2} \left[F_{1/2} + \beta F_{3/2} \right] . \tag{76}$$

Combining Eqs. (75) and (76), we finally obtain

$$\langle p^{-2} \rangle = \frac{2}{m_e k_B T} \frac{\partial F_{-3/2}/\partial\beta + \beta \partial F_{-1/2}/\partial\beta}{F_{1/2} + \beta F_{3/2}} \,. \tag{77}$$

In the non-relativistic limit the terms in β can be left out. The classical limit results in $\langle p_{\rm cl}^{-2} \rangle = (m_e k_B T)^{-1}$, and consequently

$$\Theta_e = 2 \frac{\partial F_{-3/2}/\partial\beta + \beta \partial F_{-1/2}/\partial\beta}{F_{1/2} + \beta F_{3/2}} \,, \tag{78}$$

which accounts for the degeneracy of electrons, in the thermally averaged De Broigle wavelength. It is trivial to also account for Fermi-Dirac statistics of ions, but because of the mass difference we have chosen to ignore this, as also stated in Eq. (69). The behaviour of Θ_e is shown in Fig. 6. We notice that in the non-relativistic limit, $\theta_e(\eta, 0) = \Theta_e(\eta, 0)$, which can easily be verified by setting $\beta = 0$ in Eq. (56) and compare with the non-relativistic θ_e in Eq. (62).

From Fig. 6 we see that the average de Broigle wavelength of electrons decrease both with increasing η and increasing β. In both cases the momentum-distribution will be peaked towards higher values and hence decrease the average de Broigle wavelength. For $\beta = 1$, quantum-diffraction of protons will be equally important to that of electrons at $\eta_e \simeq 51$. At the $\beta \lesssim 0.017$ explored in the present paper, this does not become a concern, even for an η_e which is orders of magnitudes larger than the value above.

Dividing $\lambda_{\alpha\beta}$ with $\lambda_{\rm D}$, we now get

$$\gamma_{\alpha\beta} = \frac{\hbar}{\lambda_{\rm D}\sqrt{2k_{\rm B}T}}\left[\frac{\Theta_\alpha}{m_\alpha} + \frac{\Theta_\beta}{m_\beta}\right]^{1/2} . \tag{79}$$

In order to incoorporate this one-component plasma (OCP) quantum diffraction term into our multi-component plasma, we need to write out $\kappa_{\rm D}$ in the expression for the Debye-Hückel free energy, Eq. (60), and relate $\tau(\gamma_{\alpha\beta})$ to the pairwise interactions between particles of species α and β. We rewrite F_4 as

$$F_4 = \frac{2\sqrt{\pi}e^3}{3\sqrt{kTV}}g(\Lambda)\sum_\alpha N_\alpha \tilde{Z}_\alpha^2 \sqrt{N_{\rm e}\theta_{\rm e}\tau^2(\gamma_{\alpha{\rm e}}) + \sum_\beta N_\beta \tilde{Z}_\beta^2 \tau^2(\gamma_{\alpha\beta})} , \tag{80}$$

and note that the τ's has to be squared to come out right in the one-component plasma case for which τ was developed. OCP-τ, but I would really appreciate some comments/opinions - RT]

In order to save computing time, we define an average τ, that can be taken outside the summation over elements

$$\bar{\tau} \equiv \frac{\sum_\alpha N_\alpha \tilde{Z}_\alpha^2 \sqrt{N_{\rm e}\theta_{\rm e}\tau^2(\gamma_{\alpha{\rm e}}) + \sum_\beta N_\beta \tilde{Z}_\beta^2 \tau^2(\gamma_{\alpha\beta})}}{\sum_\alpha N_\alpha \tilde{Z}_\alpha^2 \sqrt{N_{\rm e}\theta_{\rm e} + \sum_\beta N_\beta \tilde{Z}_\beta^2}} , \tag{81}$$

where the two sums in the denominator have decoupled again, as in the classical expression for the Debye-Hückel free energy, *i.e.*, Eq. (60).

A very good fit to the above expression can be made from only two contributions

$$\bar{\tau} \simeq N_1\tau(\gamma_1) + (1 - N_1)\tau(\gamma_2) , \tag{82}$$

Table 2. Coefficients, a_{ij}, for Eq. (83).

γ_1/γ_{ee}	0	1	2	3	4	5
0	9.1782e-01	-1.1232e-02	1.7127e-03	-4.2358e-04	6.0588e-05	-2.4894e-06
1	-4.7200e-02	4.3322e-03	-2.6263e-04	8.9617e-05	-1.1236e-05	4.3540e-07
2	1.0418e-02	-8.7279e-04	1.6545e-04	-7.2533e-05	9.7177e-06	-4.1137e-07
3	-1.9114e-03	1.5821e-04	-4.6280e-05	2.2475e-05	-2.9216e-06	1.1581e-07
4	2.1899e-04	-1.2414e-05	4.4749e-06	-2.4821e-06	3.0554e-07	-1.1137e-08
5	-8.6693e-06	2.1068e-07	-1.4091e-07	9.1226e-08	-1.0532e-08	3.4806e-10

where the first contribution is the combined electron-electron and electron-nucleon contributions and the second is the nucleon-nucleon term.

The RMS deviations of the two-component fits are less than 0.25% throughout the compositional X/Y-plane.

The three new parameters, N_1, γ_1/γ_{ee} and γ_2/γ_{ee} can furthermore be fitted to binomials of order 5 in the X/Y-plane, *e.g.*,

$$\left(\frac{\gamma_1}{\gamma_{ee}}\right) = \sum_{ij} a_{ij} X^i Y^j \tag{83}$$

$$\left(\frac{\gamma_2}{\gamma_{ee}}\right) = \sum_{ij} b_{ij} X^i Y^j \tag{84}$$

$$N_1 = \sum_{ij} c_{ij} X^i Y^j \; . \tag{85}$$

We carried out this fitting procedure, using relative metal-abundances from (Grevesse & Noels 1992), and obtained the fitting coefficients listed in tables 2–4.

Using the γ's and N_1's calculated from Eq. (83-c) results in overall RMS devi-

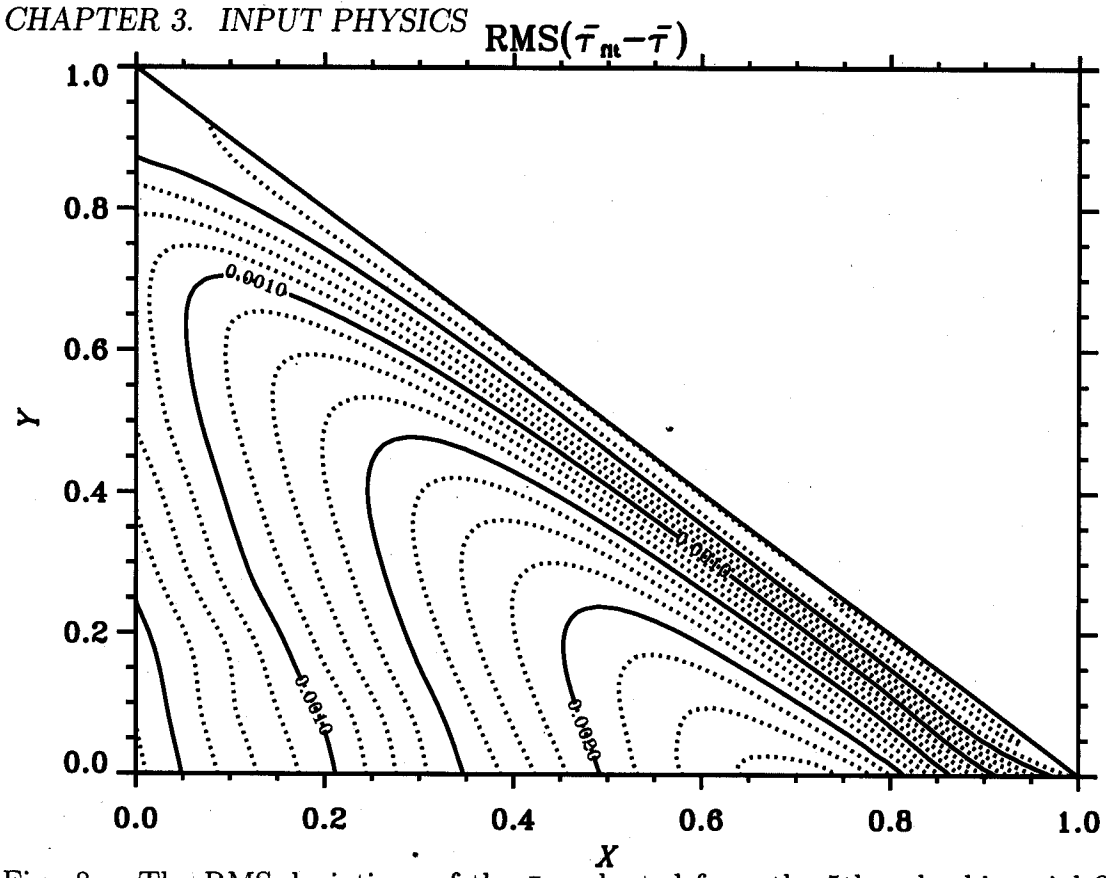

Fig. 8. The RMS-deviations of the $\bar{\tau}$ evaluated from the 5th-order binomial fits, from the exact expression, Eq. (81). The dotted contours are spaced 0.0125% apart and solid contours are 0.05% apart.

Table 3. Coefficients, b_{ij}, for Eq. (84).

γ_2/γ_{ee}	0	1	2	3	4	5
0	5.0211e-03	1.7181e-04	-7.1055e-05	3.0452e-05	-4.5304e-06	2.6472e-07
1	3.5494e-04	-1.1401e-04	2.4850e-05	-6.1806e-06	9.7417e-07	-4.4853e-08
2	-2.3679e-04	1.2572e-04	-1.4812e-05	3.5951e-06	-6.3073e-07	3.2206e-08
3	1.0054e-04	-4.4103e-05	5.8336e-06	-1.5860e-06	2.7030e-07	-1.3612e-08
4	-1.5879e-05	6.2142e-06	-7.6992e-07	2.2073e-07	-3.6915e-08	1.7905e-09
5	9.5203e-07	-2.9630e-07	3.1661e-08	-9.4868e-09	1.5661e-09	-7.3255e-11

ations of less than 0.25% and single $\tau(\gamma_{ee})$ deviations of less than 2%. The largest deviations, as seen in Fig. 8, occur at $\gamma_{ee} \simeq 10^2$ around $X = 0.7$, $Y = 0$ — a rather rarely encountered region of the X-/Y-plane.

Table 4. Coefficients, c_{ij}, for Eq. (85).

N_1	0	1	2	3	4	5
0	1.4213e-01	1.2357e-02	-9.3669e-04	6.5955e-04	-8.8170e-05	5.2504e-06
1	2.7666e-02	7.9054e-04	5.8247e-04	-1.9683e-04	2.8651e-05	-1.5253e-06
2	-1.8022e-05	8.3095e-05	-9.2704e-05	3.3238e-05	-4.1539e-06	1.5133e-07
3	5.6812e-04	-1.6656e-05	6.4215e-06	-3.4200e-06	1.6857e-07	7.5673e-09
4	-6.1064e-05	-2.9772e-07	-2.8268e-07	1.2400e-07	2.4253e-08	-2.7578e-09
5	3.0018e-06	-8.9259e-08	7.8630e-09	1.6651e-09	-1.9424e-09	1.4887e-10

For the moment we have neglected electron-degeneracy effects in the fitting of $\bar{\tau}$, but this can be remedied by using

$$\gamma_1 \rightarrow \frac{\hbar}{\lambda_D\sqrt{2kT}}\sqrt{\frac{\Theta_e}{m_e}}\left(\frac{\gamma_1}{\gamma_{ee}}\right) \tag{86}$$

$$\gamma_2 \rightarrow \frac{\hbar}{\lambda_D\sqrt{2kT}}\sqrt{\frac{1}{m_e}}\left(\frac{\gamma_2}{\gamma_{ee}}\right) , \tag{87}$$

where the γ-ratios are the no-degeneracy fits, that can be fitted with the coefficients from Tab. 2 and 3 respectively.

This whole procedure might seem a bit complicated, but bear in mind that the three parameters, N_1, γ_1/γ_{ee} and γ_2/γ_{ee}, need only be calculated once for each composition, and during the bulk of the calculations, the number of τ-calculations will be reduced by an order of magnitude.

The Free Energy of the

Exchange interaction

The free-energy of the first-order exchange interaction is

$$F_{\rm ex} = \sum_{\alpha} N_{\alpha} \frac{e^2 \tilde{Z}_{\alpha}^2}{\pi n_{\alpha} \lambda_{\alpha 0}^4} [\mathcal{I}(\eta_{\alpha}) + \mathcal{J}(\eta_{\alpha}, \beta_{\alpha})] \tag{88}$$

(Kraeft et al. 1986), where the sum extends over all particle species. The thermal de Broigle wavelength, $\lambda_{\alpha 0}$ [See Eq. (52)], is based on Boltzmann statistics, and all degeneracy effects are included in the exchange integrals, $\mathcal{I}(\eta_{\alpha})$ and $\mathcal{J}(\eta_{\alpha}, \beta_{\alpha})$.

We reformulate Eq. (88) by collecting all η_{α}-dependent terms in one factor, with the relativistic effects included as a Taylor expansion

$$F_{\rm ex} = -\frac{h^2 e^2}{16\pi V k_{\rm B} T} \sum_{\alpha} N_{\alpha}^2 \frac{\tilde{Z}_{\alpha}^2}{m_{\alpha}} J_{\rm ex}(\eta_{\alpha}, \beta_{\alpha}) \ . \tag{89}$$

In this form, it is easier to recognize the dependence on the independent variables, particle-mass and -densities, the latter of which indicates the binary-interaction nature of the exchange-term.

The exchange integral, $J_{\rm ex}$, can be written

$$J_{\rm ex}(\eta, \beta) \equiv \frac{\mathcal{I}(\eta) + \mathcal{J}(\eta, \beta)}{[F_{1/2}(\eta, \beta) + \beta F_{3/2}(\eta, \beta)]^2} \ , \tag{90}$$

where

$$J_{\rm ex}(\eta, 0) = I_{\rm ex}(\eta) = \frac{\mathcal{I}(\eta)}{F_{1/2}(\eta)^2} \tag{91}$$

is the non-relativistic part. DeWitt (1961) derived an expression for $I_{\rm ex}$, amenable to numerical integration

$$I_{\rm ex}(\eta) = \frac{\int_{-\infty}^{\eta} F_{-1/2}^2(\eta')\mathrm{d}\eta'}{F_{1/2}^2(\eta)} \ , \tag{92}$$

which is shown as the solid line in Fig. 9.

We find that $I_{\rm ex}$ can be approximated by the analytical expression

$$I_{\rm ex} \equiv 2\chi \left[C^B + \chi^B\right]^{-1/B} \ , \quad \chi = \frac{1-e^{-A\eta}}{A\eta} \tag{93}$$

using

$$A = 1.0129034 \ , \quad B = 1.5384386 \quad \text{and} \quad C = \frac{4}{9A} \ . \tag{94}$$

This fit agrees with a numerical integration, within 0.75 %. The difference between our fit and the numerical integration, is shown with the dashed line in Fig. 9, on the right-hand-side axis. The fit is constructed so as to give the correct asymptotic behavior in the non-degenerate limit: $\lim_{\eta\to-\infty} I_{\rm ex} = 2$, and in the completely degenerate limit: $\lim_{\eta\to\infty} I_{\rm ex} = 9/(2\eta)$. This expression is an alternative to Eqs. (39) and (40) of Kovetz et al. (1972).

Following Kovetz et al. (1972), we write the integrals as

$$\begin{aligned} \mathcal{I}+\mathcal{J} &= \beta^{-2}\int_0^\infty \frac{x_1^2\mathrm{d}x_1}{e^{u_1-\eta}+1}\int_0^\infty \frac{x_2^2\mathrm{d}x_2}{e^{u_2-\eta}+1} \\ &\times \left[\frac{2}{y_1y_2} - \frac{1}{x_1y_1x_2y_2}\ln\left(\frac{y_1y_2-1+x_1x_2}{y_1y_2-1-x_1x_2}\right)\right] \ , \end{aligned} \tag{95}$$

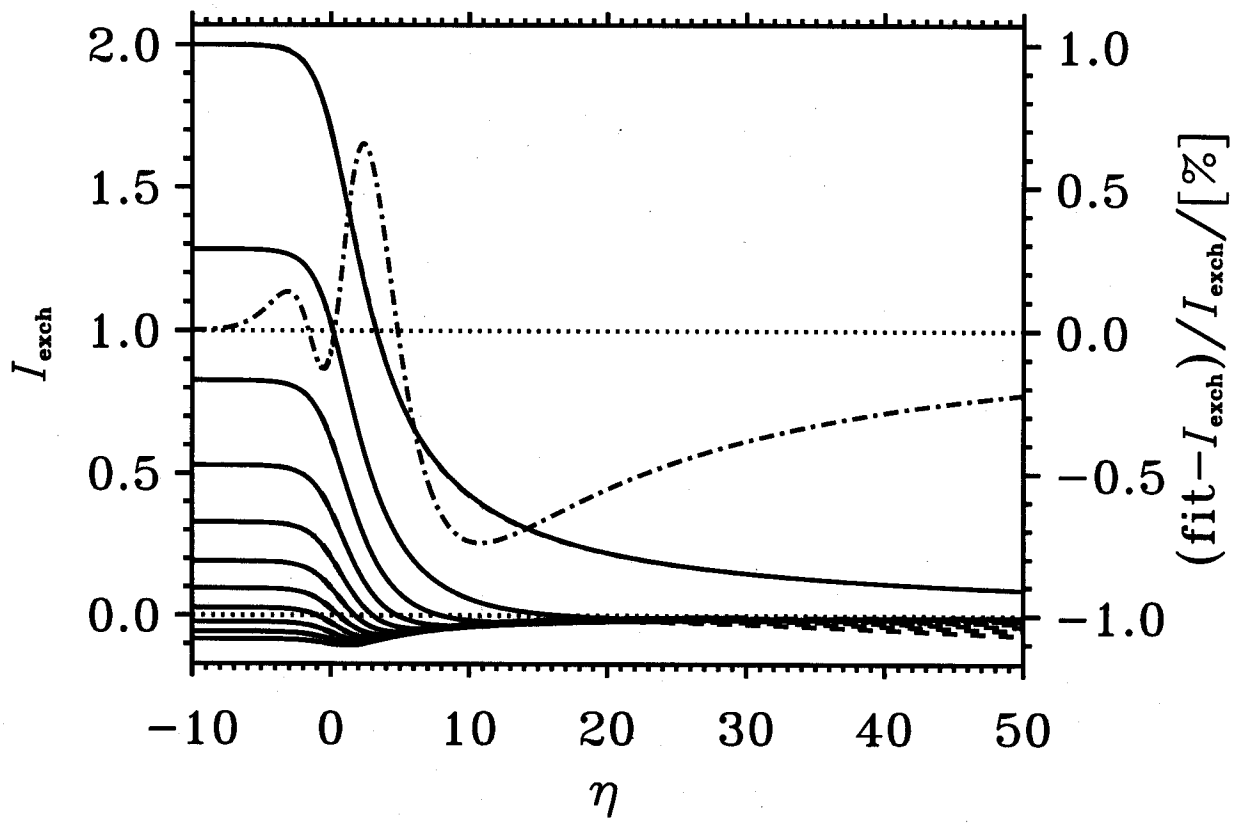

Fig. 9. The exchange integral, $J_{\mathrm{ex}}(\eta,\beta)$, as function of degeneracy parameter η. The upper solid line shows the numerical integration of $I_{\mathrm{ex}}(\eta)$, indistinguishable from the fit of Eq. (93). The dashed line (right hand axis) is the relative deviation between the numerical integration and the fit for I_{ex}. The other lines show the behavior of J_{ex} with increasing β (in steps of 0.1) going from top to bottom. The fit of Eq. 103 is shown with dashed lines, but only discernible above $\eta \simeq 30$.

where $x_i = p_i/mc, y_i = \sqrt{1+x_i^2}$ and $u_i = \varepsilon_i/k_{\mathrm{B}}T$ are the dimension-less momenta, energies (including rest-mass) and kinetic energies for the two interacting (identical) particles. We re-write in terms of u_i and get in the general case

$$\begin{aligned} \mathcal{I}+\mathcal{J} &= \int_0^\infty \frac{\mathrm{d}u_1}{e^{u_1-\eta}+1}\int_0^\infty \frac{\mathrm{d}u_2}{e^{u_2-\eta}+1} \\ &\times \left[4\beta\sqrt{u_1u_2}\sqrt{1+\tfrac{1}{2}\beta u_1}\sqrt{1+\tfrac{1}{2}\beta u_2}-\ln\mathcal{A}\right], \end{aligned} \tag{96}$$

where the argument of the logarithm is

$$\mathcal{A} = \frac{\beta u_1 u_2 + u_1 + u_2 + 2\sqrt{u_1 u_2}\sqrt{1+\frac{1}{2}\beta u_1}\sqrt{1+\frac{1}{2}\beta u_2}}{\beta u_1 u_2 + u_1 + u_2 - 2\sqrt{u_1 u_2}\sqrt{1+\frac{1}{2}\beta u_1}\sqrt{1+\frac{1}{2}\beta u_2}} \,. \tag{97}$$

From Eq. (54), we recognize the first term in the square-bracket of Eq. (96) as $4F^2_{1/2}(\eta,\beta)$.

In the non-relativistic case we get

$$\mathcal{I} = -\int_0^\infty \frac{\mathrm{d}u_1}{e^{u_1-\eta}+1}\int_0^\infty \frac{\mathrm{d}u_2}{e^{u_2-\eta}+1}\ln\mathcal{A}^{\mathrm{NR}} \tag{98}$$

with

$$\mathcal{A}^{\mathrm{NR}} = \frac{u_1+u_2+2\sqrt{u_1u_2}}{u_1+u_2-2\sqrt{u_1u_2}} \,. \tag{99}$$

Since the non-relativistic part has been solved through Eqs. (91) and (92), we only seek the relativistic correction

$$\begin{aligned} \mathcal{J} &= 4\beta F^2_{1/2}(\eta,\beta) \\ &- \int_0^\infty \frac{\mathrm{d}u_1}{e^{u_1-\eta}+1}\int_0^\infty \frac{\mathrm{d}u_2}{e^{u_2-\eta}+1}\ln\left(\frac{\mathcal{A}}{\mathcal{A}^{\mathrm{NR}}}\right) \,. \end{aligned} \tag{100}$$

This integrand lends itself to expansions in the non-relativistic Fermi-Dirac integrals, as carried out by Kovetz et al. (1972). Since our code already evaluates relativistic Fermi-Dirac integrals, we instead perform the expansion in terms of $F_\nu(\eta,\beta)$, Taylor-expanding

$$\frac{\mathcal{A}/\mathcal{A}^{\mathrm{NR}}}{\sqrt{1+\frac{1}{2}\beta u_1}\sqrt{1+\frac{1}{2}\beta u_2}} \,, \tag{101}$$

in u_1 and u_2.

After collecting terms with the same combinations of powers of u_1 and u_2, we finally obtain

$$\begin{aligned}\mathcal{J}(\eta,\beta) &= 3\beta F_{1/2}^2(\eta,\beta) + \frac{3}{4}\beta^2 F_{1/2}(\eta,\beta)F_{3/2}(\eta,\beta) \\ &+ \frac{1}{48}\beta^3\left[7F_{3/2}^2(\eta,\beta) + 15F_{1/2}(\eta,\beta)F_{5/2}(\eta,\beta)\right] \\ &- \frac{1}{768}\beta^4\left[95F_{3/2}(\eta,\beta)F_{5/2}(\eta,\beta) + 105F_{1/2}(\eta,\beta)F_{7/2}(\eta,\beta)\right] ,\end{aligned} \tag{102}$$

to the fourth power in β.

This Taylor expansion is, however, only valid in a rather small regime. In order to improve on this, with only a slight sacrifice of accuracy, we generalize Eq. 102 to

$$\begin{aligned}\mathcal{J}(\eta,\beta) &= e_0\beta F_{1/2}^2(\eta,\beta) + e_1\beta^2 F_{1/2}(\eta,\beta)F_{3/2}(\eta,\beta) \\ &+ \beta^3\left[e_2 F_{3/2}^2(\eta,\beta) + e_3 F_{1/2}(\eta,\beta)F_{5/2}(\eta,\beta)\right] \\ &- \beta^4\left[e_4 95F_{3/2}(\eta,\beta)F_{5/2}(\eta,\beta) + e_5 F_{1/2}(\eta,\beta)F_{7/2}(\eta,\beta)\right] ,\end{aligned} \tag{103}$$

and perform a χ^2-minimization fit for the coefficients. The result is listed in Tab. 5.

Derivatives of $\mathcal{J}$ are listed in App. ??.

Coulumb interactions beyond Debye-Hückel

Going beyond the Debye-Hückel theory is rather cumbersome, due to the long-range nature of the Coulumb interactions. Density-expansions of the equation of state now

Table 5. Coefficients for $J_{\rm ex}$, Eq. (103)

i	e_i
0	1.51561928
1	0.26835826
2	0.01595827
3	-0.06476090
4	0.00468264
5	-0.00243785

reach $n_{\rm e}^5$ (DeWitt et al. 1995), but subsequent terms will take an even larger effort to derive.

As an alternative, one can employ Monte-Carlo- and Hyper-Netted-Chain-simulations of the one-component-plasma (OCP) to determine the deviations from the Debye-Hückel free-energy, $F_{\rm DH}$. The main result from these simulations, is the internal energy, U, which can be integrated to give the free-energy: $F(\Gamma) = \int_0^\Gamma U(\Gamma')\mathrm{d}\Gamma'/\Gamma$, where $\Gamma = (\Lambda^2/3)^{1/3}$ and the plasma-parameter (for a particular particle species, α)

$$\Lambda_\alpha = \frac{\tilde{Z}_\alpha \tilde{z} e^2}{\lambda_{\rm D} kT} \ . \tag{104}$$

We express the free-energy as a harmonic average of the Abe cluster-expansion (Abe 1959) for low density and the free-energy of a fluid, $F_{\rm fl}$, as found by Stringfellow et al. (1990), plus a bridging-term and the zero-point, F_0, of the fluid-term,

$$\frac{1}{g(\Lambda)} = \frac{1}{g_{\rm Abe}} + \frac{1}{g_{\rm fl} + g_0 + b_4 \Lambda^{e_4}} \tag{105}$$

Table 6. Coeffecients for $g(\Lambda)$, Eq. (106)

i	b_i	e_i
1	1.87077570	-1/3
2	-4.53518904	-7/9
3	-0.18176156	-11/9
4	2.33750105	-1.72492756
5	3.59275987	——
6	0.48894000	——

where $g_x = F_x(\Lambda)/F_{\rm DH}$, with DH denoting the Debye-Hückel-term. We differentiate this expression with respect to Γ, to obtain the corresponding $g_U = U/U_{\rm DH}$. This we then fit to the Monte-Carlo results of Slattery et al. (1982) for $\Gamma = [1;150]$, Stringfellow et al. (1990) for $\Gamma = [150;200]$ and hyper-netted-chain simulations for $\Gamma = [0.1;0.9]$. For $\Gamma < 0.06$ we fit to the Abe-expansion.

The best fit of the fluid-phase by Stringfellow et al. (1990) combined with our fit, results in

$$g_{\rm fl} + g_0 + b_4\Lambda^{e_4} = b_1\Lambda^{e_1} + b_2\Lambda^{e_2} + b_3\Lambda^{e_3} + b_4\Lambda^{e_4} + \frac{b_5 + b_6 \ln\Lambda}{\Lambda} \qquad (106)$$

with coeffecients as listed in Tab. 6.

We need to check for self-consistency of the plasma potential, in the sense that the potential energy of ion m in the field around ion n has to be the same as that of

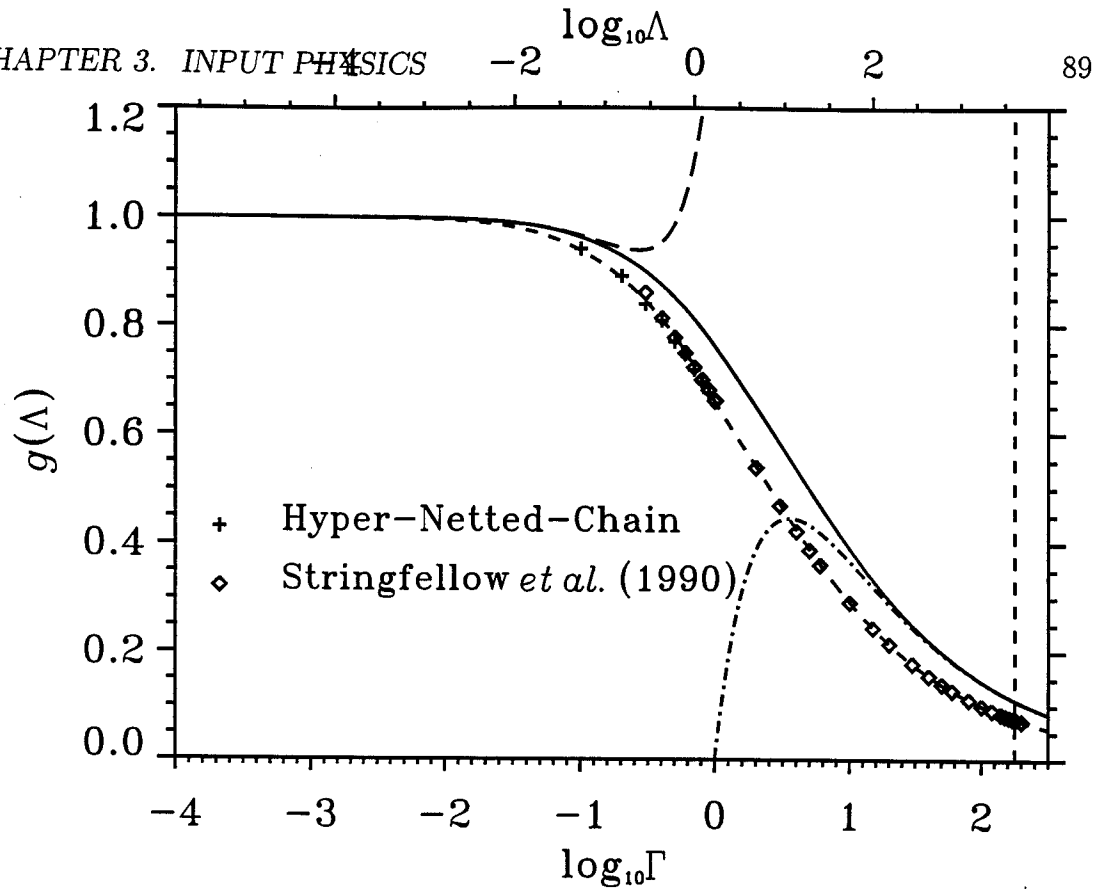

Fig. 10. The effect of higher order correlations on the free energy. The solid line is our fit to $g = F/F_{\rm DH}$, Eq. (105) and the dashed line is the corresponding $g_U = U/U_{\rm DH}$. The long-dashed line diverging at -0.5, is the Abe cluster expansion (Abe 1959), and the dot-dashed line is the fit to the fluid-phase free-energy presented in Stringfellow et al. (1990). The vertical dashed line shows the location of the transition to the crystalline phase.

n in the field around m. This means that

$$\frac{\partial V_n(0)}{\partial \tilde{Z}_m} = \frac{\partial V_m(0)}{\partial \tilde{Z}_n}, \tag{107}$$

where n and m refers to *single* ions, not *species* of ions. Writing $V_n(0) = e\tilde{Z}_n\kappa_{\rm D}g(\Lambda_n)$, the derivative is

$$\begin{aligned}\frac{\partial V_n(0)}{\partial \tilde{Z}_m} &= e\tilde{Z}_n\frac{\partial \kappa_{\rm D}}{\partial \tilde{Z}_m}g(\Lambda_n) + e\tilde{Z}_n\lambda_{\rm D}\frac{\partial g}{\partial \Lambda_n}\frac{\partial \Lambda_n}{\partial \tilde{Z}_m} \\ &\propto \tilde{Z}_n\tilde{Z}_m g(\Lambda_n) + \tilde{Z}_n\frac{\partial g}{\partial \Lambda_n}\frac{\partial \Lambda_n}{\partial \tilde{Z}_m}.\end{aligned} \tag{108}$$

If g contains powers of Λ_n different from 0 or 1, we see that Λ_n can not depend explicitly on $\tilde{Z}_n$. Also the average charge, z, from Eq. (104), need to be a root-mean-square average, in order for the differential to be proportional to $\tilde{Z}_n\tilde{Z}_m$, as in the Debye-case.

Comparing with Eq. (104), we then obtain our choise for Λ,

$$\Lambda_\alpha = \Lambda = \frac{V}{4\pi N_{\rm tot}}\lambda_{\rm D}^{-3} \ , \tag{109}$$

consistent with *e.g.*, Graboske et al. (1975). Using this Λ in the expression for the Debye-Hückel free energy, we can re-write Eq. (60)

$$F_{\rm DH} = -\tfrac{1}{3}N_{\rm tot}k_{\rm B}T\Lambda \tag{110}$$

Including the quantum diffraction from Sect. 3.3.5 just adds another term, also proportional to $\tilde{Z}_n\tilde{Z}_m$, as γ_{nm} only depends on $\tilde{Z}_m$ through $\kappa_{\rm D}$ [*cf.* Eq. (79)]. This also means that both methods, an average $\bar{\tau}$ or explicit $\tau(\gamma_{nm})$, will be equally self-consistent.

The complete free energy of coulomb interactions is then

$$F_4 = -\tfrac{1}{3}N_{\rm tot}k_{\rm B}T\Lambda g(\Lambda)\bar{\tau} + F_{\rm ex} \ . \tag{111}$$

Shielding by bound electrons

$\tilde{Z}$ refers to the effective charge including the contribution from partly shielded core charges of atoms or incompletely stripped ions, shielded by the bound electrons. Assuming a simple exponential (s-orbital) distribution of electrons in the atoms/ions, the effective charge felt at distance r is

$$\begin{aligned} Z_\alpha(r) &= Z_{0,\alpha} + \Delta Z_\alpha \left(1 - \frac{1}{2r_\alpha^2}\int_0^r r'^2 e^{-r'/r_\alpha} \mathrm{d}r'\right) \\ &= Z_{0,\alpha} + \Delta Z_\alpha e^{-r/r_\alpha}\left[\frac{1}{2}\left(\frac{r}{r_\alpha}\right)^2 + \frac{r}{r_\alpha} + 1\right] \end{aligned} \tag{112}$$

where ΔZ_α is the atomic number of particle α minus its net charge, $Z_{0,\alpha}$. We then average this over the volume V and obtain the average effective charge, felt by homogenously distributed particles,

$$\begin{aligned} \tilde{Z}_\alpha &= \frac{3}{R_\alpha^3}\int_0^{R_\alpha} r^2 Z_\alpha(r)\mathrm{d}r \\ &= Z_{0,\alpha} + \Delta Z_\alpha \times \\ &\left[60\rho_\alpha^3 - \tfrac{3e^{-1/\rho_\alpha}}{\rho_\alpha}\left(\tfrac{1}{2} + 3\rho_\alpha + 10\rho_\alpha^2 + 20\rho_\alpha^3 + 20\rho_\alpha^4\right)\right], \end{aligned} \tag{113}$$

where $\rho_\alpha = r_\alpha/R_\alpha$ and $R_\alpha^3 = 3V/(4\pi N_\alpha)$. The term inside the bracket, makes the transition from 0 to 1 in the interval $\rho = 0.03$–3.

In the previous version of the MHD EOS, the interactions with neutral particles, were accounted for by means of a first order approximation to hard sphere model. As this could be done, using the occupation probabilities, it was possible to include

the effect of highly excited atoms, having large radii.

The second order term was also included, although assuming all particles to be in their groundstate, through the Ψ-term, analyzed by Trampedach & Däppen (2004b). This rather ad-hoc term can now be abandoned.

The hard-sphere model is an unphysical model, as the model is undefined for high densities. Apart from wrecking havoc with numerical schemes for solving the equations, this is also unphysical as the interactions at small distances should merely approach the Coulumb interactions between the bare charges of the nuclei. This is exactly what is described by using the effective charge, $\tilde{Z}$, from Eq. (112).

The new F_4

We summarize our changes to the Coulomb free energy,

$$F_4 = g(\Lambda)\bar{\tau}F_{\rm DH} + F_{\rm ex} \ , \tag{114}$$

where $g(\Lambda)$ accounts for the higher-order terms in the Coulomb interactions, arising from the long-range nature of the Coulomb potential. The quantum diffraction-term, $\bar{\tau}$, accounts for the overlapping of particle wave-functions in close encounters, effectively removing the short-range divergence of the Coulomb potential. The exchange free energy, $F_{\rm ex}$, accounts for the interactions between wave-functions of identical particles.

In addition to these changes, we have also changed all occurences of particle charges from their net-charge, Z_α, to an effective charge, $\tilde{Z}_\alpha$, of particles of species α.

This effective charge is the volume-averaged charge, assuming s wave-functions for all electrons bound in species α, going from Z_α at low density, to the charge of the bare nucleus for inter-particle distances much smaller than the extent of the electron orbitals.

Using this effective charge, supplies small seed-charges, which are needed for the pressure ionization to set in, via the occupation probabilities. Using just the fixed net-charge, Z, the plasma cannot pressure ionize at low temperatures and the original MHD EOS therefore included a hard-sphere-term in the occupation probabilities, plus an ad-hoc approximation to higher-order hard-sphere interactions, Ψ. The latter term was analyzed by Trampedach & Däppen (2004b) and found to be of very little consequence for stars more massive than about $0.4\,M_\odot$.

3.3.6 Improved micro-field distribution

The occupation probabilities of the MHD EOS is based on the ionization of excited atoms by fluctuating electric fields, as described by Pillet et al. (1984). The proccess is itterative and goes as follows: The Stark splitting of levels moves the electron up while the next higher level is moved down, crossing the occupied level and allowing the electron to cross over. The field then changes sign, moving the level with the electron, up to meet the next, down-shifted level, and the procces continues till the atom is ionized.

The effeciency and range of this proccess clearly depends on the distribution of amplitudes of this fluctuating electric field. A higher probability for large fields

will make it less likely for even low lying states to survive, and will make pressure-ionization very effecient and *vice verca.*

The original MHD EOS use a linear approximation to the Holtzmark micro-field distribution, which itself (Holtzmark 1924) is the result for an interaction free plasma, *i.e.*, the low density limit. Nayfonov et al. (1999) implemented analytical fits to a higher order theory, and we, in turn, have implemented their work as part of the new MHD EOS.

Our implementation differs a little from that of Nayfonov et al. (1999), in that it is not optimized for speed but for flexibility. Our modular approach allows for any formulations of the micro-field distribution to be employed in the occupation-probabilities.

Following Hummer & Mihalas (1988), the propability of an electronic state i in particles of species s to survive despite fluctuating electric fields, is

$$w_{is} = \int_0^{F_{is}^{\rm cr}} P(F)dF \equiv Q(F_{is}^{\rm cr}) \ , \tag{115}$$

where $F_{is}^{\rm cr}$ is the critical field-strength for ionization of this state, and $P(F)$ is the microfield distribution-function, and $Q(F)$ is the accumulated microfield distribution-function.

The field-strength is usually expressed in units of the field-strength due to pre-turbers at the average ionic distance from the perturbed particle, F_0, *i.e.*, $\beta = F/F_0$.

In the MHD EOS the approximation

$$F_0 = a_0^2 N_{\rm e} \left(\frac{16\pi^2}{9N_{\rm ion}} \right)^{1/3}, \tag{116}$$

is used, with $N_{\rm ion} = \sum_{\alpha \neq {\rm e}} N_\alpha$, and a_0 being the Bohr radius.

The critical field-strength for ionization of level i of particle-species s with ionization-energy χ_{is}, is

$$\beta_{is} = 16^{-2/3} \frac{K_{is} \chi_{is}^2 / e^4}{\tilde{Z}_{is}+1} \left[\sum_{\alpha \neq e} N_\alpha \zeta_\alpha \right]^{-2/3}. \tag{117}$$

The quantum-correction factor, K_{is}, as given in Hummer & Mihalas (1988), is

$$K_{is} = \begin{cases} \frac{16}{3} \left(\frac{n}{n+1} \right)^2 \frac{n+7/6}{n^2+n+1/2} & {\rm n} > 3 \\ 1 & {\rm n} \leq 3 \end{cases} \tag{118}$$

where n is the principal quantum-number of state i.

The original MHD formulation used a rough fit to the Holtzmark distribution

$$Q_{\rm orig}(\beta_{is}) = e^{-\beta_{is}^{-3/2}}, \tag{119}$$

whereas Nayfonov et al. (1999) introduced

$$Q(\beta_{is}) = \frac{f(\beta_{is}, Z_s, a)}{1 + f(\beta_{is}, Z_s, a)}, \tag{120}$$

with

$$f(\beta_{is}, Z_s, a) = \frac{C_1(Z_s, a)\beta_{is}^3}{1 + C_2(Z_s, a)\beta_{is}^{3/2}} \ . \tag{121}$$

where

$$C_1(Z_s, a) = P_1(X + P_5 Z_s a^3) \tag{122}$$

and

$$C_2 = P_2 X \ , \quad X = (1 + P_3 a)^{P_4} \ . \tag{123}$$

The coeffecients were fitted to calculations based on the micro-field distribution functions by Hooper (1966; 1968).

The resulting derivatives are listed in App. ??.

3.3.7 Including more molecules

We wish to include more molecules in this EOS, in order to be able to use it as a foundation for calculations of atmospheric opacities. The current calculations of atmospheric opacities are often based on crude and old fashioned EOS, sometimes lacking thermodynamic consistency. Also, the bound-free metal opacities are often outdated, which we wish to remedy, by merging the metal opacities from the opacity project (OP) and the improved calculations carried out as part of the iron project (IP) (Hummer et al. 1993) with those of modern molecular line databases Parkinson 1992; Jørgensen 2002, and references therein).

Molecules other than H_2 and its ion, will necessarily exist in much lower concentrations, and will therefore have a smaller net effect on the thermodynamics. We

therefore relax our precision requirements a little, and settle for parameterized partition functions, instead of including a detailed treatment of all bound roto-vibrational and electronic states.

The entropy associated with a partition function Q is

$$TS = E + Nk_{\rm B}T\ln Q \tag{124}$$

and therefore the Helmholtz free energy is

$$F = E - TS = N\left[E_0 - k_{\rm B}T\ln Q\right], \tag{125}$$

where E_0 is the dissociation energy of the molecule with respect to the zero-point of the implicated elements. For CH_2, for example, we have

$$\begin{aligned} E_0({\rm CH_2}) &= D_0({\rm CH_2}) + E_0({\rm C}) + 2E_0({\rm H}) \\ &= D_0({\rm CH_2}) + D_0({\rm H_2})\ , \end{aligned}$$

as neutral atoms are the zero-point for carbon and H_2 is the zero-point for hydrogen.

Sauval & Tatum (1984) give five-term expansions and coefficients for the partition functions of 300 diatomic molecules, expressed as

$$\log_{10} Q = \sum_{n=0}^{4} a_n (\log_{10}\theta)^n, \tag{126}$$

where $\theta = (k\ln 10)^{-1}/T \simeq 5040\,{\rm K\,eV^{-1}}/T$. Irwin (1981) merged this list, with the

JANAF list of poly-atomic molecules. By computing the EOS and opacities with the full set of molecules, he determined which of these molecules are significant for various stellar chemical compositions. Of these, we selected the 414 molecules containing only one or two different chemical elements including, *e.g.*, H_2O, H_2S and CH_3. Among the molecules we consider, 315 are diatomic.

We reformulate the fitting formula, Eq. (126) in terms of the natural logarithm, $b_n = (\ln 10)^{1-n} a_n$, to simplify the derivatives (See App. ??). This gives the bound state contribution, F_2, to the free energy from molecules of type k, as

$$F_{2,k}(Q) = N_k \left[E_0 - k_B T \sum_{n=0}^{m_k} b_{kn} (\ln\theta)^n \right] . \tag{127}$$

We model pressure dissociation by multiplying the partition function at zero density, Q_0, by a density dependent term

$$f_Q = \left[\left(a_1 \varrho^{-1/3} + a_2 T^{e_1} \varrho^{e_2} \right)^3 + 1 \right]^{-1} , \tag{128}$$

so that

$$Q = Q_0 \left[1 - f_Q(\varrho, T) \right] . \tag{129}$$

This expression fits the pressure-dissociation of the H_2- and H_2^+-molecules, which is obtained from explicit accounting of 348 and 472 roto-vibrational levels, respectively, treated in the same way as the atomic and ionic species as described in the rest of the present paper.

In our approximate treatment of molecules, we neglect dependencies of the pa-

rameters a_1, a_2, e_1 and e_2 on chemical composition, and fit them to a table of H_2- and H_2^+-partition functions calculated for our $Z = 0.04$-mixture (See Sect. 3.3.2). This results in

$$e_1 = -4.15 \quad \text{and} \quad e_2 = -0.117 \tag{130}$$

The dissociation reactions are

$$n_X X + n_Y Y \longleftrightarrow X_{n_X} Y_{n_Y} \ , \tag{131}$$

which gives rise to the stoichiometric relations

$$\frac{\partial F}{\partial N_{X_{n_X} Y_{n_Y}}} - n_X \frac{\partial F}{\partial N_X} - n_Y \frac{\partial F}{\partial N_Y} = 0 \ . \tag{132}$$

The number conservation equations now read

$$\sum_m n_{km} N_m + \sum_{j=1}^{J_k} N_{jk} = \alpha_k N_{\rm tot} \tag{133}$$

where index, m runs over all molecules containing atoms of species k, and j runs over all ionization stages of species k. α_k is the normalized number fraction of species k including all stages of ionization/dissociation.

In Fig. 11 we show the number densities of all species considered in a $Y = 0.24, Z = 0.04$-mix with the metals comprised of C, N, O and Ne. The various line-styles were employed to make it easier to follow the individual species, which are labeled at their maximum density. The thin, solid lines are the results using the EOS

of the Uppsala-package, which is part of the MARCS stellar-atmosphere-code.

We see that the two versions are fairly close on the scale of Fig. (11), but we also notice that the Uppsala-package systematically under-estimates most of the molecules by 10–30% and the NH-molecule by a full 100%. The electron- and H^--ion densities, on the other hand, are over-estimated by about 5%, as seen in Fig. (12). The comparisons are performed on a solar model and the vertical dashed lines in both plots, marks the solar $T_{\rm eff} = 5777\,{\rm K}$.

The differences are mostly due to the update of molecular dissociation-energies and partition-functions, going from those of Tsuji (1973) to those of Irwin (1981).

3.3.8 Energy levels of the H_2- and H_2^+-molecules

In the original MHD EOS (Mihalas et al. 1988) the empirical anharmonic-oscillator and vibrating rotator constants by Herzberg & Howe (1959) were used, resulting in 284 roto-vibrational levels of the ground electronic state (it was found that excited electronic states would only have a marginal impact on the EOS). For the present work, we employ the 305 levels observed by Dabrowski (1984), supplemented by 43 levels from the *ab initio* calculations by Waech & Bernstein (1967), as presented in Irwin (1987).

Level-energies for the H_2^+-ion was based on the dynamical constants evaluated by Vardya (1966), adjusted to obtain agreement with the calculation of Hunter et al. (1974) for the higher levels. We presently use 472 levels from ().

These changes have a rather marginal effect on the EOS in the solar case—even

on the scale of helio-seismology. The effect on pressure and χ_ϱ is to lower them by less than 10^{-5} in bumps around temperatures of 5000 and 25000 K, and χ_T is increased in a similar fashion, by up to 5×10^{-5}. The adiabatic exponent, γ_1 is lowered by 5×10^{-5} in the solar atmosphere, below 7000 K and displays some ten times smaller wiggles around zero, up to 70000 K.

3.3.9 Conclusion

The improvements to the MHD equation of state, presented in the present paper, extend the range of applicability, compared to the original domain of stellar envelopes. In Sect. 3.3.7 we include 315 diatomic and 99 poly-atomic molecules and molecular ions, extending the range of this EOS to also include stellar atmospheres. Both in itself, and as the foundation for calculation of new atmospheric opacities, this will have implications for stellar atmosphere modeling. It also opens up the possibility of using the exact same EOS (and later also opacities) for detailed atmosphere modeling as for stellar structure and evolution calculations.

The treatment of quantum effects, *i.e.*, quantum diffraction (See Sect. 3.3.5) and exchange interactions (Sect. 9) improve the performance of the EOS for higher densities and in stellar cores. Of the two quantum effects, the exchange terms has the largest effect on a solar stratification, changing both the pressure and the adiabatic exponent in the radiative core.

We include relativistic effects, in the spirit of Gong et al. (2001b), but we also include relativistic effects in the degeneracy factors θ_e and Θ_e affecting the screening

length and the de Broigle wavelength of electrons, respectively. Relativistic effects are also included in the exchange integral, presented in Sect. 9. These changes only affects the high-temperature region, and has a measurable effect in the solar core.

The key ingredient in the MHD EOS is the occupation probabilities, determining the probability that a given state of an atom or ion is so heavily perturbed by collisions with other particles, that it is destroyed. The original occupation probabilities (Hummer & Mihalas 1988) included perturbations by charged particles, through the distribution of amplitudes of the fluctuating electric micro-field, approximated by a linear fit to the Holtzmark distribution. In Sect. 3.3.6 we include the work by Nayfonov et al. (1999) on a micro-field distribution that also accounts for correlation effects from the screening of ions by electrons. This introduces a lot of new structure in the EOS along a solar stratification, and will have consequences for inversions of solar p-modes (Christensen-Dalsgaard & Däppen 1992; Basu & Thompson 1996).

The original occupation probabilities also included a hard-sphere term, to account for perturbations by neutral particles. Since this term was only linear in density, an approximate second-order term, Ψ was included to ensure pressure ionization in cold plasmas. We have abandoned both of these terms for the more physical concept of effective charges (See Sect. 3.3.5); A neutral atom is not a hard-sphere, but a nucleon with a fixed charge, a some smeared-out distribution of electrons around it, resulting in a zero net-charge. Interactions between neutral atoms arise from close proximity, causing the electron wave-functions to overlap and only partially screen the nuclear charge. By introducing this concept all particles can be treated on an equal footing in the MHD EOS. This has a rather small effect in the Sun, close to the

top of the convection zone, but changes the EOS at lower temperatures and higher densities.

The single most important change is the incorporation of higher-order terms in the Coulomb interactions, which extends the validity of the EOS towards higher R, and brings the EOS in the solar convection zone closer to that of the OPAL EOS. There are still differences, however, and it will be interesting to see how the present work and the newly updated OPAL EOS (Rogers & Nayfonov 2002), fare in helioseismological inversions.

This new version of the MHD EOS will have a direct effect on stellar and solar structure calculations. If the changes cause an improved agreement with a helioseismological structure inversion, it might be relevant to re-visit the seismological determination of the solar helium abundance (Basu & Antia 1995) and convection-zone depth (Christensen-Dalsgaard et al. 1991; Basu & Antia 1997).

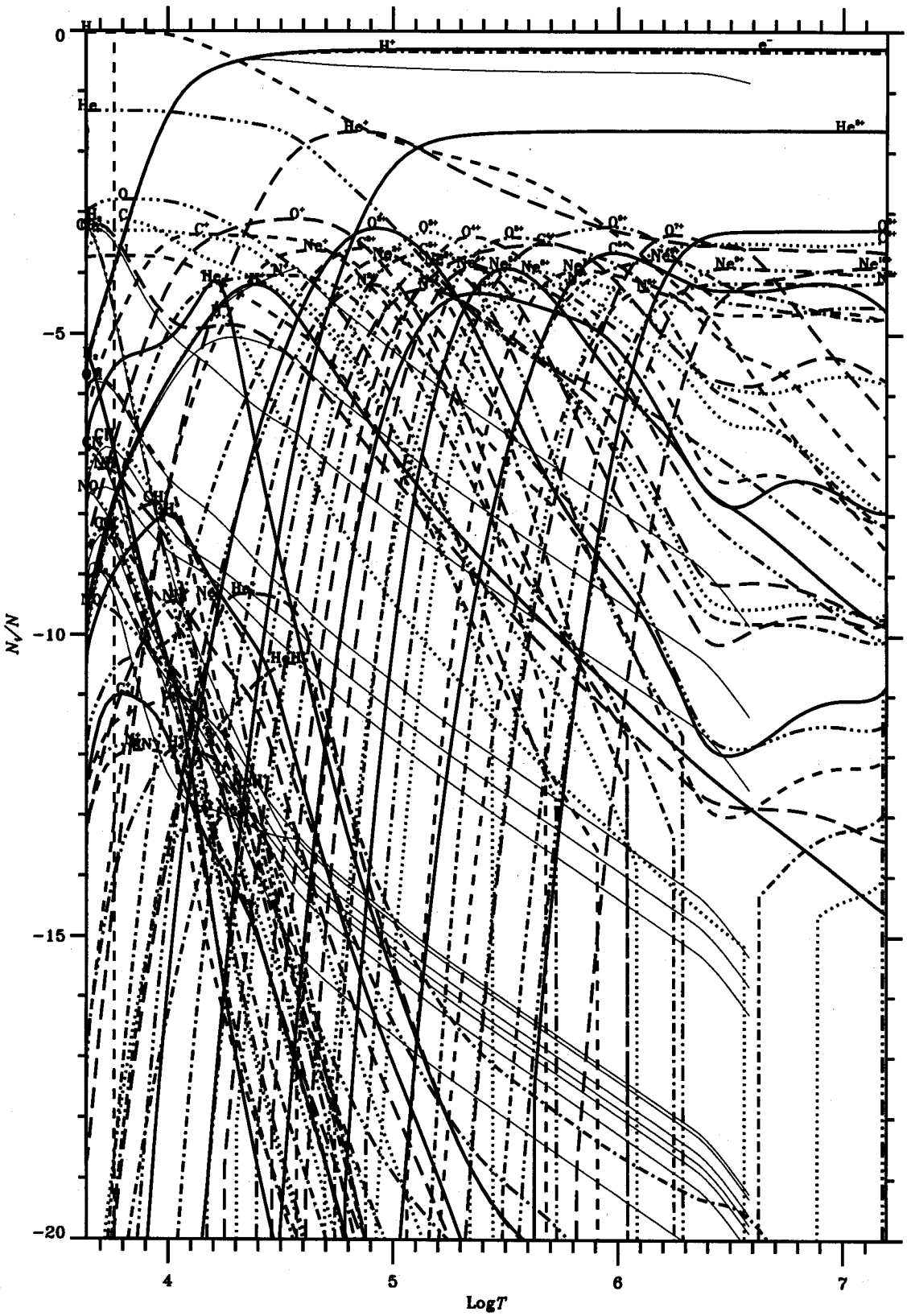

Fig. 11. The number densities of all considered particle species in a 6-element mixture.

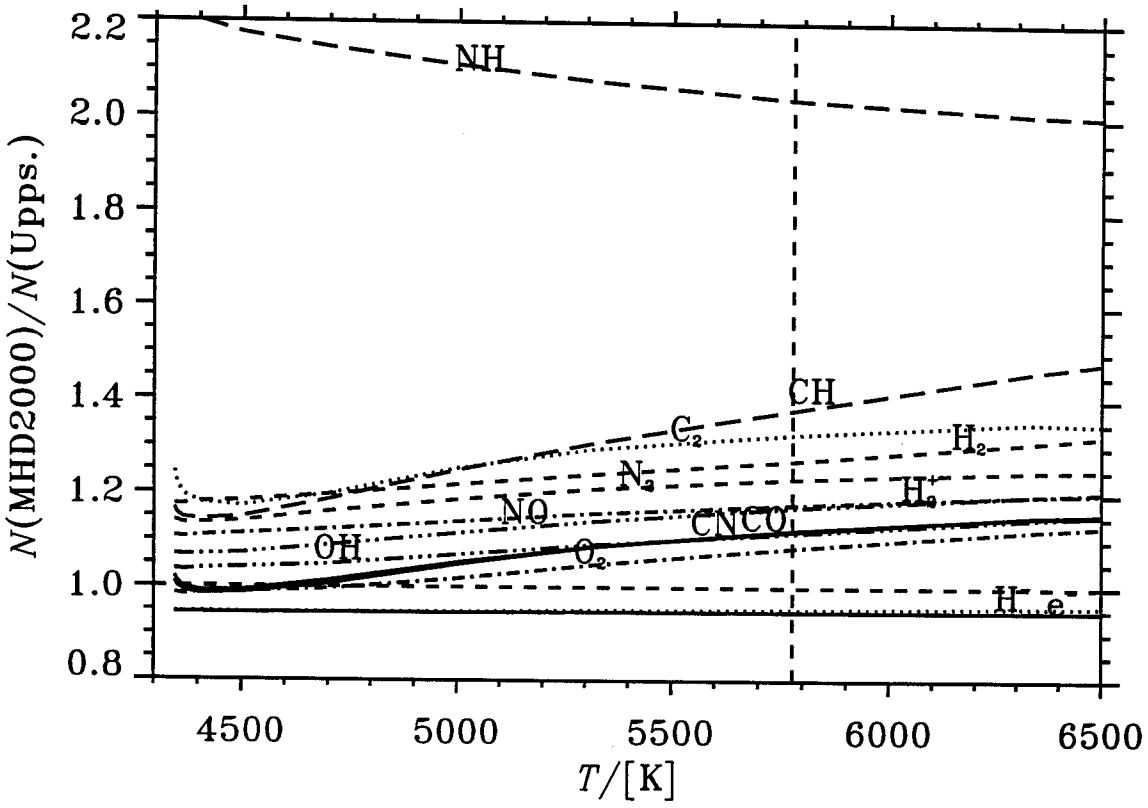

Fig. 12. Ratios of molecular number-densities between the present EOS and those obtained with the EOS in the Uppsala-package, which is part of the MARCS stellar atmosphere-models.

3.4 Opacity

In the early 1990's the astronomical community witnessed a quantum-leap in atomic physics. The OPAL-team (Rogers & Iglesias 1992a; Rogers & Iglesias 1992b) and the "Opacity Project" (OP) (Seaton 1995; Berrington 1997) published independant calculations of opacities for astrophysical applications. They were based on the OPAL EOS and the MHD EOS, respectively, which are compared in detail in Sect. 3.1.1. The level of sophistication in the calculations were hitherto unheard of—no more semi-classical approximations and hydrogen-like ions.

The two decades since then have seen an explosion in research in this field, both theoretical and experimental:

Aguilar et al. (2003) have measured the absolute photo-absorption by the Mg^{+}- and Al^{2+}-ions, Kjeldsen et al. (2002b) that by the Fe^{+}-ion, Kjeldsen et al. (2002a) that by the N^{+}- and O^{+}-ions and Kjeldsen et al. (2001) that of the C^{+}-ion. These measurements are very impressive, and once and for all demonstrate that the very complicated and intricate structures in photo-absorption coefficients that we have been treated to since the OP- and OPAL-opacies were first published, are actually real—not a mere figment of imagination of a quantum mechanic.

One of the main improvements in the *ab initio* calculations of absorption coefficients, is the inclusion of relativistic effects. The calculations are performed by means of the close-coupling R-matrix method (Seaton 1987), as was implemented in the OP work. As part of the iron project (IP) (Hummer et al. 1993), these calculations were extended to also include relativistic effects in the so-called Breit-Pauli

(BP) approximation and all-together this is called the Breit-Pauli R-matrix method (BPRM). The BP approximation includes spin-orbit interactions, which breaks the LS symmetry and gives rise to fine-structure and can even cause resonance lines below the ionization-treshold.

A detailed comparison between BPRM-calculations and experiment has been carried out by Nahar (2003) for the first four ions of oxygen. The agreement between theory and experiment is in general very impressive. The various resonances are not only in qualitative, but most often also in quantitative agreement, both with respect to position and strength.

Badnell & Seaton (2003) present a comparison between the original OP Rosseland opacity and a new calculation also including inner-shell absorption by C, O, S and Fe (a mixture chosen for comparison with OPAL). The comparison shows up to a 25% increase of the Rosseland opacity around $T = 4 \times 10^6\,\mathrm{K}$ and largest for high densities. These opacities are based on the Q-MHD (Nayfonov et al. 1999) formulation for the micro-field distribution, $P(F)$, as is also the case with the improvements to the MHD EOS presented in Sect. 3.2.5, the two therefore being compatible and consistent with each other. In the opacity work, $P(F)$ is used both for evaluating the occupation probability and hence the populations of the electronic levels of atoms and ions (See Sect. 4 of "MHD 2000" on p. ??), as well as for computing the Stark broadening of lines of hydrogenic ions.

Since MHD 2000 also includes molecules, we here have a chance to compute the first set of consistent, unified opacities, with monochromatic opacities at low temperatures, suitable for detailed atmosphere calculations, as well as Rosseland

opacities for stellar structure calculations. The former will of course be a valuable improvement for the convection simulations too.

The last decades opacity improvements also include a number of density effects. Allard et al. (1994; 1998) evaluated the electric dipole moment of two hydrogen atoms passing close to each other, and found that interactions with the bound states in the H_2-molecule introduced resonances in the wings of the Lyman lines of hydrogen, as well as provided a natural cut-off of the line-wings. The resonances are density dependent, some linear and some quadratic in density, and were soon found in the spectra of white dwarfs (Koester et al. 1996).

The dipole moments from hydrogen molecules or a helium atom and a hydrogen molecule passing each other, results in broad continous opacity (Borysow et al. 1989; Borysow & Frommhold 1989) dubbed Collision-induced absorption (CiA).

Both of these should be fairly trivial to include in the final opacities, greatly broadening the range of applicability, matching the range of the underlying EOS.

In light of the improvements to the high-density EOS and corresponding opacities, it would be interesting to continue the work by Ludwig et al. (1994) on simulations of convection in white dwarfs. Here the convection zone is so thin that it can be fully contained in the simulation domain, including convective overshoot at the base of the convection zone. Since there are several categories of pulsating white dwarfs, such convection simulations could be coupled with a seismological analysis to further constrain models of white dwarf structure, as well as their cooling history.

As work on the improved MHD EOS is not completed yet, the calculation of corresponding opacities is a project that will be organized in the near future.

Chapter 4

Radiative Transfer

4.1 Opacity sampling for 3D convection simulations

We, Trampedach & Asplund (2004), present a method for performing opacity sampling on a very small number of wavelengths, applicable for multi-dimensional and dynamic cases such as, *e.g.*, 3D simulations of convection. We show that we can reduce the number of sampled wavelengths by a factor of 2000 and still be within a percent of the result with 10^5 wavelength-points.

4.1.1 Introduction

In radiation-hydrodynamical 3D simulations of convection in stellar atmospheres, the coupling with radiation is crucial in determining the efficiency of convection (Nordlund 1985; Nordlund & Dravins 1990). A realistic treatment of radiation is

therefore important, and should as a minimum include the effects of spectral lines in some way. So far this has been done by binning the total (continous+lines) opacity according to strength and using as a source function, the accumulated source function of the wavelengths belonging to each bin (Nordlund 1982). We explain this *opacity binning* in more detail in Sect. 4.1.2.

Solar simulations show good agreement with line-profiles and bi-sectors, without the need for the usual macro- and micro-turbulence parameters (Asplund et al. 2000). Also the use of a horizontally- and temporally-averaged simulations, matched with a 1D solar model for the interior, greatly improves the agreement with observed high-degree p-modes (Rosenthal et al. 1999). There is also at least a superficial agreement with the granulation structure, although a more quantitative analysis has yet to be carried out. Simple Fourier-analysis is not adequate, as shown by Nordlund et al. (1997).

There is, however, still some disagreement with limb-darkening data, hydrogen Balmer-line profiles and the cores of strong lines. We also see a little too much flux in the ultra-violet. These minor, but significant remaining problems have prompted us to look into improvements to the scheme for solving the radiative transfer problem.

The most direct way of evaluating radiative transfer is to discretize in wavelength and use enough wavelength-points, N_λ, to capture the physics of the full calculation. This is the brute-force method, but it also is the only way to ensure convergence to the complete calculation. The method is called *opacity sampling* (OS) (Sneden et al. 1976) and is elaborated on in Sect. 4.1.3.

Since $N_\lambda \gtrsim 10^5$ are needed for randomly distributed wavelength-points to repro-

duce the full calculation, opacity sampling is prohibitive for multi-dimensional and dynamic cases. This has lead us to investigate whether a small number of wavelength-points can be carefully chosen so as to reproduce the main-effects of the full radiative transfer. In Sect. 4.1.4 we describe our method for choosing wavelengths and we compare (in 1D) the $N_\lambda \sim 10^5$ OS-case, with our new $N_\lambda \sim 50$ case in Sect. 4.1.5. We call our new method sparse or selective opacity sampling (SOS).

The motivation behind this work, is the anticipation that a more direct method for evaluating the radiative transfer, *i.e.*, using actual opacities and source functions instead of binned quantities, will more accurately span the range of a convective atmosphere. We address this issue in Sect. 4.1.6 where we compare the opacity sampling, the opacity binning and our new method, for a vertical slice of a solar simulation.

This is a continuation of work presented in (Trampedach & Asplund 2003).

4.1.2 Primer on Opacity Binning

Currently the simulations employ an opacity binning, or multi-group scheme, as described in detail by (Nordlund 1982). This scheme relies on a monochromatic, forward calculation performed on the average structure of the simulation; the calibration stratification. Wavelength-points are then grouped together depending on their opacity and the result of the of the 1D radiative-transfer calculation performed on the calibration stratification.

The discretized version of the radiative heating is

$$\int_\lambda \kappa_\lambda (J_\lambda - B_\lambda) \mathrm{d}\lambda \simeq \kappa \sum_i^{N_\lambda} x_i (J_i - B_i) w_i \ , \tag{134}$$

where we have defined the relative opacity

$$x_\lambda = \kappa_\lambda / \kappa \ , \tag{135}$$

with respect to κ, the standard opacity is defined in Eq. (141) below.

The next step is a reordering of the wavelength points into groups, i, where $j(i)$ is the set of wavelength points that fall in bin i. The bins of relative opacities are chosen to be logarithmically equidistant

$$x_i = 10^{ai}, \tag{136}$$

with $i = 0, 1, 2, 3$ and $a = 1$. A wavelength j belongs to bin i if τ_{λ_j} reaches unity within the interval $i - \frac{1}{2} < \log \tau < i + \frac{1}{2}$ of the standard optical-depth, $\mathrm{d}\tau = \varrho \kappa \mathrm{d}z$.

The weight of bin i is simply

$$w_i = \sum_{j(i)} w_{\lambda_j} \ . \tag{137}$$

The approximation inherent to the opacity-binning scheme, consists of assuming the x_j of all members, $j(i)$ of bin i, to display the same behaviour with depth. In that case the average opacity, x_i, and the average source-function of the bin, can be de-coupled

to yield the pseudo Planck functions

$$B_i w_i = \sum_{j(i)} B_{\lambda_j} w_{\lambda_j} \ . \tag{138}$$

This approximation is obviously rarely ful-filled. If the members of a given bin, correspond to lines of ions/atoms with similar excitation/ionization characteristics, the approximation will likely be valid. With a mix of molecular, and high- and low-excitation-potential atomic and ionic lines the approximation will not hold.

The pseudo Planck functions are functions of temperature only through the temperature dependence of B_λ, since the bin-membership of a wavelength is fixed for the whole temperature-/density-area covered by a given simulation.

To calculate the standard opacity, we observe that in optically thick layers the diffusion approximation holds and radiative transfer can be described in full by a single opacity, the *Rosseland mean opacity*

$$\frac{1}{\tilde{\kappa}} = \frac{\int_0^\infty \frac{1}{\kappa_\lambda + \sigma_\lambda} \frac{\partial B_\lambda}{\partial T} d\lambda}{\int_0^\infty \frac{\partial B_\lambda}{\partial T} d\lambda}, \tag{139}$$

where scattering, σ_λ, is included. For $\tau \to 0$, on the other hand, the intensity weighted mean

$$\langle \kappa \rangle J = \int_0^\infty \kappa_\lambda J_\lambda d\lambda \tag{140}$$

without scattering, reproduces the fluxes of the monochromatic solution (Mihalas 1978, Chapter 3.2). An ad-hoc bridging function is used to interpolate between the

two cases, resulting in the standard opacity

$$\kappa = e^{-30\tilde{\tau}^*}\langle\kappa\rangle^* + (1 - e^{-30\tilde{\tau}^*})\tilde{\kappa}^*. \tag{141}$$

The $*$ furtermore indicates that Eq. (139) is evaluated from the continuous opacity only, excluding lines, and

$$\langle\kappa\rangle^* = \frac{\sum_j \kappa_{\lambda_j} J_{\lambda_j} e^{-\tau_{\lambda_j}/2} w_{\lambda_j}}{\sum_j J_{\lambda_j} e^{-\tau_{\lambda_j}/2} w_{\lambda_j}}. \tag{142}$$

is weighted towards optically thin wavelengths.

The (pseudo) source-functions and the interpolated opacity are then used for the radiative transfer in the 3D simulations. The angular integration to obtain the mean intensity is evaluated by keeping the simulation box fixed and interpolating it to a tilted grid, exploiting the periodic horizontal boundaries. Only the rectangular part of the box having standard optical depth $\tau < 300$ is used for the radiative transfer calculations, and this part is furthermore rescaled to optimally resolve the temperature structure.

For each angle, the radiative transfer is thus solved $N_{\rm bin}$ times; we typically use $N_{\rm bin} = 4$, and $N_\theta = 2$ and $N_\phi = 4$ for the latitudinal and azimuthal angular resolution, respectively.

There are a number of weak points in the method, as implemented: The bin-membership is determined from the 1D average structure of the simulation, which will most likely not correspond to the stratification experienced by any of the rays

of light going through the simulation. Since radiative transfer is a highly non-linear problem, the heavy reliance on this reference stratification is troublesome.

The choice of bridging function between the optical deep and the optically thin opacities is rather arbitrary. The right limits are of course ensured with this expression, but the details of the transition are not.

Instead of the actual opacities of each bin $\sum_{j(i)} x_{\lambda_j} w_{\lambda_j}$, the log-equidistant opacities, x_i, are used. This approximation was used to minimize the size of the table, in the early days of these simulations, and can be abandoned now (Skartlien 2000).

Another weakness of the implementation of the opacity binning, is the calculation of Rosseland mean-opacities. The bf-(bound-free-)opacities are calculated for the whole table, whereas the bb (line-) contribution is only included in the 1D calibration stratification. The effect of lines is then extrapolated to the rest of the table, assuming the same ratio between opacities with and without lines along iso-τ contours. It turns out that points in the simulations that have the same optical depth, are highly correlated in ϱ and T, and fall along a narrow line.

There is no reason that the factor correcting for lines, should depend in any simple way on the optical depth, but the bridging function between optically thick and thin, should, and we simply employ the same extrapolation scheme for both.

We abandon most of these approximations in our SOS method, except for the reliance on a 1D calibration stratification. We show that the SOS method depends more weakly on the calibration model, than does the opacity binning, thus resulting in a more accurate local radiation field in the simulations. This will be addressed in Sect. 4.1.6.

4.1.3 Primer on Opacity Sampling

Opacity sampling (OS) consists of performing monochromatic radiative transfer for a large number of random wavelengths. It is a statistical method because of the random selection of wavelengths (in practice, equally spaced in, e.g., $\log\lambda$). Because of the extremely complicated behavior of stellar opacities, more than 10^4 wavelengths are needed before the procedure converges. For early type stars and metal-poor stars a larger number of wavelengths is needed, in order not to miss the rather few but important lines in their spectra. Full OS is therefore prohibitively expensive for 3D hydrodynamical simulations.

Conventional 1D stellar atmospheres have been modeled with opacity sampling by, *e.g.*, Plez et al. (1992), Kurucz (1995) and Asplund et al. (1997).

4.1.4 SOS

Our aim is to reproduce the $N_\lambda^{\rm OS} \sim 10^5$ OS solution, with orders of magnitude smaller number of wavelengths, $N_\lambda^{\rm SOS} \sim 50$. The straight-forward method, of going through all combinations of $N_\lambda^{\rm SOS}$ wavelengths, and finding the set with the smallest RMS deviation from the full solution, is rather prohibitive; It would require the computation of $(N_\lambda^{\rm OS})^{N_\lambda^{\rm SOS}}$ RMS-differences. We therefore have to perform some pre-conditioning of the problem to make it tractable. We do this by dividing the spectrum into $N_{\rm reg}$ regions and each region into $N_{\rm bin}$ bins, and then choose one wavelength that best represents the total of the bin. The RMS fitting is then carried out only within a bin or between two bins, reducing the dimension of the problem to the order of

$N_\lambda^{\rm OS}/N_\lambda^{\rm SOS}$ or $(N_\lambda^{\rm OS}/N_\lambda^{\rm SOS})^2$, with $N_\lambda^{\rm SOS} = N_{\rm reg} \times N_{\rm bin}$.

Our scheme for selecting the $N_\lambda^{\rm SOS}$ wavelengths is performed on the 1D reference stratification, and proceeds as follows:

1) We divide the spectrum into $N_{\rm reg}$ regions, by requiring each region to radiate the same amount of energy at $\tau = 1$.

2) In each region, the member-wavelengths are grouped together, or binned, according to the position of the minimum of the monochromatic radiative heating,

$$q_\lambda = \kappa_\lambda (J_\lambda - B_\lambda) \ , \tag{143}$$

where J_λ is the usual zeroth moment of the monochromatic intensity and B_λ and κ_λ are the monochromatic Planck-function and opacity, respectively. Note that this expression includes scattering despite the absence of the actual source function (Mihalas 1978).

The location of the maximum cooling (minimum of q_λ) is calculated as the center-of-mass of all cooling above $\tau_\lambda = 1$ (*i.e.*, $\tau_\lambda \leq 1$), and wavelengths with no cooling above that, are counted as continuum bins, *i.e.*, having cooling peak around $\tau_\lambda \sim 1$.

The limits of the bins are determined for each region, depending on the distribution of loci of heating minima. With equidistant bins, some bins will invariably turn up empty, but we also want to make sure that even sparsely populated regions of the τ-scale are represented well.

Our solution is to fit $N_{\rm bin}$ Gauss-functions, to the logarithm of the distribution function, substituting -2 for log(0), to make any non-zero regions of the distribution

function stick out prominently against the background. We also add in a small repulsive potential between the Gaussians, in order to avoid degeneracy. The limits of the bins are evaluated as the mid-point between the centers of the Gaussians. The whole procedure has proven very robust in real applications.

3) We have now chosen the $N_{\rm reg}$ regions and the $N_{\rm bin}$ bins, and need to decide on the criteria for choosing the $N_\lambda^{\rm SOS}$ wavelengths representing these bins. The key quantity for the simulations, is the radiative heating/cooling, q, which directly determines the effect of the radiation field on the hydrodynamics. We also need to ensure a physically meaningful connection to the equilibrium state and observables, in this case the flux. In principle the radiative flux can be determined from integration of the heating, but since the spatial deviation of $q_{\rm rad}^{\rm SOS}$ from $q_{\rm rad}^{\rm OS}$ will in general fluctuate wildly, a separate constraint on the flux is important. Secondarily, we also want to be able to calculate consistent radiative contributions to the pressure and internal energy of the stellar plasma. For this we need the zeroth and second moments of the radiation field; J and K, respectively. We also find it useful to demand that the total Planck function is close to the nominal $B = \sigma T^4/\pi$. A sixth quantity that could prove useful, is the Rosseland averaged opacity. This turns out to result automatically for $\tau \gtrsim 1$ when the five previous quantities have been fitted for, as is evident from Fig. 13.

We consequently fit for

$$f \equiv \left\{ \frac{q(\tau)}{|\min(q)|}, \frac{H(\tau)}{H_{\rm eff}}, \frac{B(\tau)}{J(10^2)}, \frac{J(\tau)}{J(10^2)}, \frac{K(\tau)}{K(10^2)} \right\} , \tag{144}$$

where $H_{\rm eff} = \sigma T_{\rm eff}^4/(4\pi)$ and σ is Stefan-Boltzmann's constant. The normalizations in Eq. (144) are necessary in order for the different quantities to carry similar weight in the fitting. The use of J, K and B at $\tau = 100$ is somewhat arbitrary, but it seems to result in a fair weighting compared to H and q.

4) We define the weight of bin j of region i, as

$$w_{ij} = \sum_{\lambda \in {\rm bin}_{ij}} w_\lambda \tag{145}$$

and

$$f_{ij} w_{ij} = \sum_{\lambda \in {\rm bin}_{ij}} f_\lambda w_\lambda \ , \tag{146}$$

and we similarly define w_i and f_i of region i.

5) For each region, we find the two bins with most members and fit the $N_{\rm bin} - 2$ other bins individually, minimizing RMS$(f_{ij} - f_\lambda)$, and using the weight, w_{ij}, on the resulting representative of that bin, f_{ij}^*.

6) The two remaining bins, j_1 and j_2, of region i, are optimized jointly to reproduce the remainder of the region

$$f_{i,12} w_{i,12} = f_i - \sum_{k=3}^{N_{\rm bin}} f_{ij_k} w_{ij_k} \ , \simeq [\epsilon f_{i,1}^* + (1-\epsilon) f_{i,2}^*] w_{i,12} \tag{147}$$

where $w_{i,12} = w_{i1} + w_{i2}$ and $\epsilon = \{0, 0.2, 0.4, 0.6, 0.8, 1\}$. For each combination, $\{j_1, j_2\}$, we compute the RMS deviation for the six values of ϵ, find the interpolated minimum and the associated $\epsilon_{\rm min}(j_1, j_2)$. The smallest of these interpolated minima then determines j_1 and j_2 and is used with $\epsilon_{\rm min}$ to finally find $f_{i,12}^*$.

7) This ends the task of finding the $N_{\rm bin}$ wavelengths $\lambda(i, j_k), k = \{1, \ldots, N_{\rm bin}\}$, reproducing region i, and the whole procedure is simply repeated for the other regions.

8) In the end, we refine the fit by optimizing the weights, $w_{ij} \rightarrow w^*_{ij}$, by means of a χ^2-minimization performed on the logarithmic weights (to ensure positive definite weights) and enforcing conservation of the total weight, $\sum_{ij} w^*_{ij} = \sum_1^{N_\lambda} w_{\lambda_l}$. This last step does improve the agreement between $f^{\rm OS}$ and $f^{\rm SOS}$, and we prefer to leave it in, despite the weakening of the definition of the weights.

4.1.5 1D radiative transfer

We have carried out the wavelength selection procedure, detailed in Sect. 4.1.4, on a number of MARCS models (Gustafsson et al. 1975; Asplund et al. 1997), as shown in Fig. 1. The atmosphere parameters are listed at the top of the plot. We have plotted both the full 10^5 wavelength MARCS results and our corresponding results with just 50 wavelengths, but the differences are only immediately visible in $\kappa_{\rm Ross}$ for which we did not fit. For the other quantities we also plotted the differences (dashed lines, right hand axis). The photospheric dip in the heating, $q_{\rm rad}$, arise from the transition from convective to radiative transport of the flux. In the second plot from the bottom, $3K$ is larger than B, which is larger than J, only diverging above the photosphere. In this plot we only plot the J-differences, which is representative of the B- and K-differences too. We see that our method is successful in reproducing the full radiation field to within a percent. The metal-poor atmosphere (middle-right) is easiest reproduced with few wavelengths, whereas the red giant (left) causes more

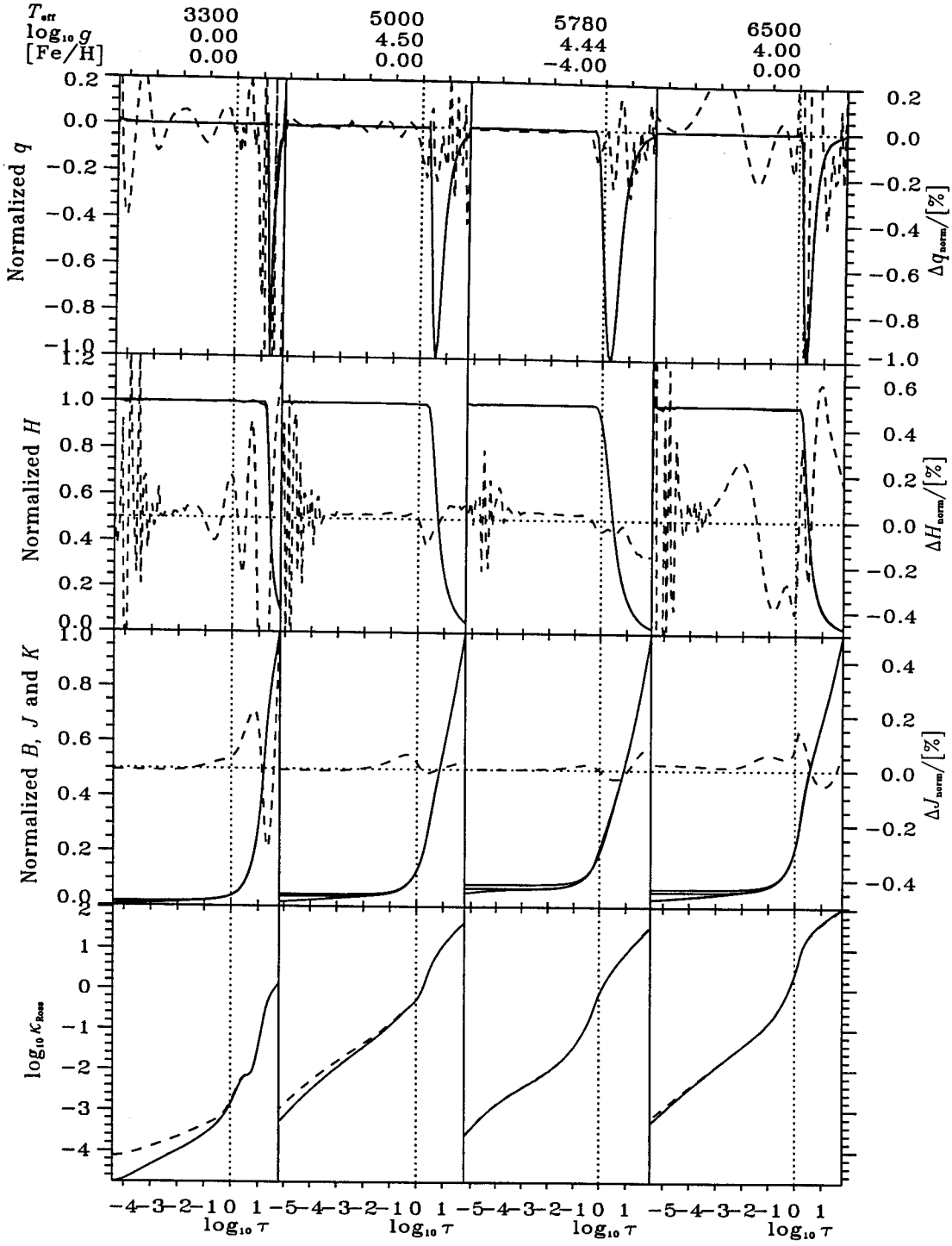

Fig. 13. Heating q, flux H, J, B, $3K$ and Rosseland opacity for four of the test cases (horizontally). In the three upper panels, the dashed line (right axis) is the differences in the sense SOS − monochromatic. In the lower panel the dashed line is the Rosseland opacity from our method. The horizontal dotted lines are the zero-points for the differences, and the vertical ones show the location of $\tau = 1$.

problems due to the many molecular lines in the rather cool atmosphere.

Notice that this is opposite the case for pure opacity sampling. The reason being that with SOS, we have the freedom to choose our wavelengths to cover the few but prominent lines, whereas with OS the wavelengths has to be chosen randomly. The SOS method is obviously not interesting for conventional 1D stellar atmosphere models, as it relies on a full OS evaluation of the radiative transfer in the reference stratification, as detailed in Sect. 4.1.4.

4.1.6 Spanning convection

In Fig. 14 we test the old and the new method on the heating in a vertical slice of a solar simulation snapshot (Stein & Nordlund 1998; Stein & Nordlund 1989; Asplund et al. 1998). We plot deviations from the "monochromatic" calculation, averaged over the horizontal dimension of the slice. Solid and dashed lines denote plain- and RMS-averages respectively, and the old opacity binning is shown with thin lines, and the new SOS method is shown with thick lines. The reference ("monochromatic") model in this case is based on the ODFs used in the ATLAS atmosphere-models of Kurucz (1992c), with 230 ODFs of 12 points, corresponding to 2760 "wavelength"-points. This is a far smaller set of wavelengths to choose from, and the fit for the 1D average of the slice is about 10 times worse than what we saw in Fig. 13 for the MARCS models (Note that this does not say anything about the accuracy of MARCS or ATLAS models). In the future, the plan is to base our wavelength selection on a OS calculation for the 1D average stratification of the simulation with 10^5 wavelengths,

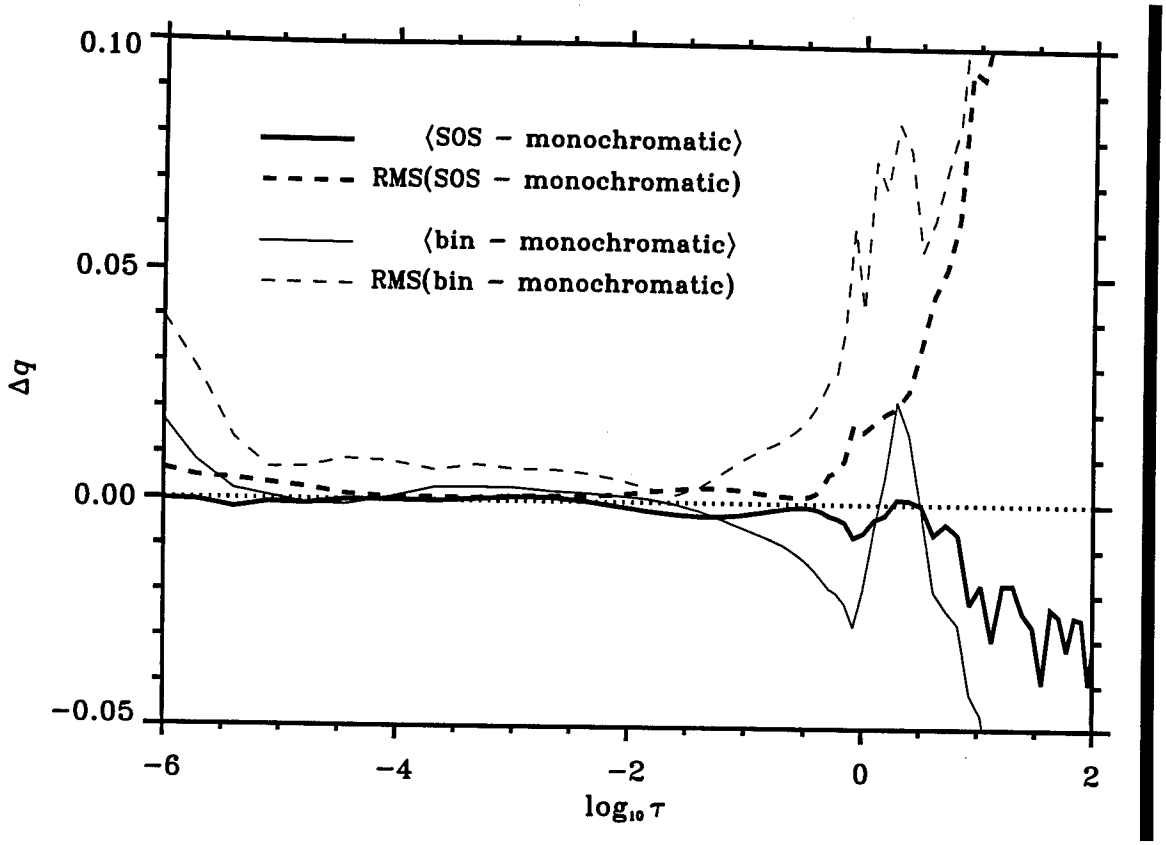

Fig. 14. Comparison of the heating from the opacity binning (bin, thin lines) and our new method (SOS, thick lines), with the "monochromatic" case (see text). A $\langle \ldots \rangle$ denotes horizontal averages over a 1.5×6 Mm, 82×200 point vertical slice from a solar simulation (solid). RMS denotes the corresponding horizontal root-mean-square averages (dashed lines).

but for now, we can test our new method on the ODF case. The accuracy should increase with more choices of wavelengths.

From Fig. 14 we see that our wavelength selection is more stable against convective fluctuations than the opacity binning method. Some of that is due to our new method explicitly fitting for $q(\tau)$ of the average structure, whereas the opacity binning is a forward calculation, with no feed-back mechanisms (i.e., no iterative fitting scheme). We see that both the average- and the RMS-deviations over the slice are smaller with our new method.

The transition from convective to radiative transfer of the flux, is accompanied by a radiative cooling-dip. In Fig. 13 we see the difference between the monochromatic and the binned case, exhibiting both a positive and a negative "bump" around $\log\tau \sim 1$. This is the tell-tale sign of the cooling-dip in the binned solution is located (on average) a little higher in the atmosphere, than is the case in the full OS solution. Such a feature is not present in the SOS solution.

4.1.7 Conclusion

This first feasibility analysis has shown that

1. It is indeed possible to find 50 wavelengths that can represent the radiative transfer of a full OS calculation with 10^5 wavelengths.
2. Both the heating and the first three moments of the intensity J, H, K are well reproduced.
3. Although the Rosseland opacity does not enter in our fitting criteria, it is reproduced to within 1% in the optical deep layers.
4. The proposed selective opacity sampling method is more stable against the convective fluctuations than the opacity binning.

We have yet to implement the new method in the 3D convection simulations, but these first tests are very promising.

Chapter 5

Improvements to stellar structure models, based on 3D convection simulations

As a part of the grander scheme, to better understand stars, improved models of stellar structure and evolution are obviously key ingredients.

In chapter 3 I presented an analysis of one of the leading equation of state projects, as well as some improvements aimed at broadening the range of applicability and increase the accuracy of the MHD equation of state. This work is equally aimed at the convection simulations and the general stellar structure and evolution problem.

These equation of state improvements are to be followed up by new calculations of opacities, as outlined in Sect. 3.4, which likewise has implications for both the convection simulations and stellar structure models.

With the progress in the evaluation of atomic physics, by far the most uncertain aspects of stellar structure models, are those involving dynamical processes which typically lead to mixing. As convection directly affects the structure of the star (not only through mixing) this is important dynamical process. This has been realized for almost a century, but the preferred formulation of the problem is still the rather simplified picture of the mixing-length formulation (MLT) (Böhm-Vitense 1953; Böhm-Vitense 1958). In Sect. 5.1.10 I explore some of the reasons why MLT, after all, does a pretty good job at describing convection, and I point out some of the differences between MLT and what we have learned from 3D simulations of convection. Since the MLT formulation has a (principal) free parameter, α, a first step towards a better description of convection in stellar models, is a calibration of α against the convection simulations, as undertaken in Sect. 5.1.10.

In order to be able to perform this calibration of α, everything other than the actual convection, had to be the same in the stellar structure models and the convection simulations. That means equation of state, opacities and the atmosphere. The problem of stellar atmospheres is computationally very expensive, and cannot be incorporated directly into stellar structure calculations. Instead, the results from atmosphere calculations can be used in the form of T-τ relations; temperature as function of optical depth, as confirmed in Sect. 5. T-τ relations are derived from the simulations and applied to the stellar structure models, to facilitate the calibration of α in Sect. 5.1.10. The T-τ relations from the simulations have also been fitted in the atmosphere parameters so that they can readily be used in stellar modeling.

One of the short-comings of conventional stellar atmosphere models is their re-

striction to 1D space, with some dynamical effects included after the fact, *e.g.*, micro- and macro-turbulent velocities. These atmosphere models also use the MLT for describing convection, but as the largest deviations between the MLT picture and the 3D simulations occur in the atmosphere, the structure of an atmosphere that incorporates MLT-type convection, is unlikely to resemble a real stellar atmosphere in any detail.

Using the combination of the α-fitting and the T-τ relations in stellar structure and evolution calculations, carries the promise of more reliable stellar models, at least in the solar neighborhood of the HR-diagram. The implications for stellar evolution will be studied in a future paper (Trampedach et al. 2004b).

5.1 T-τ relations from convection simulations

T-τ relations are normally used for describing the photospheric transition from optically thick to optically thin in stellar models. This is well justified, but the importance of the T-τ relationrelation as an upper boundary condition for stellar envelops seems not to have been fully appreciated. We assess the effects of employing often used assumptions about T-τ relations on stellar models and illustrate the interplay between atmospheric stratification and the depth of an outer convection zone. Convection in stellar structure models is often described by the mixing-length theory (MLT). We present calculations of T-τ relations based on 3D radiation-coupled hydrodynamical (RHD) simulations and give simple fits to our results for easy use in stellar structure calculations.

5.1.1 Introduction

The calculation of stellar atmospheres is so complex that it has formed its own sub-discipline. Most complications arise because radiative transfer in the transition from optically thick to optically thin is hard to treat in a simplified manner without losing essential features. To treat this region properly, the radiative transfer has to be solved for hundreds of thousands of wavelength points. This obviously renders atmosphere calculations time consuming and impractical to incorporate directly in stellar evolution codes.

A solution to this problem is to use the results of stellar atmosphere modeling (semi-empirical or fully theoretical) as upper boundary conditions for stellar struc-

ture models. Since T-τ relations can be derived from limb-darkening observations, the use of semi-empirical models based on such observations often has been considered the safest choice. Knowing pressure and opacity as functions of ϱ and T, and assuming hydrostatic equilibrium, the system of equations can be closed by the T-τ relation without having to solve the frequency dependent radiative transfer — *i.e.*, the stratification of the detailed atmosphere calculation can be recovered with a grey opacity, as described in Sect. 5.1.2. We proceed by giving a short overview of the 1D structure calculations in Sect. 5.1.3, where we also elaborate on the implementation of T-τ relations.

Theoretical T-τ relations from 1D stellar atmosphere models have been published in connection with, *e.g.*, the ATLAS (Kurucz 1992c; Kurucz 1995), the MARCS (Gustafsson et al. 1975; Asplund et al. 1997) and the NEXTGEN (Hauschildt et al. 1999a; Hauschildt et al. 1999b) grids of stellar atmospheres. These are grids in effective temperature, surface gravity and metallicity and dense enough that simple interpolation is safe. The level of sophistication is very impressive, the only weak point left, being the treatment of convection.

In late type stars the modeling of photospheres is further complicated by convection. Not only are the atmospheres no longer one-dimensional, but the fluctuations are also well outside the regime of linear perturbations. So far, the only way to deal with the combined problem of radiation-coupled convection in stellar photospheres, is to perform realistic radiation hydrodynamic (RHD) simulations. We describe such 3D convection simulations in Sect. 5.1.4 and go through the various ways of extracting the average structure from the simulations in Sect. 5.1.5. In Sect. 5.1.6, we

compare the results of our "high-precision" solar simulation with T-τ relations from the literature.

In Sect. 5.1.7, we present a single fitting formula for $T(\tau)$, which works well for all the simulations. We furthermore give a list of fits, linear in $\log T_{\rm eff}$ and $\log g_{\rm surf}$, of all the coefficients, for use in stellar structure calculations. We apply the T-τ relations, derived from the simulations, to stellar structure calculations in Sect. 5.1.9. We compare the effects of using some of the most common combinations of T-τ relations and opacities, and point out some of the often encountered inconsistencies. We also explore how changes to the physics in the atmosphere changes the depth of the outer convection zone.

This paper is the first in a series dedicated to the improvement of stellar structure and evolution calculations. These improvements are based on lessons learned from 3D radiation-coupled hydrodynamical simulations of convection in the atmospheres of a handful of solar-like stars. Here we present results on the radiative part of the mean-stratification of the simulations in the form of T-τ relations. Paper II (Trampedach et al. 2004a) deals with the convective part of the mean-stratification by calibrating the mixing-length and presenting results easy to implement in stellar structure codes. The radiative and the convective parts of the problem are strongly interdependent, as discussed in the two papers, but we also show that separating the two parts is possible and has a significant effect on stellar structure models. Paper III (Trampedach et al. 2004b) will address the consequences of applying the above improvements to stellar evolution calculations.

The effect of T-τ relations on stellar evolution, has also been studied by Chabrier

& Baraffe (1997b) for low-mass stars with solar composition. They argue that the use of T-τ relations imply grey radiative transfer in the atsmophere. From our analysis in Sect. 5.1.2 we show that this is not the case; a T-τ relation relation can fully describe a non-grey atmosphere, but the zeroth, Eq. 152, and first, Eq. 153, moments of the transfer equation are modified. These modifications imply the use of Rosseland opacities, also being the natural choice for the stellar modeler. Chabrier & Baraffe are rightfully concerned about the proper implementation and interpretation of the T-τ relation in the transition between radiative and convective zones—an issue which is often overlooked. We hope that our discussion in Sect. 5.1.2 below will clarify matters, and justify the use of T-τ relations, even in this region.

Ludwig et al. (1999) have performed a similar, but employing a completely independent method, calibration of the mixing-length based on 2D simulations of convection. Their T-τ relations are computed and implemented in a way similar to what we present here. Paper II provides further comparisons between the two methods and the results.

5.1.2 The Basis for T-τ relations

We describe the 1D, plane-parallel, radiative transfer in terms of the usual moments of the radiation field

$$I_\lambda^{(n)} = \tfrac{1}{2}\int_{-1}^{1} \mu^n I_\lambda(\mu)\mathrm{d}\mu \ , \tag{148}$$

where the intensity, I_λ, only depends on the angle with the surface normal, $\mu = \cos\theta$. Dependence on optical depth, τ, is implied throughout this section. Extension to the

3D case is dealt with in Sect. 5.1.5.

The first three moments are also called

$$J_\lambda = I_\lambda^{(0)}\,, \quad \frac{F_{\rm rad}}{4\pi} = H_\lambda = I_\lambda^{(1)} \;\text{ and }\; K_\lambda = I_\lambda^{(2)}\,. \tag{149}$$

The transfer equation is

$$\mu\frac{{\rm d}I_\lambda(\mu)}{{\rm d}\tau_\lambda} = I_\lambda(\mu) - S_\lambda\,, \tag{150}$$

where the source-function, S_λ, is isotropic.

The corresponding radiative heating (cooling when negative) is

$$Q_{{\rm rad},\lambda} = 4\pi\varrho\kappa_\lambda(J_\lambda - S_\lambda)\,, \tag{151}$$

where the 4π comes from the angular integration of an isotropic quantity and $Q_{\rm rad}$ is the extensive version (per volume) and $q_{\rm rad} = Q_{\rm rad}/\varrho$ is the intensive quantity. A solution in radiative equilibrium obviously obeys $Q_{\rm rad} = \int_0^\infty Q_{{\rm rad},\lambda}{\rm d}\lambda = 0$.

Grey Radiative Transfer

In a grey atmosphere, the opacity is independent of wavelength, and we can drop all the λ-subscripts. Integrating the transfer equation over angle then gives

$$\frac{{\rm d}H}{{\rm d}\tau} = \frac{1}{4\pi}\frac{{\rm d}F_{\rm rad}}{{\rm d}\tau} = J - S\,, \tag{152}$$

whereas the first moment of the transfer equation gives

$$\frac{\mathrm{d}K}{\mathrm{d}\tau} = H = \frac{F_{\mathrm{rad}}}{4\pi} = \frac{\sigma T_{\mathrm{eff}}^4}{4\pi}\left(1 - \frac{F_{\mathrm{conv}}}{F_{\mathrm{tot}}}\right) , \tag{153}$$

or

$$\Delta K = \frac{\sigma T_{\mathrm{eff}}^4}{4\pi}\left(\tau - \int_0^\tau \frac{F_{\mathrm{conv}}(\tau')}{F_{\mathrm{tot}}}\mathrm{d}\tau'\right) , \tag{154}$$

where the integral contains the convective effect. The convective flux is the sum of the enthalpy and the kinetic energy fluxes.

It turns out that we are only interested in $\Delta K(\tau) = K(\tau) - K(0)$, and are therefore not concerned with the constant, $K(0)$, from the integration of Eq. (153).

Assuming local thermodynamic equilibrium (LTE), as we do in both the simulations and the stellar structure calculations, we have $S = B = \sigma T^4/\pi$. Multiplying both sides of Eq. (154) by $4\pi S/(3\Delta K \sigma T_{\mathrm{eff}}^4)$ therefore results in the T-τ relation

$$\frac{4}{3}\left(\frac{T}{T_{\mathrm{eff}}}\right)^4 = \frac{S}{3\Delta K}\left[\tau - \int_0^\tau \frac{F_{\mathrm{conv}}(\tau')}{F_{\mathrm{tot}}}\mathrm{d}\tau'\right] . \tag{155}$$

The $\tau/\Delta K$-factor is convergent, since ΔK increase approximately linearly in τ and we can therefore describe finite temperatures. Using K instead of ΔK, would have introduced an extra term for the temperature at $\tau = 0$.

All subsequent references to the T-τ relation will only deal with the *radiative* part,

$$\frac{4}{3}\left(\frac{T}{T_{\mathrm{eff}}}\right)^4 = \frac{S}{3\Delta K}\tau , \tag{156}$$

unless otherwise noted.

Average Radiative Transfer

If, on the other hand, the opacity *does* depend on wavelength, integrating Eq. (153) over wavelength gives

$$\int_0^\infty \frac{1}{\varrho\kappa_\lambda}\frac{\mathrm{d}K_\lambda}{\mathrm{d}z}\mathrm{d}\lambda = H = \frac{F_{\mathrm{rad}}}{4\pi}\ , \tag{157}$$

where we substituted $\mathrm{d}\tau_\lambda = \varrho\kappa_\lambda \mathrm{d}z$. F_{rad} and H are just the results of direct integration over wavelength. As $J_\lambda \to S_\lambda$ and $K_\lambda \to \frac{1}{3}J_\lambda$ for $\tau_\lambda \to \infty$ and $S_\lambda = B_\lambda$ in LTE, Eq. (157) leads us to the usual definition of the *Rosseland opacity*

$$\frac{1}{\kappa_{\mathrm{Ross}}} = \frac{\int_0^\infty \frac{1}{\kappa_\lambda}\frac{\mathrm{d}B_\lambda}{\mathrm{d}T}\mathrm{d}\lambda}{\int_0^\infty \frac{\mathrm{d}B_\lambda}{\mathrm{d}T}\mathrm{d}\lambda}\ . \tag{158}$$

(We can interchange differentiation with respect to z and T as they are monotonic functions of each other.)

From this, we can now define

$$\frac{\mathrm{d}\tilde{K}}{\mathrm{d}\tau_{\mathrm{Ross}}} \equiv \kappa_{\mathrm{Ross}}\int_0^\infty \frac{1}{\kappa_\lambda}\frac{\mathrm{d}K_\lambda}{\mathrm{d}\tau_{\mathrm{Ross}}}\mathrm{d}\lambda = H = \frac{F_{\mathrm{rad}}}{4\pi}\ , \tag{159}$$

where $\mathrm{d}\tau_{\mathrm{Ross}} = \varrho\kappa_{\mathrm{Ross}}\mathrm{d}z$ defines the *Rosseland optical depth.* The tilde refers to quantities that are averaged over wavelength in a way that makes them obey the grey transfer equations, Eqs. (152) and (153). In a similar way, the zeroth moment

of the transfer equation gives

$$\frac{\mathrm{d}\tilde{H}}{\mathrm{d}\tau_{\mathrm{Ross}}} \equiv \kappa_{\mathrm{Ross}} \int_0^\infty \frac{1}{\kappa_\lambda} \frac{\mathrm{d}H_\lambda}{\mathrm{d}\tau_{\mathrm{Ross}}} \mathrm{d}\lambda = J - S \ , \tag{160}$$

where we again substitute $S = B$.

We see that the tight link between the zeroth and first moments of the averaged radiative transfer is broken as $H \neq \tilde{H}$ in general. We do, however, obtain the same expression for the T-τ relation, Eq. (155), by substituting $\tilde{K}$ and τ_{Ross}.

With the radiative temperature being given by Eq. (156), and the temperature from the simulations by Eq. (155), we can reduce the temperatures from the simulations to the purely radiative ones by

$$T_{\mathrm{rad}} = T\tau^{1/4} \left[\tau - \int_0^\tau \frac{F_{\mathrm{conv}}(\tau')}{F_{\mathrm{tot}}} \mathrm{d}\tau' \right]^{-1/4} \ . \tag{161}$$

This is the stratification in the case of no convective flux. Deriving $T_{\mathrm{rad}}(\tau)$ from the simulations does, however, retain secondary convective effects, ie, the radiative equilibrium, as influenced by convection. As mentioned earlier, T_{rad} is the temperature to be used in T-τ relations.

5.1.3 The 1D-envelopes

The T-τ experiments have been performed on models of stellar envelopes (Christensen-Dalsgaard & Frandsen 1983), that each cover the range from a relative radius of $r/R = 0.05$ and out to an optical depth of $\tau = 10^{-4}$.

All time dependent and composition altering processes, *e.g.*, nuclear reactions, diffusion and settling of helium and metals, have been left out. This renders the envelopes functions of the atmospheric parameters, $T_{\rm eff}$ and $g_{\rm surf}$ (and composition) only, but it also rules out any abundance gradients. Helium and metals slowly dropping out of the convection zone build up an abundance gradient, just below the convection zone, which is counteracted by diffusion. As diffusion and settling only generate abundance gradients below the convection zone, our results on the T-τ relation and the α-calibration should be independent of these processes, whereas the depth of the convection zone might be affected slightly. Radiative levitation of high-opacity elements, on the other hand, would have the largest effect in the photosphere and the change in composition would alter the opacity and equation of state so as to change the efficiency of convection. From the 3D simulations, however, we know that the convective overshoot sustain velocities-fields, at least out to $\tau \simeq 10^{-4}$ that would immediately wipe-out any chemical gradients in the atmospheres of the stars we have explored here.

For the envelopes, we have used the same equation of state (EOS), chemical composition, and, for $T \lesssim 10^4\,\mathrm{K}$, the same opacities as for the simulations (*cf.* Sect. 5.1.4). For higher temperatures, we used the OPAL opacities (Rogers & Iglesias 1992a). The difference between the two opacities is generally small at this temperature, and the transition is smoothed and always takes place in the adiabatic part of the convection zone, minimizing the impact on the structure of the model.

Convection is treated using the standard MLT as described in Böhm-Vitense

(1958), using the standard mixing length

$$l = \alpha H_P \tag{162}$$

and form factors $y = \frac{1}{3}$ and $\nu = 8$.

The T-τ relations are supplied through Eq. (168) (See Sect. 5.1.7), and different choices for the coefficients then constitute the various cases listed in Tab. 7 below.

Implementation of the T-τ relation

The *Hopf function*, $q(\tau)$, introduced by Henyey et al. (1965), is part of the T-τ relation

$$\frac{4}{3}\left(\frac{T}{T_{\rm eff}}\right)^4 = q(\tau) + \tau + q_{\rm conv}(\tau) \ . \tag{163}$$

In the spirit of Eq. (155) we distinguish between the convective Hopf function, $q_{\rm conv}(\tau)$, which is the integral from Eq. (155), and the purely radiative Hopf function, $q(\tau)$. The radiative part is convergent, $q(\tau) \to q_\infty$ for $\tau \to \infty$, and recovers the diffusion approximation.

In deriving the T-τ relation in Sect. 5.1.2 we make the transformation from actual to radiative T-τ relation by changing T, as shown by Eq. (163). In the envelope calculations we need to re-introduce convection in the T-τ relation, this time described by MLT. This is done with the inverse transformation, which is accomplished through a modification of the optical depth

$$\mathrm{d}\hat{\tau} = f_\kappa \mathrm{d}\tau \ , \tag{164}$$

so that

$$q(\hat{\tau}) + \hat{\tau} = q(\tau) + \tau + q_{\rm conv}(\tau) \ . \tag{165}$$

Differentiating both sides of Eq. (165) with respect to τ, we get

$$f_\kappa = \frac{q'(\tau) + 1 + q'_{\rm conv}(\tau)}{q'(\hat{\tau}) + 1} \ , \tag{166}$$

where primes indicate differentiation with respect to the argument and $\hat{\tau}$ is found from solving Eq. (165).

Employing hydrostatic equilibrium and, as usual, defining the radiative gradient as the gradient that would be caused by radiative transport of energy alone, *i.e.*, assuming that T is given by $q(\tau) + \tau$, we find

$$\nabla_{\rm rad} \equiv \left(\frac{\partial \ln P}{\partial \ln T}\right)_{\rm rad} = \frac{\kappa p}{g} \frac{3F_{\rm tot}}{16\sigma T^4} (1 + q') \ . \tag{167}$$

The actual gradient, ∇, can similarly be found by using Eq. (165) and the transformation to $\hat{\tau}$, resulting in $f_\kappa = \nabla / \nabla_{\rm rad}$.

With these relations the T-τ relation can be used throughout the stellar envelope model, without the (common) artificial transition between atmosphere and interior.

5.1.4 The 3D-simulations

The fully compressible, transmitting boundary, RHD simulations are described by Nordlund & Stein (1990; 1989). Since the matching to 1D envelopes demands a high degree of consistency between the simulations and the envelopes, we found

it necessary to bring the micro-physics up to the same level as that used for the envelopes. Direct comparison to observations of the Sun also necessitated an update. We therefore revised most of the opacity sources and added a few more sources, as described in detail in Trampedach (1997). The line opacity is supplied by the opacity distribution functions (ODFs) of Kurucz (1992a; 1992b), and the EOS is changed to the Mihalas-Hummer-Däppen (MHD) EOS (Hummer & Mihalas 1988; Däppen et al. 1988).

Table 7. Parameters and derived convection zone depths for the seven simulations.

name	Star A	α Cen B	Sun	α Cen A	Star B	η Boo	Procyon
Spectral class	M 5 IV	K 1 V	G 2 V	G 2 V	F 8 V	G 0 IV	F 5 IV-V
$T_{\rm eff}$	4851 K	5362 K	5801 K	5768 K	6167 K	6023 K	6470 K
$g_{\rm surf}/[{\rm cm^2\,s^{-1}}]$	$1.243{\cdot}10^4$	$3.604{\cdot}10^4$	$2.740{\cdot}10^4$	$1.970{\cdot}10^4$	$1.084{\cdot}10^4$	$5.668{\cdot}10^3$	$1.084{\cdot}10^4$
$M/M_\odot$	0.600	0.900	1.000	1.085	1.240	1.630	1.750
α	1.8705	1.8313	1.8171	1.8032	1.7360	1.7383	1.7193
$d_{\rm CZ}$	0.5600	0.3063	0.2861	0.3070	0.1966	0.2087	0.1035
$d_{\rm CZ}$ solar	0.5616	0.3085	0.2861	0.3057	0.1870	0.1927	0.0925
$d_{\rm CZ}$ 5000 Å	0.5505	0.2971	0.2647	0.2795	0.1552	0.1618	0.0639
$d_{\rm CZ}$ HSRA	0.5498	0.3016	0.2705	0.2866	0.1579	0.1623	0.0692

We have performed simulations for seven sets of atmospheric parameters, five of which correspond roughly to actual stars, as listed in Tab. 7. The Star A-simulation was added to get a better coverage in the $T_{\rm eff}/g_{\rm surf}$-plane and Star B was a simulation of Procyon that turned out too cool (they therefore have the same $g_{\rm surf}$).

Mostly for historical reasons, we used a hydrogen fraction by mass of $X = 70.2960\,\%$ and a metal fraction by mass, $Z = 1.78785\,\%$. Each of the simulations was performed on a $50 \times 50 \times 82$-point grid and covers about 4–6 granules horizontally and 13 pressure-scale-heights vertically, with 20% being above $\langle T \rangle = T_{\rm eff}$. After

relaxation to a quasi-stationary state, we calculated mean models as described in Sect. 5.1.5.

5.1.5 Averaging procedures

We evaluated T-τ relations for both the Rosseland optical depth, $\tau_{\rm Ross}$, and the 5000 Å monochromatic optical depth, τ_{5000}, each with three different averaging procedures.

The convective fluctuations in density and especially temperature are so large that the opacity and the EOS (*e.g.*, gas pressure, $P_{\rm g}$) are non-linear in the fluctuations, which has the consequence that $\langle P_{\rm g}\rangle \neq P_{\rm g}(\langle\varrho\rangle,\langle T\rangle)$. This means that the average gas pressure is, in general, not related to the average density and temperature through the EOS. The relative difference amounts to about 5% in the solar photosphere. This effect is much larger for the opacity where the relative difference reaches more than 90%. This has led us to evaluate the three averaging procedures compared in Fig. 15, and detailed below.

Case a): Calculate optical depth-averaged models by interpolating temperature, T, onto iso-τ surfaces, equidistant in $\log_{10}\tau$, and averaging over these surfaces. These τ-averages were then subjected to temporal averaging and we denote this procedure $\langle\ldots\rangle_\tau$.

The radial p-modes, which are excited in the simulations, are to a large extent filtered out by this method because of the dependence of opacity on density and temperature. With increased temperature and density, the opacity and optical depth increase, moving the τ-scale outwards with respect to the z-scale, in much the same

way as the column mass scale. The temporal RMS-fluctuations of gas-pressure on a

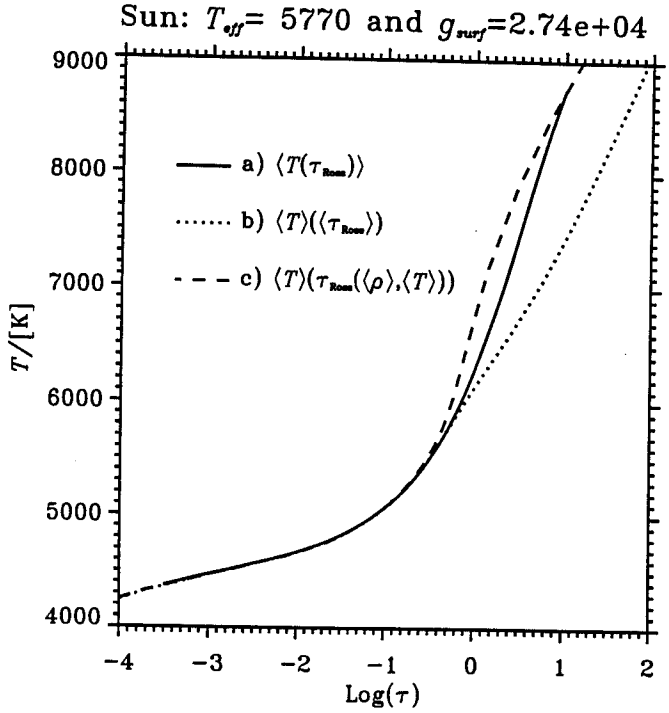

Fig. 15. The effect of various averaging techniques applied to a solar simulation (See text for details). Notice how cases a) and b) follow closely in the atmosphere down to $\langle T \rangle = T_{\rm eff}$, at $\log_{10} \tau \simeq -0.2$.

τ-scale are about 10 times smaller than on a fixed height-scale. This effect is also clearly seen in the results of Georgobiani et al. (2003a), where the p-modes excited in a solar simulation are very prominent in temperature, sampled at a fixed height, but almost vanish when sampled on the undulated iso-τ surface.

This averaging procedure is motivated by the form of the radiative transfer equation, Eq. (150). Since τ is the only quantity entering the radiative transfer equation in a non-linear way (a division), this is also the only quantity that cannot merely be replaced by its horizontal average. We therefore recommend this averaging method for use in conventional 1D stellar models, and it is the method used for the rest of our analysis. This averaging procedure corresponds to observations of the

"radial" or disk-center $T(\tau)$ in the sense that it is the average of $T(\tau)$ along radial rays. Also, looking at disk center, it is not possible to "observe" the height-scale—only the τ-scale.

Case b): Calculate geometrically averaged models by mapping the horizontal averages onto a column mass scale and performing the temporal averaging on this scale instead of on a direct spatial scale. This approach filters out the main effects of the p-modes excited in the simulations. We refer to this procedure as *Lagrangian averaging*, $\langle \ldots \rangle_{\rm L}$.

This Lagrangian averaged T as a function of the Lagrangian averaged τ corresponds in a sense to limb observations, observing the Sun "horizontally", instead of "radially" on an optical depth-scale. Real limb observations would also contain a **case a)** component due to the Sun's sphericity. As noted above, this method is not compatible with the radiative transfer equation.

Case c) Calculate $\langle T \rangle_{\rm L}$ as function of a τ, based on integration of $\kappa(\langle T \rangle_{\rm L}, \langle \varrho \rangle_{\rm L}) \neq \langle \kappa \rangle$. The non-linearity of the opacity is taken into account by this method. If $P_{\rm turb}$ and the non-linear effects on $P_{\rm g}$ were known, the correct ϱ, T, P-structure could be recovered with such a T-τ relation. This method mixes the convective and optical parts of the problem, though, making it more difficult to improve their treatment in stellar structure calculations in a consistent way.

From Fig. 15 we see that the T-τ relation can be derived fairly unambiguously from limb-darkening observations, for $\langle T \rangle \lesssim T_{\rm eff}$. There the inhomogeneities are small enough for the opacity to be linear on the scale of the fluctuations, rendering the three averaging procedures equivalent. At greater depth this is no longer the case as the

inefficient convection at the top of the convection zone causes large and non-linear fluctuations, splitting case a) and b) apart. The T-τ relation still has a significant effect on the envelope model at these depths, though, requiring us to make a specific choice. Based on Sect. 5.1.2 we choose case a), as also advocated by Ludwig et al. (1999).

5.1.6 The solar T-τ relation

Apart from the simulations of the seven stars presented in Tab. 7, we also made a simulation for direct comparison with solar observations. This simulation has a slightly different composition: $Y_\odot = 0.245$ in accordance with helioseismology (Basu & Antia 1995), and $Z_\odot/X_\odot = 0.0245$ in agreement with meteoritic and solar photospheric metal to hydrogen ratios (Grevesse & Noels 1992). This ratio results in the hydrogen mass-fraction, $X = 73.6945\%$ and the helium-hydrogen number ratio, He/H=0.0837, instead of the often assumed He/H$\simeq$ 0.1. The latter ratio is what we, for historical reasons, used for the seven other simulations, listed in Tab. 7.

The Z/X ratio is reduced by about 4 % from the other simulations, primarily decreasing the line-blocking by metals, resulting in a decreased q. Helium, being an inert element, contributes little to the opacity. Its own opacity is very small in the solar atmosphere, and the high ionization potential means that no electrons are donated for the formation of H^--ions, which is the most important source of continuum opacity in the Sun. The larger X (lower Y) therefore leads to increased opacity and the lower Z leads to less line-blocking. These changes to the composition

also alter the mean molecular weight, μ, which enters both in Eq. (177) for the convective flux and in the hydrostatic equilibrium through its effect on the pressure.

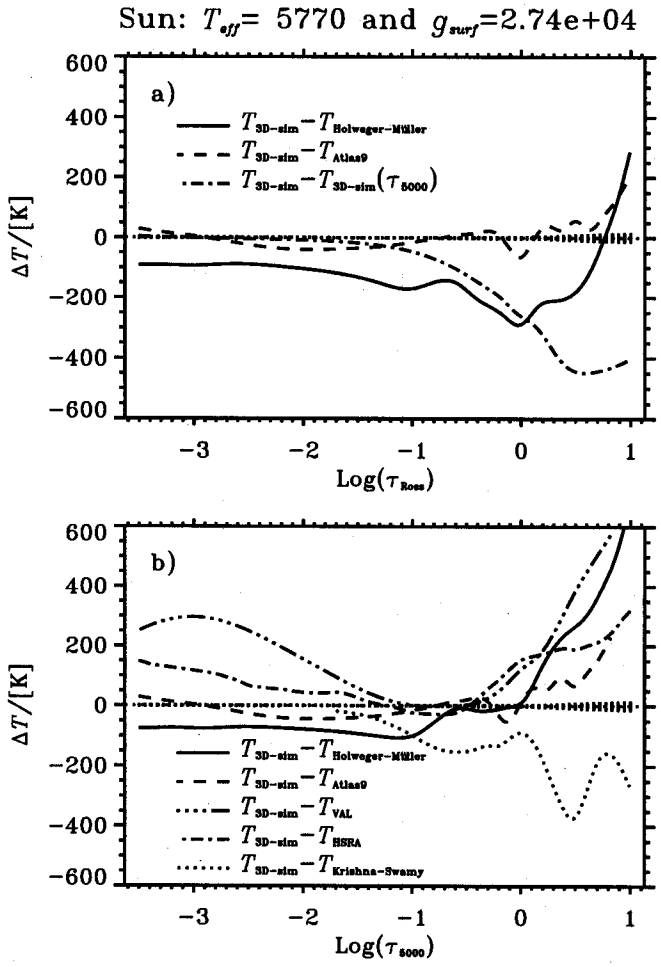

Fig. 16. Comparison of the T-τ relation from the simulation, with some often used solar T-τ relations. a): The difference in Rosseland T-τ relations between the simulation and an Atlas9 atmosphere model (Kurucz 1993; Castelli et al. 1997). b): Differences, on a τ_{5000}-scale, between the simulation and an Atlas9 model, and four semi-empirical atmosphere models: The model by Holweger & Müller (1974), the classical fit by Krishna Swamy (1966a; 1966b), the HSRA model (Gingerich et al. 1971) and the VAL model (Vernezza et al. 1981).

The effective temperature of the solar simulation is $T_{\rm eff} = 5\,777 \pm 9\,{\rm K}$, which is in excellent agreement with irradiance observations (Willson & Hudson 1988): $5\,777 \pm 2.5\,{\rm K}$. The horizontal spatial resolution of this simulation is twice that of the seven other simulations ie, $100 \times 100 \times 82$ points.

We compare the resulting T-τ relations with various 1D models, in Fig. 16. Panel a) shows temperature differences on the $\tau_{\rm Ross}$-scale and panel b) is for the τ_{5000}-scale. The vertically hatched area around the zero-line (in both panels) shows the temporal RMS-scatter of the T-τ relation of the simulation, confirming that all the differences are statistically significant. Panel a) also shows the difference between the temperature measured on the two τ-scales for the simulation (dot-dashed curve), the sign of which means that we can see deeper into the Sun at 5000 Å than on (a Rosseland) average, and therefore that the Rosseland opacity is larger than the 5000 Å opacity.

The past decade or so of work on compiling and computing line-data for atoms and molecules has added a lot of line-opacity in the UV, which has increased the Rosseland opacity with respect to the 5000 Å opacity. This in turn has increased the difference between $\tau_{\rm Ross}$ and τ_{5000}. This is clearly expressed in the 200 K difference at $\tau \simeq \frac{2}{3}$. This difference is two times larger than the corresponding differences among modern atmosphere models (*cf.* Fig. 16b), so it is no longer justified to assume the two τ-scales to be equal.

For stellar structure calculations, it has been common practice to use a T-τ_{5000} relation combined with a Rosseland opacity. With the current opacities and today's demand for accuracy, this no longer seems a valid approximation and we recommend not using it.

For the theoretical Atlas9 atmosphere models (Kurucz 1993), both monochromatic and Rosseland T-τ relations can be obtained, illustrated as the dashed line in both panels of Fig. 16. The peculiar wiggles in these curves are features from the

Atlas9 model. Using the "overshoot"-option, later rejected by Castelli et al. (1997), these wiggles combine to a larger but smoother dip, compared to the simulation. The rather close agreement in the radiative part of the atmosphere is expected, since the same line-opacities were used, and since the convective fluctuations have only a small effect on the averaged T-τ relation above the convection zone (*i.e.*, all averaging methods give the same results, *cf.* Fig. 15).

The model by Holweger & Müller (1974) presented in Fig. 16 (solid line) is about 100 K warmer than the simulation above the photosphere, on both τ-scales. For this model the T-difference between the two τ-scales is, however, less than 60 K, so below $\tau \simeq 0.5$ the behavior in the two panels differ by the $(\tau_{\rm Ross} - \tau_{5000})$-difference for the simulation. The Holweger-Müller model is hotter by up to 300 K on the $\tau_{\rm Ross}$-scale, but is very similar in the photosphere and getting increasingly cooler with depth on the τ_{5000}-scale.

The two other semi-empirical atmosphere models presented in Fig. 16, VAL C for the quiet Sun (Vernezza et al. 1981) and the Harvard-Smithsonian solar reference atmosphere (HSRA) (Gingerich et al. 1971), differ significantly and essentially in the same way from the simulation results. High in the atmosphere, the differences can most likely be attributed to non-LTE effects, heating from a hot corona and possibly also magnetic fields in the atmosphere, none of which is included in the simulations. It could, however, also be due to misinterpretation of temperature proxies. Since the UV Planck-function, ionization balances and level populations in atoms and ions involve exponential terms in T, the temperature derived from spatial and temporal averaged quantities will be higher than the correspondingly averaged temperature,

as shown by Carlsson & Stein (1995) in the dynamic 1D case. This is irrespective of our finding from Fig. 15, that the convective fluctuations have little effect on the average T-τ relation above the photosphere. Individual lines and the UV brightness can still behave non-linearly.

The immediate outcome of this would be larger T, but as the opacity increases strongly with T, the τ-scale could easily change enough so as to result in a lower T-τ relation than the actual, as we find in Fig. 15.

The differences between the HSRA, the Holweger-Müller and the VAL models may be due to temporal variations in the solar atmosphere between the observations, ten years worth of improvement in the handling of non-LTE effects, as well as differences in the opacities used for the τ-scale.

At intermediate optical depths, from $\tau \simeq 0.1$ down to $\langle T \rangle = T_{\rm eff}$, the agreement between both theoretical and semi-empirical atmospheres and the simulation is very good. Differences are also smaller than the difference between the 5000 Å and the Rosseland T-τ relation from the simulation. This agreement is reassuring, as all four approaches to the solar atmosphere should be about equally valid in this region: 3D-effects are small, the velocity-field only contributes a small turbulent pressure to the hydrostatic equilibrium, the convective flux is less than a percent of the total flux, non-LTE effects are small and we are far away from the hot corona.

With the onset of convection, the T-τ relations in Fig. 16 diverge, with the various 1D-models, sharing the MLT-formulation of convection, all differing from the simulation in more or less the same manner. Below $\langle T \rangle = T_{\rm eff}$, 3D-effects become important and the turbulent pressure contributes up to 14% of the total pressure,

rendering the simulation the best choice for an atmosphere model. The validity of the simulations in this region has to be assessed from comparisons with more direct observations of the Sun, *e.g.*, measurements of the flux-spectra, limb-darkening and line-profiles. This serves to stress that T-τ relations from semi-empirical models are not observations and are only unambiguous with respect to the underlying limb-darkening observations above the point where $\langle T \rangle = T_{\rm eff}$. This, of course, rests on the assumption that we have complete knowledge of the opacities in the atmosphere, which, despite the last decades progress (Kurucz 1992b), still seems a rather unrealistic assumption (Kurucz 1992e; Lester 1996).

The last T-τ relation presented in Fig. 16 is the one by Krishna Swamy (1966a; 1966b), which is still used as an upper boundary in some stellar model codes. It is interesting to note that the behavior below the photosphere is opposite that of the more modern T-τ relations.

5.1.7 Fitting formulas

T-τ relations for seven individual stars are of rather limited value when concerned with stellar structure calculations in general, unless there is a way to interpolate between these individual stars.

We have therefore fitted the individual T-τ relations, through the corresponding Hopf functions, Eq. (163), to expressions of the form

$$q(\tau) = q_1 + q_2 e^{-(q_3\tau)^{q_4}} (\log\tau - q_5) + \eta\,[q_6 - q_7\eta] \ , \qquad (168)$$

where

$$\eta = \frac{-q_{\rm conv}(\tau)}{q(\tau) + \tau + q_{\rm conv}(\tau)} \tag{169}$$

is the negative ratio of convective to total Hopf function [*cf.* Eqs. (155) and (163)]. This definition makes η increase with increasing convective ratio of the total flux.

The first term serves to give the limit of optical deep layers with radiative energy transport. At large optical depths, the Rosseland opacity suffices to describe the transport of radiation and the stratification is therefore that of a grey atmosphere, provided all the energy is transported by radiation. In terms of the Hopf function, $q(\tau)$, this means that $q(\tau) \rightarrow q_\infty$, mimicked by the $q_1 + \tau$ term in Eq. (168).

In optically thin layers, the transport of radiation can no longer be described by a single opacity, and the T-τ relation deviates from the grey case. The $q_2(\log_{10}\tau - q_5)$ part of the second term provides the asymptotic behavior for $\tau \rightarrow 0$, and the $e^{-(q_3\tau)^{q_4}}$-factor interpolates smoothly between the two cases. None of the simulations show any sign of leveling off to an isothermal atmosphere, which must be due to the cooling by very strong lines, extending further out than the simulation domains. Therefore, we have not included an isothermal term, as is normally done. We still, however, encourage the use of an isothermal boundary condition at $\tau = 0$ in stellar structure models. Proper non-LTE calculations would most likely produce temperature minima for all seven atmospheres, which would be closer to the photosphere than the transition to an isothermal atmosphere, but the global influence on stellar structure models will be small.

If some of the energy is transported by convection, the T-τ relation will be

cooler than the grey case at large optical depth, which is described by the last term in Eq. (168). This term therefore describes the transition from radiative to convective energy transport. It should not be used with normal stellar models, as these often assume a purely radiative T-τ relation (set $q_6 = q_7 = 0$ in that case), and incorporate convection subsequently.

It might seem natural to use the same method as in the envelope models, and use the effective optical depth, $\hat{\tau}$, as given by Eq. (164). This, however, turns out to underestimate the effect of the transition to convection. The reason is that, as pointed out by Nordlund & Stein (2000), the high temperature sensitivity of the opacity hides the warm up-flows (granules) from our view, thereby cooling the T-τ relation in the convection zone. This is a pure 3D effect due to the large in-homogeneities at the top of the convection zone, which are maintained by the sharp increase in opacity with temperature. The horizontal average of the temperature in the simulation is therefore higher than in the 1D-models, although it is lower on a τ-scale. That this is actually the case for the Sun has been supported by comparison with helioseismology (Rosenthal et al. 1999). In 1D models, the η-terms should be considered part of $q_{\rm conv}$. Whether they could be included with η calculated from the 1D fluxes, without compromising consistency, is not resolved.

5.1.8 Results and Discussion

The τ- and time-averaged temperatures for each of the simulations were fitted to Eq. (168) with standard deviations of 3–7 K (except for Procyon which could not be

Table 8. Coefficients for Eq. (170).

n	$a_{n\odot}$	a_{n1}	a_{n2}	$\mathrm{d}a_{n\odot}/\mathrm{d}Y$
1	0.87029	-0.78450	0.17643	0.00256
2	-1.14200	-0.24250	0.06275	-2.28313
3	0.44612	-0.94208	-0.70312	4.71555
4	0.75131	-3.25925	0.21293	-3.29934
5	2.38410	-11.25957	1.44532	33.49655
6	1.30317	-82.75698	5.98615	2.66277
7	1.65473	3.80075	-0.68706	1.86574

fitted to better than 14 K—we comment on this below), yielding the coefficients $q_{n,\mathrm{fit}}$. Each of these coefficients were then fitted to expressions

$$f_n = a_{n\odot} + a_{n1} \log \frac{T_{\mathrm{eff}}}{T_{\mathrm{eff},\odot}} + a_{n2} \log \frac{g_{\mathrm{surf}}}{g_{\mathrm{surf},\odot}} + \frac{\mathrm{d}a_{n\odot}}{\mathrm{d}Y}(Y - Y_\odot) \tag{170}$$

where the f_n's are related to the coefficients in Eq. (168) through

$$f_n = \begin{cases} q_{n,\mathrm{fit}} & \text{for } n = 1, 4, 5, 6 \\ \log q_{n,\mathrm{fit}} & \text{for } n = 2, 3, 7\ . \end{cases} \tag{171}$$

The numerical values of the coefficients are given in Tab. 8, and the standard deviation between the actual T-τ relations and the global fit is 10 K. The relative deviations are everywhere less than 40 K (*cf.* Fig. 17).

With 10 parameters, it is not trivial to make unambiguous fits to Eq. (168). A lot of effort has therefore gone into splitting degeneracies in parameter-space. We furthermore performed the fitting in two different ways: first by fitting the individual T-τ relations and then fitting the resulting 70 parameters to Eq. (170), and second by

fitting the T-τ relations directly from Eq. (170), *i.e.*, making global fits that assume the f_n's to be linear in $T_{\rm eff}$ and $g_{\rm surf}$. We iterated between the two methods, using the results from the first method in the second method and vice versa, until the two sets of results converged. We used four iterations. The accuracy of the fits is illustrated in Fig. 17, from which we see that the deviation from the actual T-τ relations lies mostly within the shaded area of the temporal RMS-fluctuations. Comparing with Fig. 16 we see that the deviations are smaller than the differences between the current range of solar atmosphere models and smaller than the differences between the T-τ relations from the seven simulations, as shown in Fig. 21.

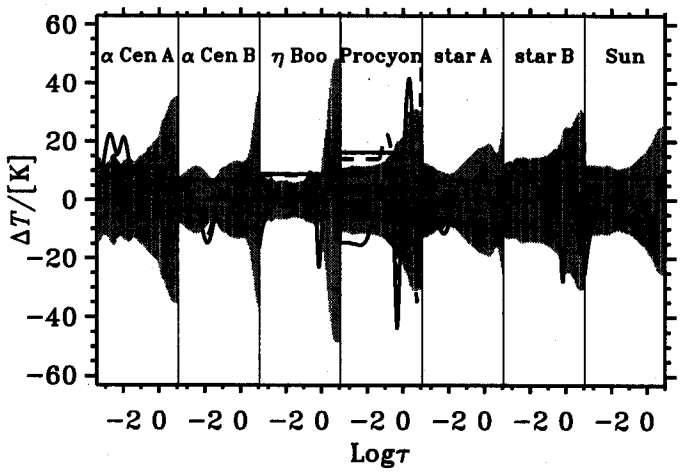

Fig. 17. Plot of the differences between the actual T-τ relations and the global fit (solid line) and the individual fits (dashed line). The horizontal solid and dashed lines are the corresponding RMS deviations from the fits. The shaded areas show the RMS of the temporal variation of the temperature.

From Fig. 17 we notice that Procyon is the worst fit. Allowing for a change in position and slope of the zero-line, we see that the main-component of the disagreement, is a sharp dip at τ slightly smaller than one. Looking at the panels for η Boo and Star B, we notice similar features, although less pronounced. In an earlier paper

(Trampedach et al. 1998), we presented a fitting formulae that also contained a negative Gaussian in τ. This expression was very good at fitting the above mentioned features, and brought down the RMS deviations to below 8 K, for the individual fits. It proved difficult, however, to parameterize the coefficients for the Gaussian in $T_{\rm eff}$ and $g_{\rm surf}$ in a way that both fit the simulations and resulted in physically plausible T-τ relations outside the immediate $T_{\rm eff}/g_{\rm surf}$-range of the simulations. We have therefore abandoned the Gaussian-term in the present work, and obtain improved global fits and a more widely applicable fit.

The coefficients of the global and the individual fits of the last iteration are compared in Fig. 18. The coefficients listed in Tab. 8 are the results of the last global fit.

The coefficients in Tab. 8 are based on the seven simulations with $X = 70.2960\,\%$ and $Z = 1.78785\,\%$. Assuming that a different composition offsets all the coefficients independently of $T_{\rm eff}$ and $g_{\rm surf}$, the $a_{n\odot}$'s have been changed to correspond to the solar simulation of Sect. 5.1.6 with the more modern abundances $X = 73.6945\%$ and $Z = 1.8055\%$.

The $\mathrm{d}q_i/\mathrm{d}Y$-term in Eq. (170) is derived from this difference in composition and is therefore only valid for helium changes accompanied by the rather unusual metallicity change, $Z - Z_\odot = -(Y - Y_\odot)/193.6$. This probably proves less useful, but, nonetheless, gives an idea of the changes with composition. Changes along more normal composition-change vectors would of course be very illuminating, but is beyond the scope of the present paper.

Notice that our fitting expression, Eq. (168) differ from that presented in Trampedach

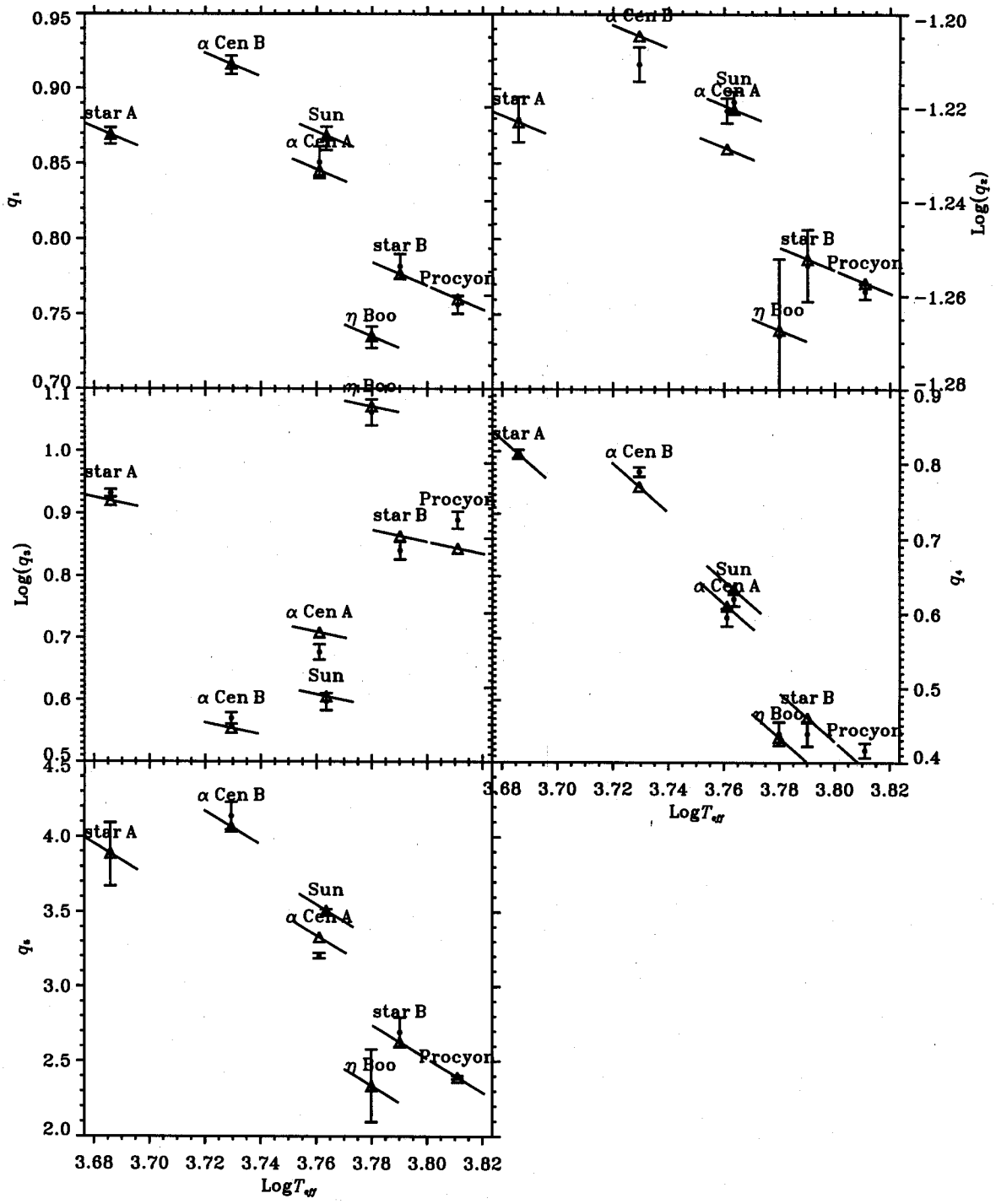

Fig. 18. Plot comparing the global (triangles) and individually (filled circles with error-bars) fit parameters for the T-τ relation-fits. The line segments show the $\log_{10}T$ gradient of the global fits. The error bars are the RMS-scatter from T-τ relation fits to single time-steps of the simulations.

et al. (1998) in a number of ways. First, as mentioned above, we have abandoned the Gaussian term in order to improve the global fits and making applicable in a wider $T_{\rm eff}/g_{\rm surf}$-range. Second, we have changed the formulation of the transition from optically thick to thin, to make the coefficients more linearly independent, and third, we have improved the separation of the convective effect on the T-τ relation (the last term in Eq. (168)). The standard deviations of the old fits were in most cases larger than those for the present fits.

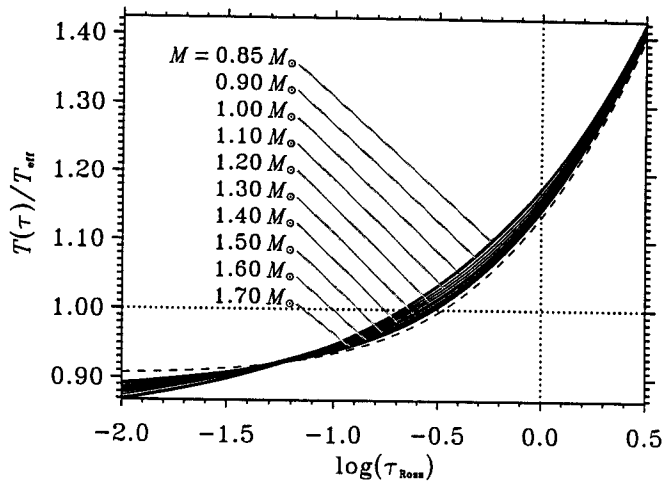

Fig. 19. The change of the T-τ relation with stellar mass, on the zero-age main-sequence. The horizontal dotted line indicates the effective temperature, and the vertical dotted line, optical depth unity. The dashed line shows the grey atmosphere.

In Fig. 19 we present the behavior of the T-τ relation with stellar mass on the zero-age main-sequence (ZAMS). The atmospheric parameters for the ZAMS were derived from the stellar structure models by (), which are also shown in Figs. 1 and 3 in Paper II. The higher mass stars have steeper T-τ relations in the photosphere, but they also have a larger curvature, making them shallower further out, as compared to the low-mass stars. The low-mass and higher mass T-τ relations, cross at $\tau \simeq 0.05$.

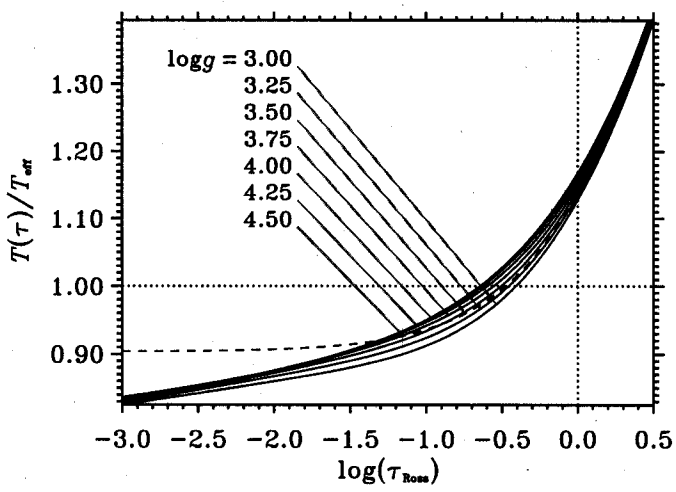

Fig. 20. The change of the T-τ relation with gravity, for fixed, solar $T_{\rm eff} = 5777\,{\rm K}$. The horizontal dotted line indicates the effective temperature, and the vertical dotted line, optical depth unity. The dashed line shows the grey atmosphere.

Fig. 20 illustrates the gravity dependence of the T-τ relation. As we go to lower gravity, the T-τ relation gets steeper in the photosphere and shallower further out—a similar effect as when going towards higher masses on the ZAMS.

In both Figs. 19 and 20 we also show the atmosphere with a grey opacity, *i.e.*, $\frac{4}{3}(T/T_{\rm eff})^4 = \frac{2}{3} + \tau$ (dashed curves). We see that the T-τ relation approaches the grey case, when we go to larger masses on the ZAMS. This is consistent with hotter stars having fewer spectral lines. The gravity sequence in Fig. 20 is a little more complicated. The steady decline of temperature in the high atmosphere, irrespective of gravity, is a sign of strong spectral lines that decouple (have monochromatic $\tau\lambda \simeq 1$) very high in the atmosphere. Explaining the behaviour at intermediate optical depth, in terms of radiative effects alone, is not possible.

Comparing the gravity sequence in Fig. 20 with 1D atmosphere models (Asplund 2003, private communications), we see rather large differences. In 1D the change with

gravity is more than a magnitude smaller than in Fig. 20. This might be due to the factor of five extrapolation of the gravity, beyond the range of the seven simulations. Of the five parameters, $q_1 - q_5$, for the radiative T-τ relation, only q_2 and q_3 have their *logarithms* fitted linearly to $\log T_{\rm eff}$ and $\log g$. At closer inspection, q_2 is increasing with g and is therefore bounded at small g by 0 and around the ZAMS the fit is guided by the simulations. The other parameter, q_3, is decreasing with g and therefore unbound towards the giants. The difference between fitting $\log q_3$ and q_3 itself, is less than a factor of two at $\log g$=3.0, so even with this large an extrapolation, the result is not diverging. We keep the logarithmic version, since we need q_3 to be positive definit.

The fit in the gravity-direction is mostly guided by the η Boo-simulation, having the lowest gravity and being only 220 K hotter. The fit at the gravity of η Boo, but solar $T_{\rm eff}$, is indeed very close to η Boo's T-τ relation. The main difference between the two simulations is the much stronger convection in η Boo; The turbulent- to total-pressure ratio is about 20% in the photosphere of the η Boo-simulation and only about 12% in the solar simulation.

As pointed out by Asplund et al. (1999), in realistic, convective stellar atmospheres the radiative heating and cooling is competing with the adiabatic cooling of rising plasma, expanding from the large density gradient in the atmosphere. The adiabatic stratification is typically more than 1000 K cooler than the radiative equilibrium solution. A stratification in-between these two extremes, will therefore experience radiative heating and convective cooling. From Eq. (151) for the radiative heating, we see that a larger Planck-mean opacity and a larger density results in more efficient radiative heating. In stars of lower gravity the density will be lower,

and the (per mass) opacity red-ward of the Balmer jump will be lower, due to fewer free electrons (from H-ionization) and hence, fewer H^--ions. On the other hand, the convective velocities, overshooting into the stably stratified layers, are larger and the adiabatic cooling therefore more efficient. All in all, three effects (density, opacity and velocities) work in the same direction, cooling the atmospheres of stars with lower gravity.

With each heating mechanism there is an associated flux F, related to the heating rate Q through

$$Q = \frac{\mathrm{d}F}{\mathrm{d}z} \,, \tag{172}$$

cf., Eqs. (151) and (152).

The two processes, radiation and convection, produce heating which is proportional to the deviation from their respective equilibria stratifications, *i.e.*, the radiative equilibrium with $J = S$ and the adiabatic equilibrium with $\nabla = \nabla_{\rm ad}$. The stratification which is closest to the adiabatic equilibrium will therefore have the least convective cooling and and the smallest convective overshoot flux (which is negative). This is precisely what we observe in the simulations, with the η Boo-simulation displaying less than half the overshoot flux of the solar simulation. A detailed analysis will be presented in a future paper.

On the backdrop of the analysis above, we therefore feel confident in the T-τ relations presented in Fig. 20. The reason that the ZAMS sequence in Fig. 19 approaches the grey atmosphere and not the adiabatic stratification is that the continuum opacity increases (as higher levels of hydrogen become more populated) as the lines fade

away. The radiative heating therefore remains stronger than the convective cooling and the equilibrium state is determined by the radiative transfer.

It is worth noting here that the "approximate overshooting" introduced by (Kurucz 1993; Kurucz 1992c) entails a positive overshooting flux, which is at odds with the convection simulations, as well as the basic expression for the convective flux; $F_{\rm conv} \propto (\nabla - \nabla_{\rm ad})$, as also discussed by Castelli et al. (1997).

5.1.9 The depth of outer convection zones

The depth of an outer convection zone depends in a complex way on the surface boundary conditions. With some simplifications we can, however, still get a rough idea of the mechanisms involved. We convert the equation of hydrostatic equilibrium to an optical depth scale

$$\frac{{\rm d}P_{\rm g}}{{\rm d}\tau} = \frac{g}{\kappa} \,, \tag{173}$$

and integrate from $\tau = 0$ and inwards

$$P_{\rm g} = \frac{g}{\bar{\kappa}}\bar{\tau} \,, \tag{174}$$

where $\bar{\kappa}$ and $\bar{\tau}$ are some appropriate averages. This gives us a first order estimate of the effects of changing various parts of the physics. The precise form of the averaging is immaterial to the present discussion as we are interested only in the differential response to changes in the physics.

If for $\bar{\tau}$ we use some average of the inverse T-τ relationwe obtain a relation

between T and $P_{\rm g}$. An increase in $T(\tau)$ will decrease $\tau(T)$, as the T-τ relation is monotonically increasing, and will therefore have the same effect on $P_{\rm g}$ as will an increase in the opacity.

We will now assume that a change in the atmospheric opacity will change the pressure by the same factor in the whole convection zone. The change in depth of the convection zone can be derived from the response to such a pressure change at the bottom of the convection zone. The Schwarzschild criterion for convection to occur

$$\nabla_{\rm rad} > \nabla_{\rm ad} \ , \tag{175}$$

is mainly governed by $\nabla_{\rm rad}$, as the adiabatic gradient is very close to the ideal- and fully ionized-gas value of $\nabla_{\rm ad} = \frac{2}{5}$ at the bottom of deep convection zones.

The radiative temperature gradient

$$\nabla_{\rm rad} = \frac{3\pi}{16\sigma}\frac{\kappa F_{\rm rad} P_{\rm g}}{gT^4} \tag{176}$$

will decrease by a decrease in pressure and the bottom of the convection zone will therefore move outward a little. Since $\nabla_{\rm rad}$ depends strongly on temperature, and has a very steep gradient at the bottom of the convection zone, the pressure-change hardly affects the location of $\nabla_{\rm rad} = \nabla_{\rm ad}$ on the temperature-scale. The largest effect is therefore due to the (almost unchanged) temperature at the bottom of the convection zone occurring at a smaller pressure. If on the other hand q_1 is changed, the decrease in pressure is accompanied by a decrease in temperature, more or less

counteracting the effect of the smaller pressure.

This trend is confirmed by the experiments. We calculated envelope models with small changes (0.001) to α, q_1 and the atmospheric $\ln\kappa$ in order to find the differential changes to the relative depth of the convection zone (Table 9). The magnitude of $\frac{\partial d_{\rm CZ}}{\partial q_1}$ is smaller than $\frac{\partial d_{\rm CZ}}{\partial \ln\kappa}$ and may even have the opposite sign. From the table we see that $\frac{\partial d_{\rm CZ}}{\partial q_1}$ and $\frac{\partial d_{\rm CZ}}{\partial \ln\kappa}$ have the same sign, except for Star B and η Boo, which have opposite and rather small responses to changes in q_1 and opacity. We also see that the same two stars react the strongest to changes in α.

Table 9. Response to changes in q_1, $\ln\kappa$ and α.

name	$\frac{\partial d_{\rm CZ}}{\partial \alpha}$	$\frac{\partial d_{\rm CZ}}{\partial q_1}$	$\frac{\partial d_{\rm CZ}}{\partial \ln\kappa}$	$d_{\rm CZ}/R_*$
Star A	0.0965	-0.0878	-0.2404	0.5600
α Cen B	0.0616	-0.0542	-0.1430	0.3063
Sun	0.1171	-0.1064	-0.2264	0.2861
α Cen A	0.1414	-0.1220	-0.2630	0.3070
Star B	0.2479	0.0192	-0.0684	0.1966
η Boo	0.2763	0.0577	-0.0617	0.2087
Procyon	0.1706	-0.2766	-0.2836	0.1035

The convective flux in the MLT formulation may be written as

$$F_{\rm conv} = \frac{5}{4}\sqrt{\frac{\delta\mu M_{\rm u}}{\nu k}}\alpha^2\frac{P_{\rm g}^2}{T^{3/2}}(\nabla-\nabla')^{3/2}, \qquad (177)$$

where k is Boltzmann's constant, $M_{\rm u}$ is the atomic mass unit, $\delta = -(\partial\ln\varrho/\partial\ln T)_P$, and μ is the mean molecular weight, both of which are fairly unaltered with changing conditions in the atmosphere. The average temperature gradient is called ∇ and ∇' is the gradient in the convective cells. Their difference is almost equal to the

super-adiabatic gradient, $\nabla - \nabla_{\rm ad}$. From this we see that an increase in temperature and/or a decrease in pressure (brought about by changes to the T-τ relation or the atmospheric opacity) will be accompanied by an increase in $\nabla - \nabla_{\rm ad}$ in order to maintain the total flux (and the fixed $T_{\rm eff}$ of the model). This increase of $\nabla - \nabla_{\rm ad}$ corresponds to a decrease of the efficiency of the convection, which will lead to a smaller convection zone. The effect can be counteracted by increasing α, increasing the efficiency by increasing the distance traveled by convective elements. An increase in the efficiency of convection will enlarge the convection zone, as also seen from Tab. 9.

As far as global observables are concerned, uncertainties in the atmospheric opacities, line-blocking and mismatches between the τ-scale and the grey opacity may be hidden in α *together* with pure convection effects. This is one reason that so many values for the solar α can be found in the literature (Another reason being the lack of concensus on the values for the auxilliary MLT parameters). As illustrated by Tab. 9, such flaws in the treatment of the photosphere will not have the same effect on all stars and we consequently expect an incorrect differential behavior, possibly masking real convection effects.

In Tab. 7 we compare the convection zone depths obtained from envelope models with different choices for the T-τ relation but constant, individual α's (as found in Paper II). The first row of d_{CZ} is for the individual T-τ relations, derived from the simulations as described in Sect. 5.1.5 and using the same Rosseland opacities in the envelope model as in the computation of the T-τ relation. This is the procedure we recommend and which separates the radiative contribution to the efficiency of

the convection from intrinsic convection effects. The individual T-τ relations are compared in Fig. 21.

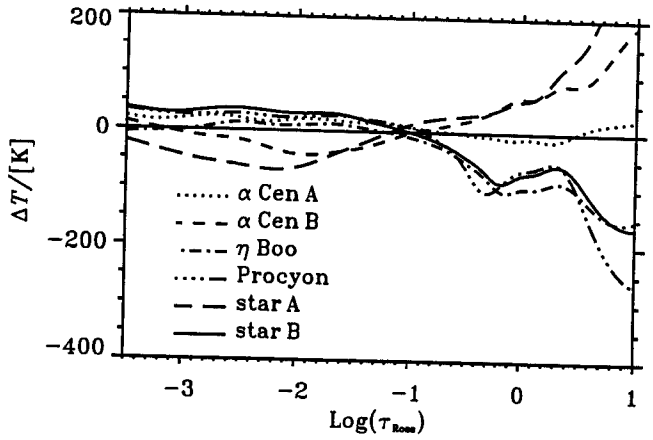

Fig. 21. Scaled T-τ relations for the seven simulations, relative to the solar simulation in the sense: $T_* \times (T_{\rm eff,\odot}/T_{\rm eff,*}) - T_\odot$. The more vigorous the convection, the flatter the T-τ relation.

The next three rows of Tab. 7 give the convection zone depth for some of the commonly used approximations. The first uses the solar T-τ relation for all the stars, where we use the T-τ relation from Sect. 5.1.6, which is based on a simulation with higher resolution and lower $T_{\rm eff}$ than the one listed as "Sun" in Tab. 7. The next approximation uses individual T-τ relations based on the monochromatic, 5000 Å, τ-scale but still using the Rosseland opacity for the grey opacity in the envelope. The opacities, κ_{5000} and $\kappa_{\rm Ross}$ are calculated with the same code, physics and abundances. Last we use the T-τ relation from the Harvard-Smithsonian reference atmosphere (Gingerich et al. 1971). From Fig. 16 we see that $d_{\rm CZ}^{5000}$ and $d_{\rm CZ}^{\rm HSRA}$ for the solar simulation differ from $d_{\rm CZ}$, approximately in proportion to the corresponding differences in the T-τ relation around $\tau = 1$. This also confirms the trends of the linear analysis listed in Tab. 9, as the various convection zone depths listed in Tab. 7 stem from

changes to the T-τ relation only.

5.1.10 Conclusion

We confirm that the use of T-τ relations is indeed a reasonable way of incorporating the effects of full radiative transfer in stellar structure computations—even in the non-grey case.

Based on that we proceed to compute T-τ relations for a small number of 3D simulations of radiation-coupled convective stellar atmospheres. Each of the T-τ relations were fitted to analytical expressions, the coefficients of which were fitted to linear expressions in the atmospheric parameters, $T_{\rm eff}$ and $g_{\rm surf}$, for easy implementation in stellar structure codes.

We have investigated how changes to the radiative part of the outer boundary affects the structure of a star, using the depth of the outer convection zone as a global measure. We evaluated the linear response of the change in depth of the convection zone caused by changes in atmospheric opacity, T-τ relation and mixing length, respectively. Our analysis shows that the convection zone is about equally sensitive to the three kinds of changes and, consequently, different parameter-triplets can easily result in the same global properties of a stellar model. References to a particular mixing length are therefore less useful unless accompanied by references to the atmospheric opacity and T-τ relation.

We also compare the effects of various commonly used assumptions about the T-τ relation, and conclude that scaled solar T-τ relations introduce systematic effects,

while the use of an 5000 Å T-τ relation with a Rosseland opacity has an even larger effect and should be avoided.

To separate the effects of convection from those of the radiative transition in the photosphere, and to avoid unnecessary systematic effects, we recommend a consistent usage of T-τ relations and their corresponding opacities in stellar structure and evolution calculations.

Extrapolation of the parameterized T-τ relations towards lower gravity (see Fig. 20) prompted a closer investigation of the interplay between convection and radiation, above the convection zone. We have gained new insights into the physics governing the overshoot of convective flows into the stably stratified parts of the atmosphere; when radiative heating is inefficient, the temperature will approach the adiabatic stratification and the (negative) overshoot flux will diminish. A more detailed analysis will be presented in a future paper. The effect on atmospheric stratification is, however, included in our fit to the T-τ relations as presented in Eqs. (168), (170), (171) and Tab. 8, and it is ready to be implemented in stellar structure and evolution codes.

As precision and scope of modern observations of stars steadily improve, and as we are entering the age of astero-seismology, higher demands are placed on the modeling of stars. With improved understanding and treatment of the interplay between radiation and convection, we will be able to isolate other effects that so far have been shrouded in the uncertainty of the atmospheric part of stellar models. With improved outer boundary conditions, combined with the mixing-length calibration in Paper II, we can have more confidence in predictions about the depth of convective

envelopes. This, in turn, will allow us to study other mixing processes, such as convective overshoot at the base of the convection zone, rotational mixing, g-mode mixing, etc. and compare with observations of chemical enrichment from dredge-ups and the destruction of volatile elements such as Li.

5.2 Calibrating the mixing-length

The mixing-length parameter α is calibrated using realistic 3D radiation hydrodynamical (RHD) simulations of seven stars in the solar neighborhood of the HR-diagram. The calibration indicates a small variation of α with surface gravity, $g_{\rm surf}$, and a larger variation with effective temperature, $T_{\rm eff}$. We give a simple fit to these results.

5.2.1 Introduction

Due to the lack of a better theory of convection in stars, the mixing-length theory (MLT) has been used for almost 60 years. By far the largest part of the solar convection zone is very close to adiabatic, and the stratification in the bulk of the convection zone is therefore determined by the adiabatic temperature gradient, $\nabla_{\rm ad} = (\partial \ln T/\partial \ln P)_{\rm ad}$. Convection is so efficient that only a very small excess gradient, or super-adiabatic gradient, $\nabla_s = \nabla - \nabla_{\rm ad}$ is sufficient for transporting the entire energy flux. In most of the convection zone the super-adiabatic gradient is tiny, $\nabla_s \lesssim 10^{-5}$, which hardly adds up to anything significant even integrating over the whole convection zone. We therefore have no need for a theory of convection here.

This picture changes dramatically near the boundaries, especially near the upper boundary of an outer convection zone. Here convection becomes exceedingly inefficient in transporting the energy flux, as radiative energy transport takes over. For the sun, this layer of appreciable superadiabaticity only takes up the outermost

1 Mm, just below the photosphere, in the region where the gas becomes optically transparent and the radiation escapes. This layer, however thin, is crucial for the star as a whole, as it is the stars insulation against the cold of space.

With the advances in atomic physics as applied to astrophysics, *i.e.*, the EOS (Hummer & Mihalas 1988; Nayfonov et al. 1999; Gong et al. 2001b; Rogers & Nayfonov 2002; Saumon et al. 1995) and opacities (Seaton 1995; Berrington 1997; Iglesias & Rogers 1996; Kurucz 1992b; Alexander & Ferguson 1994), by far the most uncertain aspects of stellar models are associated with dynamical phenomena: semi-convection, rotational mixing, mixing by g-modes, convective over-shooting and the most prominent; convection itself.

The present paper is part of an effort to improve on stellar structure models, by using results from a number of 3D convection simulations of stars in the solar neighborhood of the HR-diagram. The first paper in this series, deals with the radiative part of the stellar surface problem, and presents T-τ relations derived from the simulations (Trampedach et al. 2004d, paper I). The present paper is Paper II. Paper III will address the consequences, of the results from the first two papers, for stellar evolution (Trampedach et al. 2004b).

This paper is not a justification of the MLT, nor is it aimed at describing the structure of the surface layers of stars. Rather, we provide a way to use MLT and a non-constant α to correctly model the depth of outer convection zones. MLT in general, and our calibration of α in particular, has limited relevance to stellar atmosphere calculations.

The present paper is also a continuation of the work presented in Trampedach

et al. (1997), which unfortunately turned out to be flawed by inadequate T-τ relations.

5.2.2 Mixing-length vs. 3D convection

The conventional interpretation of the mixing-length formulation of convection, is that of bubbles, eddies or convective elements, that are warmer than their surroundings, rising due to their buoyancy. The Schwartzschild criterion for stability against convection: $\nabla_{\rm rad} < \nabla_{\rm ad}$, is equivalent to the statement that convection will occur, when gas which is warmer than its surroundings, is buoyant. The "rad" and "ad" subscripts indicate the $\nabla = {\rm dln}T/{\rm dln}P$ in the case of radiative and adiabatic stratifications, respectively.

These bubbles of gas are then envisioned to travel for one mixing-length—hence the name—before they dissolve more or less abruptly (Böhm-Vitense 1958). This picture has conceptual problems at the edges of convection zones or in small convective cores, where the distance to the edge is only a fraction of a mixing-length. Most often, the convective elements are also ascribed an aspect-ratio around unity, confounding the problem.

The mixing-length is typically chosen to be $\Lambda = \alpha H_\varrho$ or αH_p, where α is the main free parameter (of order unity) of the formulation, and H is the density- or pressure-scale-height for locally exponential stratifications. It has also been suggested to use $l = \alpha z$, where z is the distance to the top of the convection zone (Canuto & Mazzitelli 1991; Canuto & Mazzitelli 1992). This choice would solve the conceptual problems listed above, but it introduces physical problems since there are strong reasons for

real convection to have a stratification similar to an MLT model with $\Lambda = \alpha H_\varrho$, as mentioned below.

There is also a notion of a background of the average stratification, that these convective bubbles travel in. A little like the bubbles rising in a glass of beer, for instance; The concept of a background liquid is rather obvious, with isolated and distinguishable bubbles rising in it.

In the 3D simulations of convection, on the other hand, we see a very different phenomena (see also Stein & Nordlund 1989; Nordlund & Stein 1997). The convection consists of continuous flows; the warm gas rising almost adiabatically, in a background of narrower and faster down-drafts, forced by sheer mass-conservation. A fraction of the up-flows is continuously overturning in order to conserve mass on the back-drop of the steep and exponential density gradient.

Locally, the density can be approximated by

$$\varrho \propto e^{z/H_\varrho} \ . \tag{178}$$

When a vertical "slice" of the up-flow has traveled Δz, the slice would therefore be over-dense by a factor of $e^{\Delta z/H_\varrho}$, if the up-flow was confined horizontally. There is of course no such confinement, and the fraction, $(e^{\Delta z/H_\varrho} - 1) \rightarrow \Delta z/H_\varrho$ for $\Delta z \rightarrow 0$, will overturn into the down-drafts.

The up-flow will therefore be "eroded" with an e-folding scale of H_ϱ. The result of this concept is actually the same as that for the mixing-length picture described above (with $\Lambda = \alpha H_\varrho$), but without the same conceptual problems, since the flows

are continuous and the overflow from the up-flow and into the down-drafts, likewise happens on a continuous basis.

Renaming it the erosion- or dilution-length formulation, it could be a first order approximation to convection, as observed in the 3D simulations. This is probably the reason that the MLT formulation has worked so well despite its short-comings; It is based on simple mass conservation.

The above argument neglects vertical velocity gradients. A positive gradient outwards would accommodate more of the up-flow and result in a smaller fraction of the up-flow overturning. With some assumptions on the velocity-gradient, this could be included by means of a factor on the erosion-length, and various geometrical conversions could be included here as well. This is the α we are calibrating in the present paper.

The 3D simulations also display a nearly laminar up-flow, due to the density gradient smoothing out most of the generated turbulence. The down-flows are narrower and faster, and since they work against the density gradient, they are also more turbulent. The down-drafts are not compressed adiabatically, since there is continuous entrainment of hot plasma from the neighboring up-flows. The down-drafts are therefore super-adiabatic much further in than the up-flows which mainly become super-adiabatic from radiative loss of energy around the local $\tau \simeq 1$. There is also a lateral exchange of energy, extending the super-adiabatic peak in the up-flow to larger depth than would have been the case with a purely vertical loss of radiative energy. The super-adiabatic peak produced by the combination of these three phenomena is difficult to reproduce within the MLT frame-work (See Sect. 5.2.6).

The convective motions in the 3D simulations, are prolific above the convection zone, with the velocity decreasing with a scale-height which is larger than the pressure scale-height. This introduces a new contestant in the atmosphere, and radiative transfer will have to compete with adiabatic cooling for the equilibrium stratification, as discussed in Paper I.

The asymmetry in the up-flows and the down-drafts have some profound effects: In the photosphere, for example, the highly non-linear opacity coupled with the large temperature contrast, results in a $\tau = 1$ surface which is very undulated; Over the hot granules, the photosphere is located at larger geometrical height than the cooler inter-granular lanes, and the observed (disk-center) temperature contrast is therefore much smaller than in a horizontal cross-section. This introduces a *convective back-warming* on the geometrical scale, which has no counterpart on the optical depth-scale.

In the convective layers, the density and velocity differences between the up-flows and the down-drafts, give rise to a net kinetic energy-flux

$$F_{\rm kin} = \frac{1}{2}\varrho v^2 v_z \ , \tag{179}$$

which amounts to about a tenth of the total flux. The assumption of symmetry in the MLT formulation, precludes such a kinetic energy-flux, and is probably the biggest cause for disagreement with the simulations in the deeper, almost adiabatically convective layers.

As convection quickly approaches the adiabatic stratification, an actual theory of convection is hardly necessary in the bulk of a convection zone that encompasses more

than a few pressure-scale-heights. There we only need to determine which adiabat the star is following. Since α is not fixed by the MLT formulation, the answer has to come from "outside" calibrations, *e.g.*, through matching of the radius of a solar model evolved to the present age (Gough & Weiss 1976), or as performed in the present paper.

5.2.3 The simulations

The fully compressible RHD simulations are described by Nordlund & Stein (1990), and general properties of solar convection, as deduced from the simulations, are discussed by Stein & Nordlund (1998). Among the code features, important for the present analysis, are radiative transfer with line-blanketing (Nordlund 1982; Nordlund & Dravins 1990), and the transmitting top and bottom boundaries. The bottom is kept at a uniform pressure (but not constant in time), to make a node in the radial p-modes and minimize wave generation by the boundary conditions. The entropy of the in-flowing plasma is adjusted to result in the desired effective temperature, and the outflow is left unchanged.

The convection in the simulations, consists of a warm, coherent up-flow, with its entropy virtually unaltered from its value near the bottom of the convection zone. Because of the density gradient, mass conservation forces overturning of the up-flows, on distances of the order of the density scale height. The overturning plasma is entrained into narrow, fast and turbulent, entropy deficient down-drafts, generated by the abrupt cooling in the photosphere. Since only a small part of the convection

zone is simulated, open boundaries are necessary for obtaining realistic results.

Another requirement for comparison with observations is a realistic treatment of the radiative transfer in the atmosphere, and a corresponding quality of the atomic physics behind the opacities and the equation of state (EOS). Compared to the simulations cited above, we have therefore employed the so-called MHD EOS (Hummer & Mihalas 1988; Däppen et al. 1988), updated most of the continuous opacity sources and added a few new ones, as described in detail in Trampedach (1997). The line opacity is now supplied by opacity distribution functions (ODF) by Kurucz (1992a; 1992b).

Each of the simulations were performed on a $50 \times 50 \times 82$ grid. After relaxation to a quasi-stationary state, we calculated mean models for the envelope fitting (*cf.* Sect. 5.2.5). The temporal averaging was performed on a horizontally averaged column density scale, instead of a direct spatial scale, to filter out the main effect of the p-modes excited in the simulations.

The seven simulations investigated are listed in Tab. 10. Five of them correspond roughly to actual stars. The chemical composition is, mostly for historical reasons, $X = 70.2960\,\%$ hydrogen by mass and $Z = 1.78785\,\%$ metals by mass.

In Fig. 22 we have plotted the seven simulations in an HR-diagram together with evolutionary tracks (), for stars with masses between 0.85 and 1.7 $M_\odot$, as indicated. The two fictitious stars, Star A and B, can of course be shifted up or down in luminosity, depending on what mass actually corresponds to the given atmospheric parameters.

Table 10. Parameters for the simulations, and derived α's and convection zone depths, d_{CZ}.

name	α Cen B	Star A	Sun	α Cen A	Star B	η Boo	Procyon
Spectral class	K1V	K2	G2V	G2V	F8	G0IV	F5IV-V
$T_{\rm eff}$	5362 K	4851 K	5801 K	5768 K	6167 K	6023 K	6470 K
$g_{\rm surf}/[{\rm cm^2\,s^{-1}}]$	$3.604{\cdot}10^4$	$1.243{\cdot}10^4$	$2.740{\cdot}10^4$	$1.970{\cdot}10^4$	$1.084{\cdot}10^4$	$5.668{\cdot}10^3$	$1.084{\cdot}10^4$
$M/M_\odot$	0.900	0.600	1.000	1.085	1.240	1.630	1.750
$\max(P_{\rm turb}/P_{\rm tot})$	7.8%	8.2%	10.7%	11.2%	15.5%	19.5%	21.0%
α	1.8313	1.8705	1.8171	1.8032	1.7360	1.7383	1.7193
$d_{\rm CZ}$	0.3063	0.5600	0.2861	0.3070	0.1966	0.2087	0.1035

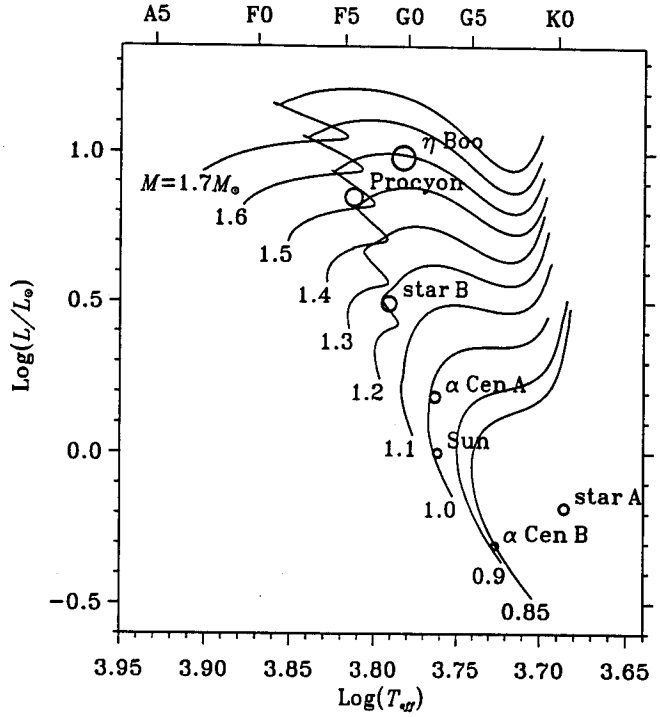

Fig. 22. The position of the seven simulations in the HR-diagram. The size of the symbols, reflects the diameter of the star. We have also plotted evolutionary tracks, with masses as indicated, to put the simulations in context.

5.2.4 The envelope models

The simulations were fitted to 1D, spherically symmetric envelope models (Christensen-Dalsgaard & Frandsen 1983), which extend down to a relative radius of $r/R = 0.05$,

and up to an optical depth of $\tau = 10^{-4}$.

We used the same MHD EOS, and in the atmospheric part of the envelopes we used the same opacities, as in the convection simulations. These atmospheric opacities are smoothly joined with the OPAL opacities (Rogers & Iglesias 1992a) in the temperature interval, $T = 2.6$–4.1×10^4 K.

Convection is treated using the standard MLT as described in Böhm-Vitense (1958), using the standard mixing length

$$l = \alpha H_P \tag{180}$$

and form factors $y = \frac{1}{3}$ and $\nu = 8$. We use the notation introduced by Gough (1977), in which the form-factors are $\Phi = \nu/4 = 2$ and $\eta = 4y/(3\sqrt{\nu}) = \sqrt{2}/9$.

The photospheric transition from optically thick to optically thin is treated by means of T-τ relations derived from the simulations. We calculated temporal and $\tau_{\rm Ross}$ (Rosseland optical depth) averaged temperatures, and fitted these to analytical expressions which were used in the envelope models. The fitting formula and the coefficients are given in Paper I. The point that we use individual T-τ relations instead of scaled solar T-τ relations is crucial for the present calibration, as discussed in Paper I.

The pressure in the simulations is not purely thermodynamic; turbulent pressure also contributes to the hydrostatic equilibrium. We therefore include a turbulent

pressure in the envelopes, based on the MLT convective velocities

$$P_{\rm turb,1D} = \beta v_{\rm conv}^2 \varrho \ , \tag{181}$$

where β is a constant, adjusted as part of the calibration procedure, as described in Sect. 5.2.5. We suppress the turbulent pressure in the envelopes with a smooth cutoff just above the matching point, to avoid spurious effects on the structure of the envelope model. This has two reasons: The practical one, is that most stellar structure calculations do not include such a turbulent pressure, and a calibration of α, including $P_{\rm turb,1D}$ in the whole convection zone, would not apply in these cases. The second, and more physical reason, is that $v_{\rm conv}$ in MLT models has a very unphysical behavior, and gives rise to an even less physical $P_{\rm turb,1D}$. The turbulent pressure in the part of the envelope above the matching point would change the outer boundary condition for the envelope, which can have a significant global effect on the model. The velocity drops from an unrealistically high, supersonic maximum, down to zero, in a fraction of a pressure scale height, giving rise to a devastating pressure gradient. To enable integration of hydrostatic equilibrium, it is necessary to introduce some cutoff, which undoubtedly will introduce an unphysical differential behavior of this MLT turbulent pressure.

In the simulations on the other hand, turbulent pressure peaks about half a pressure-scale-height below the top of the convection zone, drops off smoothly both above and below and is non-zero everywhere.

We recommend not including a 1D-turbulent pressure which is confined to the

convection zone, *i.e.*, do not incorporate an overshoot region.

Well below the super-adiabatic top of the convection zone, $P_{\rm turb,1D}$ does however match the turbulent pressure of the simulations rather well, giving an almost differentiable match. We take this as evidence, that envelope models including $P_{\rm turb,1D}$, with β and α fitted as described in Sect. 5.2.5, gives a realistic extension of the simulations towards the center of the star. This fact was exploited in an investigation of convective effects on the frequencies of solar oscillations (Rosenthal et al. 1999) by analyzing eigenmodes in a model combining the simulation and a matched envelope model. We can now proceed with the matching, with confidence.

5.2.5 Matching to envelopes

In order to derive α's from the simulations, we matched horizontal and temporal averages of the 3D simulations to 1D envelope models at a common pressure point deep in the simulation. The matching is performed by adjusting β till the 3D- and 1D-turbulent pressures agree, and α till the temperatures agree.

This method demands a high degree of consistency between the simulations and the envelope models at the matching point, which is the reason for using the exact same EOS (and chemical composition) in both cases, and for including a turbulent pressure in the deep part of the envelope models. The matching is furthermore performed at a depth in the simulation, where boundary effects are small and fluctuations in the thermodynamic quantities are small. The latter to ensure that the mean ϱ, T and $P_{\rm gas}$ are related by the EOS, *i.e.*, that direct 3D-effects are negligible, as is of

course always the case in the envelope models.

In order to filter out non-convective effects from this calibration of α, we also demand consistency in the treatment of radiative transfer at the top of the convection zone. We accomplish this by using the Rosseland opacities from the simulations, in the atmospheres of the envelopes, and using T-τ relations derived from the simulations, based on this opacity (See Paper I for details).

The combination of the average stratification of the simulations in the atmosphere, and the matched envelope in the interior, have recently been used by Georgobiani et al. (2003b), as a basis for computing the excitation of stellar p-modes for the stars listed in our Tab. 10.

5.2.6 Results and discussion

The results of this envelope matching is listed in Tab. 10 where we list both α for the matched envelope, and the relative depth of the convection zone, $d_{\rm CZ}$. The simulations are listed in order of increasing vigor of the convection, translating into decreasing α's (decreasing efficiency of convection) and decreasing relative depth of the convection zone. As a measure of how vigorous the convection is, we use the maximum of the turbulent to total pressure ratio, as listed in the fifth row of Tab. 10.

In Fig. 23 we show the α's from the envelope matching as function of $T_{\rm eff}$, as $*$-symbols. Those values are plotted with error-bars, corresponding to the RMS scatter in α derived from envelope matching to individual time-steps of the simulations. This

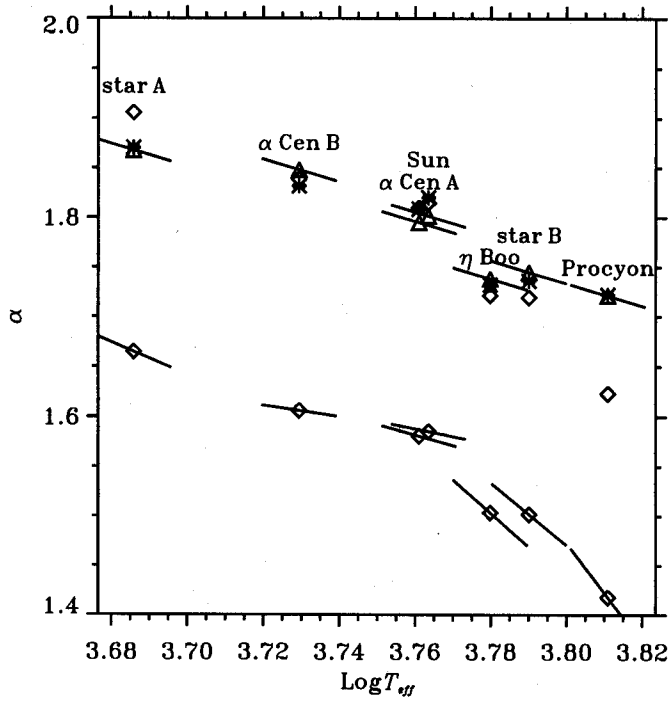

Fig. 23. A plot of the α's found from the matching procedure (stars), compared with the linear fit from Eqs. (182) and (183) (triangles). The (lower) diamonds show the 2D calibration by Ludwig et al. (1999), which we have also multiplied by 1.14 to agree with our result for the Sun (upper diamonds). The line-segments show the local Log$T$-derivative of the fitting expressions.

scatter is rather small; 1–3$\times 10^{-3}$, and is hard to see in the figure.

We fit the derived α's to a simple function of the form

$$\alpha_{\rm fit} = \alpha_\odot + A \log \frac{T_{\rm eff}}{T_{\rm eff,\odot}} + B \log \frac{g_{\rm surf}}{g_{\rm surf,\odot}} + \frac{{\rm d}\alpha}{{\rm d}Y}(Y - Y_\odot) \tag{182}$$

and find

$$\alpha_\odot = 1.81795 \quad , \quad \frac{{\rm d}\alpha}{{\rm d}Y} = -1.32012 \, ,$$
$$A = -1.11208 \quad \text{and} \quad B = 0.07454 \tag{183}$$

which is shown as triangles in Fig. 23, with the $\log T$-gradient indicated with line-segments. This linear fit has a standard deviation of $\sigma = 0.012$, whis is more than an order of magnitude less than the variation of α over the seven stars. It is also an order of magnitude larger than the RMS scatter in α from envelope matching to individual time-steps. This indicates that the variation of α is not optimally described by a plane. We find it prudent, however, to keep the fit linear in order to avoid divergences outside our rather limited fitting region of the seven simulations.

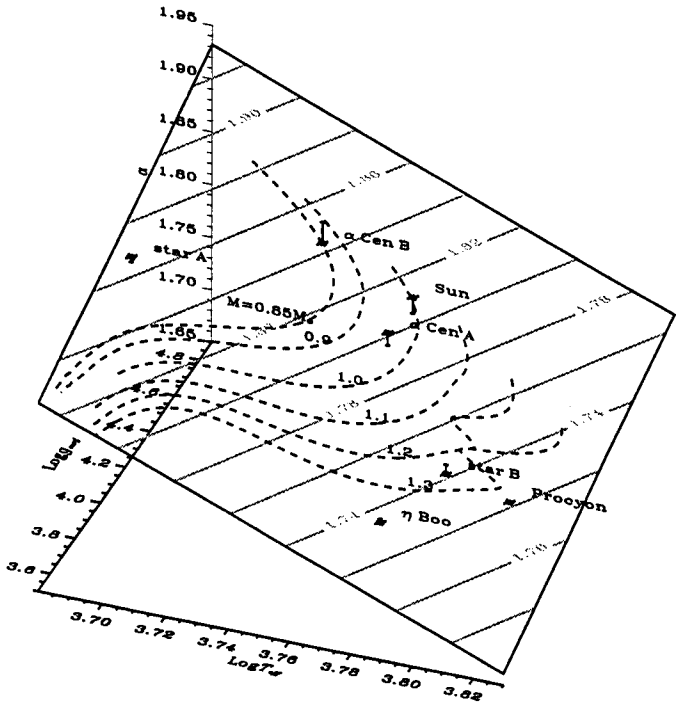

Fig. 24. This figure shows α's behavior with $T_{\rm eff}$ and $g_{\rm surf}$. The surface is the fit given in Eq. (182). The dashed lines shows evolutionary tracks for stellar masses as indicated. The stars show the α's as listed in Tab. 10 and the little circles, connected by lines, show the projection onto the fitting-plane.

A similar calibration of α against 2D RHD simulations has been performed by Ludwig et al. (1999, from here on LFS), using a method completely independent of ours. In Fig. 23 we have displayed their fit to their results, as applied to the atmospheric parameters of our simulations (lower set of $\diamond$'s, with line-segments indi-

cating local log$T$-derivatives). Based on the requirement of matching the radius of the present age Sun, they allow for a scaling of their results by 1.1–1.2 to translate from 2D to 3D.

Our results do indeed agree in the solar vicinity, after a scaling by 1.14, as shown by the upper set of $\diamond$-symbols in Fig. 23. The disagreement for Star A is most likely due to differences in the opacities. They base their opacities on the Atlas6 line-opacities whereas we use the newer Atlas9 line-opacities (in the form of opacity distribution functions). The difference, as outlined by Kurucz (1992d), consists of the addition of molecular opacity (hydrides and CN, C_2 and TiO) and improved calculations for the iron-group elements — all in all a factor of 34 more molecular, atomic and ionic lines.

These opacity changes should affect the hotter stars the least, but they still have an effect on the solar model—that was after all the main motivation behind the opacity updates (Kurucz 1992b). We therefore suspect that the factor translating LFS' results from 2D to 3D should be closer to 1.21, to bring the Procyon results into agreement. The differences for the other simulations would then be due to the opacity update. LFS used grey radiative transfer in the bulk of the 58 2D simulations going into their analysis, adding another systematic difference (also decreasing with $T_{\rm eff}$) between our results.

The fit by LFS have more degrees of freedom, as warranted by the much larger set of simulations. They also cover a larger area of the $T_{\rm eff}/g_{\rm surf}$-diagram making non-linear behaviour more pronounced. It is, however, interesting to note that our results are rather well described by a bi-linear fit in log$T_{\rm eff}$ and log$g$. We are obviously

eager to extend the present analysis to larger temperatures and lower gravities.

It seems natural to expect that quantities other than $T_{\rm eff}$ and $g_{\rm surf}$, would be more relevant for describing the efficiency of convection. The optical depth at the top of the convection zone, for example, seems much more relevant and directly related to the issue. This quantity, and other related ones, appear to give worse fits, than the one presented above. The reason for this is still unclear.

It can be argued that the set of atmospheric parameters we have chosen for our simulations lies close to a line instead of delineating an area, and therefore only the change of α along this line can be significant. Again we refer to the relative agreement with the findings of Ludwig et al. (1999), who explored a larger area in the $T_{\rm eff}/g_{\rm surf}$-plane. Also the η Boo- and Star A-simulations are rather far away from that line and yet they both lie very close to the fitting-plane.

In Fig. 24 we show the linear fit of Eqs. (182) and (183), as function of both effective temperature and gravity. Contours, in grey, are shown for every 0.01 and labelled for every 0.02. We have also over-plottet values found from the envelope matching procedure ($*$-symbols), and connected them to the corresponding points on the plane, with small vertical line-segments. The dashed lines show the evolutionary tracks from Fig. 22, with masses decreasing upward as indicated.

Fig. 24 shows a very interesting trend; The evolutionary tracks show that the stars on the zero age main sequence have α's that depend strongly on mass ($\alpha \simeq 2.11 - 0.27 M/M_{\odot}$), but their α's converge towards $\alpha \simeq 1.82$ going up the Hayashi track at the low-T/low-g corner of the plot. We also see that the α Cen binary system has kept an only slightly increasing α-difference between the two components (as the

B-component evolves slower), of about 0.03. In a recent calibration of the α Cen-system, (Morel et al. 2000) find $\alpha_{A,B} = (1.86, 1.97)$, which is a bit larger difference than what we find, but it has the same sign. Using individual α's and T-τ relations, evolving with time, might help solve the longstanding problems with the modeling of this system (Fernandes & Neuforge 1995; Lydon et al. 1993).

Depth of the Solar convection zone

We have also run a simulation for direct comparison with solar observations. This simulation has a more modern composition: a helium mass-fraction of $Y_\odot = 0.245$ in accordance with helioseismology (Basu & Antia 1995), and $Z_\odot/X_\odot = 0.0245$ in agreement with meteoritic and solar photospheric metal to hydrogen ratios (Grevesse & Noels 1992). This ratio results in the hydrogen mass-fraction, $X = 73.69\%$ and the helium-hydrogen number ratio, He/H=0.0837. We have also increased the resolution to $100 \times 100 \times 82$, to better capture the granulation structure, and we have carefully adjusted the entropy of the inflowing gas (a constant) to obtain an effective temperature of $5777 \pm 14\,\mathrm{K}$, in agreement with that derived from solar irradiance observations: $T_{\mathrm{eff}} = 5777 \pm 2.5\,\mathrm{K}$, (Willson & Hudson 1988).

Matching this simulation to an envelope-model, gives $\alpha = 1.8670$, $\beta = 0.75237$ and a depth of the solar convection zone, $d_{\mathrm{CZ}} = 0.2869 \pm 0.0009\,R_\odot$. This is in good agreement with that inferred from inversion of helioseismic observations: $d_{\mathrm{CZ}} = 0.287 \pm 0.003\,R_\odot$ (Christensen-Dalsgaard et al. 1991). The uncertainty we quote for our result is merely the RMS scatter resulting from performing the full fitting of T-τ relations and envelope-matching for the individual time-steps of the simulation.

As indicated below Eq. 180, there are two more parameters to standard MLT. The two form-factors, the aspect ratio of convective elements, Φ, and η, which is related to the radiative exchange of energy between the up- and down-flows, are, however, not linearely independant and we therefore limit our discussion to η. Fitting η with respect to the height of the super-adiabatic peak, we get $\alpha = 1.9618$, $\beta = 0.72792$ and $\eta = 0.065948$, resulting in a convection zone of depth $0.2872\,R_\odot$. This value is still safely within the uncertainty of the helioseismic result. The height of the peak in the super-adiabatic gradient is increased from 0.5 in the model above, to 0.7 with the new value of η.

If on the other hand we adjust the form-factor, η, so as to obtain the same logarithmic temperature gradient, ∇, at the matching point, then we get $\alpha = 3.8545$, $\beta = 0.46403$ and $\eta = 6.3943 \times 10^{-4}$, and a convection zone of depth $0.2894\,R_\odot$. This results is not within the uncertainty of the helioseismic result. Furthermore, the peak of the super-adiabatic gradient becomes unphysically large, reaching a value of 2, about 100 km below the photosphere.

That T, ϱ and ∇ cannot be simultaneously matched at a common pressure-point (with plausible parameters), indicates that the MLT formulation converges rather slowly, if ever, towards the super-adiabatic gradient, $\nabla - \nabla_{\rm ad}$, of a real convective envelope. This might be due to the neglect of kinetic-flux in the MLT formulation, as detailed in Sect. 5.2.2.

Notice that the depth of the solar convection zone, as found above, results from *ab initio* calculations, from the EOS and opacity calculations, to the RHD simulations. The adjustable parameters that enter the simulations are the resolution, the viscosity

coefficients, and the size of the time step relative to the Courant time. These are tuned to resolve the thermal boundary layer at $\tau = 1$ and the convective structures, to minimize numerical diffusion, and to minimize the computing time. Nothing is adjusted to fit solar observations.

5.2.7 Conclusion

We have calibrated the MLT parameter α, by matching 1D envelope models with 3D RHD simulations, and established a significant variation of α with stellar atmospheric parameters $T_{\rm eff}$ and $g_{\rm surf}$. Our results point to a common value of $\alpha \simeq 1.82$ at the beginnig of the ascend up the Hayashi track and α decreasing with mass on the zero-age main-sequence.

There is of course still the possibility that we, despite our efforts, have overlooked a source of systematic errors in our calibration, but the absolute agreement with the seismologically inferred depth of the solar convection zone, found in Sect. 5.2.6, strengthens our confidence.

Although various values of α have been considered in the modeling of stellar evolution, an α varying during the evolution of a star has, to our knowledge, not been tried yet. Results of such evolution calculations are presented in Paper III.

We stress that the choice of α depends on the choice of atmospheric physics, *i.e.* T-τ relation and atmospheric opacity. Employing a scaled solar T-τ relation will alter the effect of α, as shown in Paper I. We recommend that our fitting formula, Eq. (182) be used with individual T-τ relations.

As ground-based and soon also space-borne, asteroseismology is beginning to provide strong constraints on the structure of stars, other than the Sun, stronger demands are placed on the theoretical models.

An absolute calibration of the mixing-length parameter, α, is the first step towards improving the treatment of convection in stellar structure models. A fundamentally improved formulation of convection is of course desireable, but has proven rather difficult to come by. Various attempts has been made to rectify this situation. Canuto (1993) present a formulation based on fully developed turbulence, which however, does not account for the steep density gradient and the inherent assymetry between up- and down-flows. (Lydon et al. 1992) base their model on 3D hydrodynamical simulations of convection, and this is probably the most promising way forward. A number of approximations render their results less than optimal for the next generation of convection models, however.

With the connection between MLT and the 3D convection simulations, found in Sect. 5.2.2, we believe a properly calibrated mixing-length formulation, with the mixing-length being proportional to the density or pressure scale-height, to be the best choise for the time being.

Chapter 6

Conclusions

6.1 Summary

6.2 Future Work

Bibliography

Abe, R. 1959, "Giant cluster expansion theory and its application to high temperature plasma", Prog. Theor. Phys. 22(2), 213

Aguilar, A., West, J. B., Phaneuf, R. A., Brooks, R. L., Folkmann, F., Kjeldsen, H., Bozek, J. D., Schlachter, A. S., Cisneros, C. 2003, "Photoionization of isoelectronic ions: Mg^+ and Al^{2+}", Phys. Rev. A 67, 12701

Alastuey, A., Cornu, F., Perez, A. 1994, "Virial expansion for quantum plasmas, diagrammatic resummations", Phys. Rev. E 49, 1077

Alastuey, A., Cornu, F., Perez, A. 1995, "Virial expansion for quantum plasmas, maxwell-boltzmann statistics", Phys. Rev. E 51, 1725

Alastuey, A., Perez, A. 1992, "Virial expansion of the equation of state of a quantum plasma", Europhys. Lett. 20, 19

Alexander, D. R., Ferguson, J. W. 1994, "Low-temperature Rosseland opacities", ApJ 437, 879

Allard, N. F., Kielkopf, J., Feautrier, N. 1998, "Satellites on the Lyman β line of atommic hydrogen due to $H\text{-}H^+$ collisions", A&A 330, 782

Allard, N. F., Koester, D., Feautrier, N., Spielfiedel, A. 1994, "Free-free quasi-

molecular absorption and satellites in Lyman-alpha due to collisions with H and H^+", A&AS 108, 417

Asplund, M., Gustafsson, B., Kiselman, D., Eriksson, K. 1997, "Line-blanketed model atmospheres for R Coronae Borealis stars and hydrogen-deficient carbon stars.", A&A 318, 521

Asplund, M., Nordlund, Å., Trampedach, R., Allende Prieto, C., Stein, R. F. 2000, "Line formation in solar granulation. i. fe line shapes, shifts and asymmetries", A&A 359, 729

Asplund, M., Nordlund, Å., Trampedach, R., Stein, R. F. 1999, "3D hydrodynamical atmospheres of metal-poor stars. Evidence for a low primordial Li abundance", A&A 346, L17

Asplund, M., Trampedach, R., Nordlund, Å. 1998, "Confrontation of stellar surface convection simulations with stellar spectroscopy". In (Giménez et al. 1998), 221

Badnell, N. R., Seaton, M. J. 2003, "On the importance of inner-shell transitions for opacity calculations", J. Phys. B: At. Mol. Opt. Phys. (submitted)

Basu, S., Antia, H. M. 1995, "Helium abundance in the solar envelope", M.N.R.A.S. 276, 1402

Basu, S., Antia, H. M. 1997, "Seismic measurement of the depth of the solar convection zone", M.N.R.A.S. 287, 189

Basu, S., Christensen-Dalsgaard, J. 1997, "Equation of state and helioseismic inversions", A&A 322, L5

Basu, S., Däppen, W., Nayfonov, A. 1999, "Helioseismic analysis of the hydrogen partition function in the solar interior", ApJ 518, 985

Basu, S., Thompson, M. J. 1996, "On constructing seismic models of the Sun", A&A 305, 631

Berrington, K. A. (ed.) 1997, The opacity project, Vol. 2. Institute of Physics Publishing

Berthomieu, G., Cooper, A., Gough, D., Osaki, Y., Provost, J., Rocca, A. 1980, "Sensitivity of five minute eigenfrequencies to the structure of the sun". In: H. A. Hill and W. Dziembowski (eds.), Nonradial and Nonlinear Stellar Pulsation, Vol. 125 of Lecture Notes in Physics, IAU Coll. 38, Springer Verlag, Berlin, 307

Böhm-Vitense, E. 1953, "Die Wasserstoffkonvektionszone der sonne", Zs. f. Astroph. 32, 135

Böhm-Vitense, E. 1958, "Über die Wasserstoffkonvektionszone in Sternen verschiedener Effektivtemperaturen und Leuchtkräfte", Zs. f. Astroph. 46, 108

Borysow, A., Frommhold, L. 1989, "Collision-induced infrared spectra of H_2-He pairs at temperatures from 18 to 7000 k. II. Overtone and hot bands", ApJ 341, 549

Borysow, A., Frommhold, L., Moraldi, M. 1989, "Collision-induced infrared spectra of H_2-He pairs involving $0 \leftrightarrow 1$ vibrational transitions and temperatures from 18 to 7000 k", ApJ 336, 495

Canuto, V. M. 1993, "Turbulent convection with overshooting: Reynolds stress approach. ii.", ApJ 416, 331

Canuto, V. M., Mazzitelli, I. 1991, "Stellar turbulent convection: A new model and applications", ApJ 370, 295

Canuto, V. M., Mazzitelli, I. 1992, "Further improvements of a new model for turbulent convection in stars", ApJ 389, 724

Carlsson, M., Stein, R. F. 1995, "Does a nonmagnetic solar chromosphere exist?", ApJ 440, L29

Castelli, F., Gratton, R. G., Kurucz, R. L. 1997, "Notes on the convection in the ATLAS9 model atmospheres", A&A 318(3), 841

Cauble, R., Perry, T. S., Bach, D. R., Budil, K. S., Hammel, B. A., Collins, G. W., Gold, D. M., Dunn, J., Celliers, P., Silva, L. B. D., Foord, M. E., Wallace, R. J., Stewart, R. E., , Woolsey, N. C. 1998, "Absolute equation-of-state data in the 10-40 Mbar (1-4 TPa) regime", Phys. Rev. Letters 80, 1248

Chabrier, G., Baraffe, I. 1997a, "Structure and evolution of low-mass stars", A&A 327, 1039

Chabrier, G., Baraffe, I. 1997b, "Structure and evolution of low-mass stars", A&A 327, 1039

Christensen-Dalsgaard, J. 1991, "Solar oscillations and the physics of the solar interior". In (Gough & Toomre 1991), 11

Christensen-Dalsgaard, J., Däppen, W. 1992, "Solar oscillations and the equation of state", A&AR 4(3), 267

Christensen-Dalsgaard, J., Däppen, W., Ajukov, S. V., Anderson, E. R., Antia, H. M., Basu, S., Baturin, V. A., Berthomieu, G., Chaboyer, B., Chitre, S. M., Cox, A. N., Demarque, P., Donatowicz, J., Dziembowski, W. A., Gabriel, M., Gough, D. O., Guenther, D. B., Guzik, J. A., Harvey, J. W., Hill, F., Houdek, G., Iglesias, C. A., Kosovichev, A. G., Leibacher, J. W., Proffitt, P. M. C. R., Provost, J., Reiter, J., Rhodes Jr., E. J., Rogers, F. J., Roxburgh, I. W., Thompson, M. J., Ulrich, R. K. 1996, "The current state of solar modeling", Science 272(5266), 1286

Christensen-Dalsgaard, J., Däppen, W., Lebreton, Y. 1988, "Solar oscillation frequencies and the equation of state", Nature 336, 634

Christensen-Dalsgaard, J., Frandsen, S. 1983, "Radiative transfer and solar oscillations", Sol. Phys. 82, 165

Christensen-Dalsgaard, J., Gough, D. O., Thompson, M. J. 1991, "The depth of the solar convection zone", ApJ 378, 413

Cooper, M. S., DeWitt, H. E. 1973, "Degeneracy effects in gases in the near-classical limit", Phys. Rev. A 8(4), 1910

Cox, J. P., Guili, R. T. 1968, Physical principles, Vol. 1 of Principles of Stellar Structure. Gordon and Breach, Science Publishers

Dabrowski, I. 1984, "The lyman and werner bands of h2", Canadian J. Phys. 62, 1639++

Däppen, W. 1992, "The equation of state for stellar envelopes: Comparison of theoretical results", Rev. Mex. Astron. Astrofis. 23, 141

Däppen, W. 1996, "Helioseismic diagnosis of the equation of state", Bull. Astr. Soc. India 24, 151

Däppen, W., Anderson, L., Mihalas, D. 1987, "Statistical mechanics of partially ionized stellar plasmas: The Planck-Larkin partition function, polarization shifts, and simulation of optical spectra", ApJ 319, 195

Däppen, W., Lebreton, Y., Rogers, F. 1990, "The equation of state of the solar interior: A comparison of results from two competing formalisms", Solar Physics 128, 35

Däppen, W., Mihalas, D., Hummer, D. G., Mihalas, B. W. 1988, "The equation of

state for stellar envelopes. III. Thermodynamic quantities", ApJ 332, 261

de Boor, C. 1978, A practical guide to splines. Springer Verlag

Debye, P., Hückel, E. 1923, "Zur Theorie der Electrolyte", Physic. Zeit. 24(9), 185

DeWitt, H. E. 1961, "Thermodynamics functions of a partially degenerate, fully ionized gas", J. Nucl. Energy, Part C: Plasma Phys. 2, 27

DeWitt, H. E. 1969, "Statistical mechanics of dense ionized gases". In: S. Kamar (ed.), Low Luminosity Stars, Gordon and Breach, New York, 211

DeWitt, H. E., Schlanges, M., Sakakura, A. Y., Kraeft, W. D. 1995, "Eos", Phys. Lett. A 30, 326+

Di Mauro, M. P., Christensen-Dalsgaard, J., Rabello-Soares, M. C., Basu, S. 2002, "Inferences on the solar envelope with high degree-modes", A&A 384, 666

Ebeling, W., Förster, A., Fortov, V. E., Gryaznov, V. K., Polishchuk, Y. A. 1991, Thermodynamic properties of hot dense plasmas. Teubner, Stuttgart, Germany

Ebeling, W., Kraeft, W., Kremp, D. 1976, Theory of bound states and ionization equilibrium in plasmas and solids. Akademie Verlag, Berlin, DDR

Eggleton, P. P., Faulkner, J., Flannery, B. P. 1973, "An approximate equation of state for stellar material", A&A 23, 325

Elliot, J. R., Kosovichev, A. G. 1998, "Relativistic effects in the solar equation of state". In: S. G. Korzennik (ed.), Structure and Dynamics of the Interior of the Sun and Sun-like Stars, SOHO 6/GONG 98 Workshop, ESA, Noordwijk, The Netherlands, 453

Fermi, E. 1924, "Hejsa", Zeits. f. Phys. 26, 54+

Fernandes, J., Neuforge, C. 1995, "α Centauri and convection theories", A&A 295,

678

Fowler, R., Guggenheim, E. A. 1956, Statistical thermodynamics. Cambridge University Press

Fritsch, F. N., Butland, J. 1984, "A method for constructing local monotone piecewise cubic interpolants", SIAM J. Sci. Stat. Comput. 5, 300

Georgobiani, D., Stein, R. F., Nordlund, Å., Trampedach, R. 2003a, "What causes p-mode asymmetry reversal?", ApJ (in preparation)

Georgobiani, D., Trampedach, R., Stein, R. F., Ludwig, H.-G., Nordlund, Å. 2003b, "Excitation of stellar p-mode oscillations", ApJ (in preparation)

Giménez, Á., Guinan, E. F., Montesinos, B. (eds.) 1998. Theory and tests of convection in stellar structure, ASP conf. series, First Granada Workshop

Gingerich, O., Noyes, R. W., Kalkofen, W. 1971, "The Harvard-Smithsonian reference atmosphere", Sol. Phys. 18(3), 347

Gong, Z., Däppen, W., Nayfonov, A. 2001a, "Effects of heavy elements and excited states in the equation of state of the solar interior", ApJ 563, 419

Gong, Z., Däppen, W., Zejda, L. 2001b, "Mhd equation of state with relativistic electrons", ApJ 546, 1178

Gong, Z., Zejda, L., Däppen, W., Aparicio, J. M. 2001, "Generalized fermi-dirac functions and derivatives: properties and evaluation", Comp. Phys. Comm. 136, 294

Gough, D. O. 1977, "Mixing-length theory for pulsating stars", ApJ 214, 196

Gough, D. O., Toomre, J. (eds.) 1991. Challenges to theories of the structure of moderate-mass stars, Vol. 388 of Lecture Notes in Physics, Berlin, IAU Coll. 38,

Springer Verlag

Gough, D. O., Weiss, N. O. 1976, "The calibration of stellar convection theories", M.N.R.A.S. 176, 589

Graboske, H. C., Harwood, D. J., Rogers, F. J. 1969, "Thermodynamic properties of nonideal gases. I. Free-energy minimization method", Physical Review 186(1), 210

Graboske, H. C., Olness, R. J., Grossman, A. S. 1975, "Thermodynamics of dense hydrogen-helium fluids", ApJ 199, 255

Grevesse, N., Noels, A. 1992, "Cosmic abundaces of the elements". In: N. Prantzos, E. Vangioni-Flam, and M. Cassé (eds.), Origin and Evolution of the Elements, Cambridge University press, 15

Grevesse, N., Noels, A., Sauval, A. J. 1996, "Standard abundances". In: S. S. Holt and G. Sonneborn (eds.), Cosmic Abundances, ASP, 117

Gustafsson, B., Bell, R. A., Eriksson, K., Nordlund, Å. 1975, "A grid of model atmospheres for metal-deficient giant stars I", A&A 42, 407

Harten, A. 1983, "High resolution schemes for hyperbolic conservation laws", J. Comp. Phys. 49(3), 357

Hauschildt, P. H., Allard, F., Baron, E. 1999a, "The Nextgen model atmosphere grid for $3000 \leq t_{\rm eff} \leq 10,000$k", ApJ 512, 377

Hauschildt, P. H., Allard, F., Ferguson, J., Baron, E., D. R. A. 1999b, "The NEXTGEN Model Atmosphere Grid. II. Spherically Symmetric Model Atmospheres for Giant Stars with Effective Temperatures between 3000 and 6800 K", ApJ 525, 871

Heisenberg, W. 1927, "Über die grundprinzipien der quantenmechanik", Forsch. und Fortschr. 3(11), 83

Henyey, L., Vardya, M. S., Bodenheimer, P. 1965, "Studies in stellar evolution. III. The calculation of model envelopes", ApJ 142(3), 841

Herzberg, G., Howe, L. L. 1959, "The Lyman bands of molecular hydrogen", Canadian J. Phys. 37, 636

Holtzmark 1924, "Hejsa", Phys. Zs. 25, 73+

Holweger, H., Müller, E. A. 1974, "The photospheric barium spectrum: Solar abundance and collision broadening of Ba II lines by hydrogen", Sol. Phys. 19, 19

Hooper, C. F. 1966, "Electric Microfield Distributions in Plasmas", Phys. Rev. 149, 77

Hooper, C. F. 1968, "Low-Frequency Component Electric Microfield Distributions in Plasmas", Phys. Rev. 165, 215

Huebner, W. F. 1986, Physics of the sun, Vol. 1, 33. D. Reidel Publishing Co., Dordrecht

Hummer, D. G., Berrington, K. A., Eissner, W., Pradhan, A. K., Saraph, H. E., Tully, J. A. 1993, "Atomic data from the IRON project. 1: Goals and methods", A&A 279, 298

Hummer, D. G., Mihalas, D. 1988, "The equation of state for stellar envelopes. I. An occupation probability formalism for the truncation of internal partitition functions", ApJ 331, 794

Hunter, G., Yau, A. W., Pritchard, H. O. 1974, "Rotation-vibration level energies of the hydrogen and deuterium molecule-ions", Atomic Data and Nuclear Data

Tables 14, 11

Iglesias, C. A., Rogers, F. J. 1991, "Opacity tables for Cepheid variables", ApJ 371, L73

Iglesias, C. A., Rogers, F. J. 1995, "Discrepancies between OPAL and OP opacities at high densities and temperatures", ApJ 443, 460

Iglesias, C. A., Rogers, F. J. 1995, "Disrepancies between OPAL and OP opacities at high densities and temperatures", ApJ 443, 460

Iglesias, C. A., Rogers, F. J. 1996, "Updated opal opacities", ApJ 464, 943

Iglesias, C. A., Rogers, F. J., Wilson, B. G. 1987, "Reexamination of the metal contribution to astrophysical opacity", ApJL 322, L45

Iglesias, C. A., Rogers, F. J., Wilson, B. G. 1992, "Spin-orbit interaction effects on the Rosseland mean opacity", ApJ 397, 717

Irwin, A. W. 1981, ApJS 45, 621+

Irwin, A. W. 1987, "Refined diatomic partition functions. I. Calculational methods and H_2 and CO results", A&A 182, 348

Jørgensen, U. G. 2002, "Molecules in stellar and star-like atmospheres". In: I. Hubeny, D. Mihalas, and K. Werner (eds.), Stellar atmosphere modeling, ASP, ASP, San Francisco, 303

Kippenhahn, R., Weigert, A. 1992, Stellar structure and evolution. Springer Verlag. Chp. 18.4

Kjeldsen, H., Hansen, J. E., Folkmann, F., Knudsen, H., West, J. B., Andersen, T. 2001, "The Absolute Cross Section for L-Shell Photoionization of C^+ Ions from Threshold to 105 eV", ApJS 135, 285

Kjeldsen, H., Kristensen, B., Brooks, R. L., Folkmann, F., Knudsen, H., Andersen, T. 2002a, "Absolute, State-selective Measurements of the Photoionization Cross Sections of N^+ and O^+ Ions", ApJS 138, 219

Kjeldsen, H., Kristensen, B., Folkmann, F., Andersen, T. 2002b, "Measurements of the absolute photoionization cross section of Fe^+ ions from 15.8 to 180 eV", J. Phys. B: At. Mol. Phys. 35, 3655

Koester, D., Finley, D. S., Allard, N. F., Kruk, J. W., Kimble, R. A. 1996, "Quasi-molecular satellites of Lyman beta in the spectrum of the DA white dwarf Wolf 1346", ApJ 463, L93

Kovetz, A., Lamb, D. Q., Horn, H. M. V. 1972, "Exchange contribution to the thermodynamic potential of a partially degenerate semirelativistic electron gas", ApJ 174, 109

Kraeft, W., Kremp, D., Ebeling, W., Röpke, G. 1986, Quantum statistics of charged particle systems. Plenum, New York

Krishna Swamy, K. S. 1966a. "Profiles of strong lines in G and K dwarfs", Ph.D. thesis, University of California at Berkeley. Presented in Henyey et al. (1965)

Krishna Swamy, K. S. 1966b, "Profiles of strong lines in K-dwarfs", ApJ 145, 174

Kurucz, R. L. 1992a, "Atomic and molecular data for opacity calculations", Rev. Mex. Astron. Astrofis. 23, 45

Kurucz, R. L. 1992b, "Finding the "missing" solar ultraviolet opacity", Rev. Mex. Astron. Astrofis. 23, 181

Kurucz, R. L. 1992c, "Model atmospheres for population synthesis". In: B. Barbuy and A. Renzini (eds.), The stellar population of galaxies, IAU, 225

Kurucz, R. L. 1992d, "Model Atmospheres for Population Synthesis". In: B. Barbuy and A. Renzini (eds.), The Stellar Populations of Galaxies, IAU Symp. 149, Springer Verlag, Dordrecht, 225

Kurucz, R. L. 1992e, "Remaining line opacity problems for the solar spectrum", Rev. Mex. Astron. Astrofis. 23, 187

Kurucz, R. L. 1993. Atlas9. Kurucz CD-ROM No. 13. Stellar atmosphere programs and $2\,\mathrm{km\,s^{-1}}$ grid

Kurucz, R. L. 1995, "A new opacity-sampling model atmosphere program for arbitrary abundances". In: K. G. Strassmeier and J. L. Linsky (eds.), Stellar surface structure, IAU Symp. 176, Kluwer Academic Publishers, 523

Landau, L. D., Lifshitz, E. M. 1989, The classical theory of fields, Vol. 2 of Course of theoretical Physics. Pergamon Press, Oxford, England, 4th edition

Lester, J. B. 1996, "The status of continuous opacities". In: S. J. Adelman, F. Kupka, and W. W. Weiss (eds.), Model atmospheres and spectrum synthesis, ASP, 19. Conf. Series, Vol. 108

Lewis, J. L. 1957, "Great balls of fire", "You Win Again"

Ludwig, H.-G., Freytag, B., Steffen, M. 1999, "A calibration of the mixing-length for solar-type stars based on hydrodynamical simulations. I. Methodical aspects and results for solar metallicity", A&A 346, 111

Ludwig, H.-G., Jordan, S., Steffen, M. 1994, "Numerical simulations of convection at the surface of a ZZ Ceti white dwarf", A&A 284, 105

Lydon, T. J., Fox, P. A., Sofia, S. 1992, "A formulation of convection for stellar structure and evolution calculations without the mixing-length theory approximations.

I. Application to the sun", ApJ 397, 701

Lydon, T. J., Fox, P. A., Sofia, S. 1993, "A formulation of convection for stellar structure and evolution calculations without the mixing-length theory approximations. II. Application to α Centauri A and B", ApJ 413, 390

Mihalas, D. 1978, Stellar atmospheres. W. H. Freeman and Company, 2nd edition

Mihalas, D., Däppen, W., Hummer, D. G. 1988, "The equation of state for stellar envelopes. II. Algorithm and selected results", ApJ 331, 815

Morel, P., Provost, J., Lebreton, Y., Thévenin, F., Berthomieu, G. 2000, "Calibrations of alpha Centauri A & B", A&A 363, 675

Nahar, S. N. 2003, "Photoionization cross sections of O II, O III, O IV and O V: benchmarking R-matrix theory and experiments", Phys. Rev. A (submitted)

Nayfonov, A., Däppen, W. 1998, "The signature of the internal partition function in the thermodynamical quantities of the solar interior", ApJ 499, 489

Nayfonov, A., Däppen, W., Hummer, D. G., Mihalas, D. 1999, "The MHD equation of state with post-Holtzmark microfield distributions", ApJ 526, 451

Nordlund, Å. 1982, "Numerical simulations of the solar granulation. I. Basic equations and methods", A&A 107, 1

Nordlund, Å. 1985, "Solar convection", Sol. Phys. 100, 209

Nordlund, Å., Dravins, D. 1990, "Stellar granulation. III. Hydrodynamic model atmospheres", A&A 228, 155

Nordlund, Å., Spruit, H. C., Ludwig, H.-G., Trampedach, R. 1997, "Is stellar granulation turbulence?", A&A 328, 229

Nordlund, Å., Stein, R. F. 1990, "3-D simulations of solar and stellar convection and

magnetoconvection", Comput. Phys. Commun. 59, 119

Nordlund, Å., Stein, R. F. 1991, "Granulation: Non-adiabatic patterns and shocks". In (Gough & Toomre 1991), 141

Nordlund, Å., Stein, R. F. 1997, "Stellar convection; General properties". In (Pijpers et al. 1997), 79

Nordlund, Å., Stein, R. F. 2000, "3-d convection models: Are they compatible with 1-d models?". In: L. Szabados and D. Kurtz. (eds.), ASP Conf. Ser. 203: The Impact of Large-Scale Surveys on Pulsating Star Research, IAU Coll. 176, Springer Verlag, Berlin, 362

Parkinson, W. H. 1992, "Summary of current molecular databases". In: P. L. Smith and W. L. Wiese (eds.), Atomic and Molecular Data for Space Astronomy: Needs, Analysis and Availability, Vol. 407 of Lecture Notes in Physics, 21st IAU general assembly, Springer Verlag, Berlin, 149

Pauli, W. 1925, "Über den zusammenhang des abschlusses der elektronengruppen im atom mit der komplexstruktur der spektren", Zeits. f. Physik 31, 765

Pijpers, F. P., Christensen-Dalsgaard, J., Rosenthal, C. (eds.) 1997. Solar convection and oscillations and their relationship, Dordrecht, Kluwer

Pillet, P., van Linden van den Heuvell, H. B., Smith, W. W., Kachru, R., Tran, N. H., Gallagher, T. F. 1984, "Microwave ionization of Na Rydberg atoms", Phys. Rev. A 30(1), 280

Plez, B., Brett, J. M., Nordlund, Å. 1992, "Spherical opacity sampling model atmospheres for M-giants. I. Techniques, data and discussion", A&A 256, 551

Riemann, J., Schlanges, M., DeWitt, H. E., Kraeft, W. D. 1995, "Equation of state

of the weakly degenerate one-component plasma", Physica A 219, 423

Rogers, F. 1981a, "Analytic electron-ion effective potentials for $z \leq 55$", Phys. Rev. A 23(3), 1008

Rogers, F. 1994, "Stellar plasmas". In: G. Chabrier and E. Schatzman (eds.), The Equation of State in Astrophysics, IAU Coll. 147, Cambridge University Press, 16

Rogers, F. J. 1977, "On the compensation of bound and scattering state contributions to the partition function", Phys. Lett. 61A, 358

Rogers, F. J. 1981b, "Equation of state of dense, partially degenerate, reacting plasmas", Phys. Rev. A 24, 1531

Rogers, F. J. 1986, "Occupation numbers for reacting plasmas - The role of the Planck-Larkin partition function", ApJ 310, 723

Rogers, F. J., Iglesias, C. A. 1992a, "Radiative atomic Rosseland mean opacity tables", ApJS 79, 507

Rogers, F. J., Iglesias, C. A. 1992b, "Rosseland mean opacities for variable compositions", ApJS 401, 361

Rogers, F. J., Nayfonov, A. 2002, "Updated and expanded OPAL equation of state tables: Implications for helioseismology", ApJ 576, 1064

Rogers, F. J., Swenson, F. J., Iglesias, C. A. 1996, "OPAL equation-of-state tables for astrophysical applications", ApJ 456, 902

Rosenthal, C., Christensen-Dalsgaard, J., Nordlund, Å., Stein, R. F., Trampedach, R. 1999, "Convective contributions to the frequencies of solar oscillations", A&A 351, 689

Saha, M. N. 1921, "On a physical theory of stellar spectra", Proc. Royal Soc. London

99(A 697), 135

Saumon, D., Chabrier, G. 1989, "A new hydrogen equation of state for low mass stars". In: G. Wegner (ed.), White Dwarfs, IAU Coll. 114, Springer Verlag, Berlin, 300

Saumon, D., Chabrier, G. 1991, "Fluid hydrogen at high density: Pressure dissociation", Phys. Rev. A. 44, 5122

Saumon, D., Chabrier, G., Horn, H. M. V. 1995, "An equation of state for low-mass stars and giant planets", ApJS 99, 713

Sauval, A. J., Tatum, J. B. 1984, "A set of partition functions and equilibrium constants for 300 diatomic molecules of astrophysical interest", ApJS 56, 193

Seaton, M. 1987, "Atomic data for opacity calculations: I. General description", J. Phys. B 20, 6363

Seaton, M. J. (ed.) 1995, The opacity project, Vol. 1. Institute of Physics Publishing

Seaton, M. J., Zeippen, C. J., Tully, J. A., Pradhan, A. K., Mendoza, C., Hibbert, A., Berrington, K. A. 1992, "The opacity project – computation of atomic data", Rev. Mex. Astron. Astrofis. 23, 19

Shibahashi, H., Noels, A., Gabriel, M. 1983, "Influence of the equations of state and of the z value on the solar five-minute oscillation", A&A 123, 283

Shibahashi, H., Noels, A., Gabriel, M. 1984, "Influence of the equations of state and of the z value on the solar oscillations", Mem. Soc. Astron. Ital. 55, 163

Skartlien, R. 2000, "A Multigroup Method for Radiation with Scattering in Three-Dimensional Hydrodynamic Simulations", ApJ536, 465

Slattery, W. L., Doolen, G. D., DeWitt, H. E., Slattery, W. L. 1982, "Equation of

state of the one-component plasma derived from precision monte carlo calculations", Phys. Rev. A 26, 2255+

Sneden, C., Johnson, H. R., Krupp, B. M. 1976, "A statistical method for treating molecular line opacities", ApJ 204, 281

Stein, R. F. 1989, "Convection and waves". In: R. J. Rutten and G. Severino (eds.), Solar and stellar granulation, Kluwer Academic Publishers, 381

Stein, R. F., Nordlund, Å. 1989, "Topology of convection beneath the solar surface", ApJ 342, L95

Stein, R. F., Nordlund, Å. 1998, "Simulations of solar granulation. I. General properties", ApJ 499, 914

Stringfellow, G. S., DeWitt, H. E., Slattery, W. L. 1990, "Equation of state of the one-component plasma derived from precision monte carlo calculations", Phys. Rev. A 41(2), 1105

Trac, H., Pen, U. 2003, "A Primer on Eulerian Computational Fluid Dynamics for Astrophysics", PASP115, 303

Trampedach, R. 1997. "Convection in stellar atmospheres", Master's thesis, Aarhus University, Århus, Denmark

Trampedach, R., Asplund, M. 2003, "Radiative Transfer with Very Few Wavelengths". In: ASP Conf. Ser. 293: 3D Stellar Evolution, 209

Trampedach, R., Asplund, M. 2004, "Opacity sampling for 3D convection simulations", A&A (in preparation)

Trampedach, R., Christensen-Dalsgaard, J., Nordlund, Å., Stein, R. F. 1997, "Near-surface constraints on the structure of stellar convection zones". In (Pijpers et al.

1997), 73

Trampedach, R., Christensen-Dalsgaard, J., Nordlund, Å., Stein, R. F. 2004a, "Improvements to stellar structure models, based on 3d convection simulations. ii. calibrating the mixing-length", A&A (in preparation)

Trampedach, R., Christensen-Dalsgaard, J., Nordlund, Å., Stein, R. F. 2004b, "Improvements to stellar structure models, based on 3d convection simulations. iii. stellar evolution with a varying mixing-length parameter", A&A (in preparation)

Trampedach, R., Däppen, W. 2004a, "MHD 2000", ApJ (in preparation)

Trampedach, R., Däppen, W. 2004b, "Pressure ionization in the MHD equation of state", ApJ (in preparation)

Trampedach, R., Däppen, W., Baturin, V. A. 2004c, "A synoptic comparison of the MHD and the OPAL equations of state", ApJ (submitted)

Trampedach, R., Stein, R. F., Christensen-Dalsgaard, J., Nordlund, Å. 1998, "Stellar evolution with a variable mixing-length parameter". In (Giménez et al. 1998), 233

Trampedach, R., Stein, R. F., Christensen-Dalsgaard, J., Nordlund, Å. 2004d, "Improvements to stellar structure models, based on 3d convection simulations. i. t-τ relations", A&A (in preparation)

Tsuji, T. 1973, "Molecular abundances in stellar atmospheres. II.", A&A 23, 411

Ulrich, R. 1982, "The influence of partial ionization and scattering states on the solar interior structure", ApJ 258, 404

Ulrich, R., Rhodes, E. 1983, "Testing solar models with global solar oscillations in the 5-minute band", ApJ 265, 551

Vardya, M. S. 1966, "Pressure dissociation and the hydrogen molecular ion",

M.N.R.A.S. 134, 183

Vernezza, J. E., Avrett, E. H., Loeser, R. 1981, "Structure of the solar chromosphere. III. Models of the EUV brightness components of the quiet sun", ApJS 45, 635

Waech, T. G., Bernstein, R. B. 1967, "Hejsa", J. Chem. Phys. 46, 4905++

Willson, R. C., Hudson, H. S. 1988, "Solar luminosity variations in solar cycle 21", Nature 332, 810